공학박사 학위논문

The development of new SnSe-based materials with ultrahigh thermoelectric figure of merit ZT

초고 열전 성능 지수 **ZT**를 가지는

새로운 틴 셀레나이드 기반 소재 개발

2020 년 8 월

서울대학교 대학원

화학생물공학부

이 용 규

The development of new SnSe-based materials with ultrahigh thermoelectric figure of merit ZT

지도교수 정 인

이 논문을 공학박사 학위논문으로 제출함

2020 년 7 월

서울대학교 대학원

화학생물공학부

이 용 규

이용규의 박사 학위논문을 인준함

2020 년 7 월

위 원 장	이 규 태	(인)
부 위 원 장	정 인	(인)
위 원	박 정 원	(인)
위 원	최 장 욱	(인)
위 원	김 명 길	(인)

Abstract

The development of new SnSe-based materials with ultrahigh thermoelectric figure of merit ZT

Yongkyu Lee

School of Chemical and Biological Engineering

The Graduate School

Seoul National University

With the rapid increase in population and the depletion of fossil fuels, the demand for new energy sources is increasing worldwide. More than 60% of the energy produced is wasted in the form of heat. Thermoelectric technology can convert thermal energy into electrical energy, and since it can use waste heat as electrical energy, it has attracted much attention as a next-generation eco-friendly energy source. For the commercialization and practical use of the technology, the most problematic at present is the low performance of the thermoelectric material. Thermoelectric materials such as bismuth telluride and lead telluride, which have

been studied the most in the past, have high thermoelectric performance through various strategies, but have limitations because they have elements such as toxic lead or very expensive tellurium. This dissertation will discuss the study of thermoelectric performance improvement of SnSe, an eco-friendly material among various thermoelectric materials.

First, PbSe and Na were introduced into polycrystalline SnSe. Through the alloying of PbSe, it was confirmed that the phase transition temperature from the crystal structure of *Pnma* to the crystal structure of *Cmcm* decreased. Also, by introducing Na, the optimum carrier concentration could be improved to a level of 10^{19}. Improved electrical conductivity and power factor were confirmed by optimized carrier concentration and lowered phase transition temperature. In addition, it was observed through aberration-corrected transmission electron microscopy that the introduction of PbSe formed nanostructures in SnSe materials, unlike the information in the existing phase diagram, which was thought to form solid solutions. Through this, it was found that the introduction of PbSe causes scattering by nanostructures, thereby lowering the thermal conductivity. The p-type SnSe-based material with a thermoelectric performance index ZT of about 1.2 was successfully developed in the composition of $Na_{0.01}(Sn_{0.95}Pb_{0.05})_{0.99}Se$ due to the improved power factor and reduced thermal conductivity.

Second, a study was conducted to improve the thermoelectric performance of SnSe by defect engineering. Sample groups were constructed by introducing vacancy and

indium into SnSe. It was confirmed that the electrical conductivity and the thermal conductivity decreased simultaneously as the vacancy content increased. However, through the introduction of indium, the electronic band structure was changed to improve the Seebeck coefficient, thereby minimizing the reduction in power factor. The thermoelectric figure of merit ZT ~2.0 was confirmed in the composition of $Na_{0.01}(Sn_{0.97}In_{0.01})_{0.99}Se$ through the lowered thermal conductivity and the improved power factor. Despite the same composition, when the annealing process was performed, the thermal conductivity was lowered. In order to investigate the cause of this, changes in the microstructure according to annealing time were observed through a Cs-corrected transmission electron microscope. It was confirmed that vacancies are distributed in clusters in a SnSe matrix that has not undergone annealing, and as the annealing progresses, vacancy clusters gather to form a heterostructure in a certain direction in SnSe matrix. Through the Cs-corrected transmission electron microscope observation and phase analysis, it was confirmed that the heterogeneous phase of In_2Se_3 was formed in the bulk SnSe, and through this, the cause of the lowered thermal conductivity was identified. In addition, the mechanism of formation of heterostructures in SnSe was suggested, and the possibility of formation of nanostructures in the SnSe bulk material through the introduction of other elements and vacancies was suggested.

Third, the purpose of this study was to find out the cause of the difference in thermoelectric performance between single crystal SnSe and polycrystalline SnSe

that have not been identified. The formation of tin oxide having a thermal conductivity of about 140 times higher than that of SnSe was confirmed in SnSe through Cs-corrected transmission electron microscopy, which is the cause of high thermal conductivity of polycrystalline SnSe. To solve this, a ball mill and a reduction process were performed. The content of oxide in the material was reduced, and at the same time, the thermal conductivity was also lower than that of a single crystal. Through this, materials with thermoelectric figure of merit ZT 2.5 were developed.

In addition, in order to more fundamentally prevent the formation of oxides, a purification and reduction process of tin used in synthesis was performed. Samples synthesized using this showed a very low oxide content, and had a lower lattice thermal conductivity than single crystal SnSe. By improving the electrical conductivity and power factor through doping of Na, the power factor was significantly improved. As a result, the cause of thermal conductivity of SnSe higher than that of single crystal was found experimentally and theoretically, and ZT 3.0 having the highest thermoelectric performance among the thermoelectric materials reported so far was developed.

In this thesis, various elements and vacancy were introduced into polycrystalline SnSe. The understanding of the material as a whole was improved by confirming the change in its thermoelectric performance and the microstructure of the material. In addition, the performance difference between single crystal and polycrystalline SnSe

was overcome through the element purification, ball mill, and reduction processes. Since this strategy can be applied to all thermoelectric materials, it can contribute to improving the performance not only of tin selenide, but also of the overall thermoelectric material field.

Keywords: Thermoelectric, Polycrystalline, SnSe, PbSe, Defect, Purification, Reduction.

Student Number: 2016-30236

Contents

List of Tables

List of Figures

Chapter 1. Introduction

1.1 Background

Humanity has found new eco-friendly energy sources to replace limited oil resources. On the other hand, more than 65 percent of the energy generated by humanity is not used in the right place and is wasted as heat energy. Thermoelectric energy conversion technology is a technology that can directly convert thermal energy such as waste heat into electrical energy, and is a technology that can satisfy both of the preceding demands[1]. It can be used semi-permanently because energy conversion occurs in the solid state, and it is an eco-friendly power generation system. In the past, conversion efficiency was low, so it was limited to special fields such as space and military applications. However, with the improvement of conversion efficiency, recently, it is possible to save energy by recovering industrial waste heat and producing electricity, and it can be produced through natural energy sources such as solar heat and geothermal heat, so it is spotlighted as the next-generation renewable energy source.

The thermoelectric effect is caused by the movement of the charge carrier due to the temperature gradient. The Seebeck effect that generates electrical potential due to temperature gradient can be used for recycling of waste heat, and the Peltier effect that generates temperature gradient through electrical energy can be used for eco-friendly cooling systems that do not use refrigerant.

$$S = \frac{\Delta V}{\Delta T}$$

$$\dot{Q} = (\Pi_A - \Pi_B)I$$

Of these components, the most important component that determines performance is the material part. Although thermoelectric materials were introduced in the 1930s and research has been continued for decades, the reason why they have only entered the commercialization stage is that materials with high thermoelectric performance have not been developed. The thermoelectric performance of a material is evaluated using a dimensionless index, ZT. In the same temperature gradient, the Seebeck coefficient and electrical conductivity for large electric potential should be high, and the lower the thermal conductivity to maintain the temperature gradient, the better the thermoelectric material. For reference, the following molecular term, which refers to the output part, is called the power factor. In addition, the thermal conductivity is expressed as the sum of the thermal conductivity by the charge carrier and the lattice thermal conductivity. Research has been in progress for decades, but the reason for the slow performance is that the factors are all interrelated, so it is difficult to increase or decrease one factor independently. Currently, the thermoelectric field is very lagging in power generation efficiency compared to other power generation fields. However, if the performance index ZT can represent 3-4 levels, it can show similar efficiency to other commercial power generation.[2]

$$ZT = \frac{S^2\sigma}{\kappa}T$$

$$\kappa = \kappa_{ele} + \kappa_{lat}$$

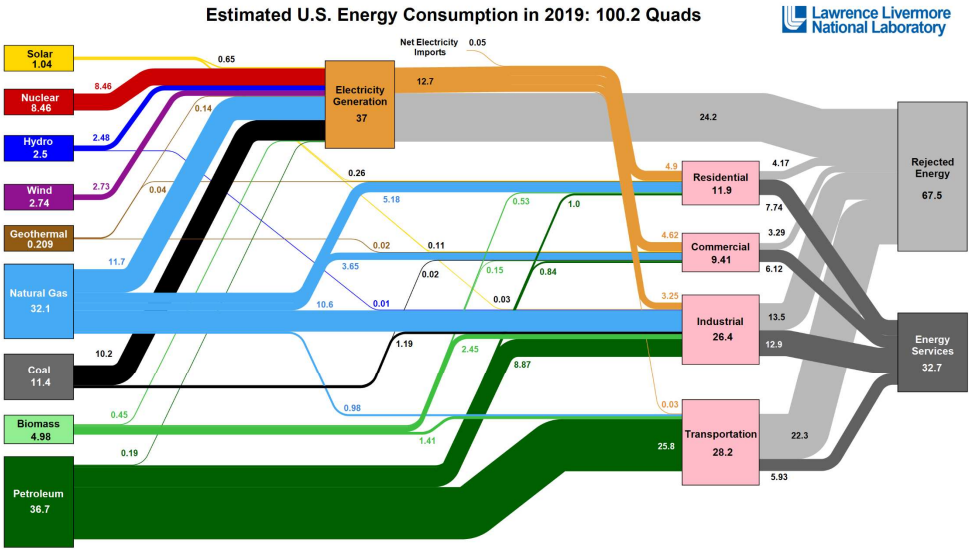

Figure 1.1. Energy flow chart of US in 2019. Data is based on department of energy in USA (DOE) and LLNL

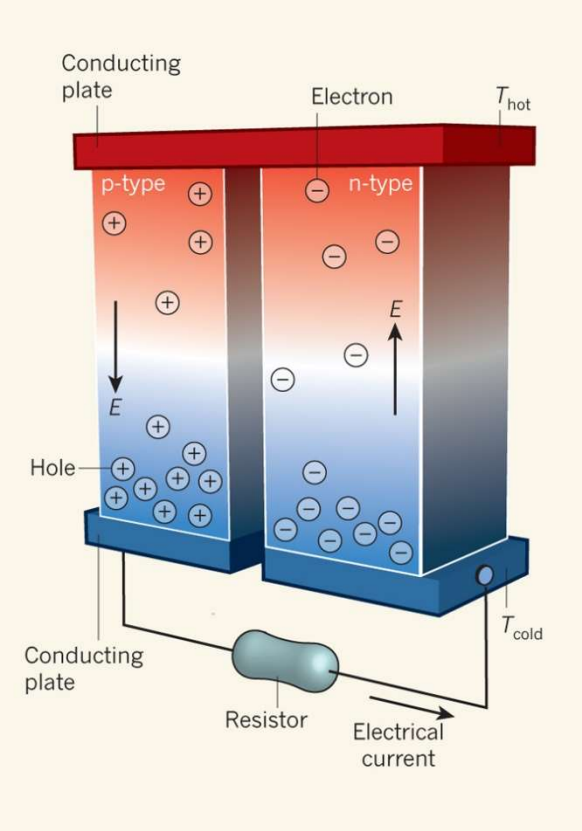

Figure 1.2. Thermoelectric generator diagram.

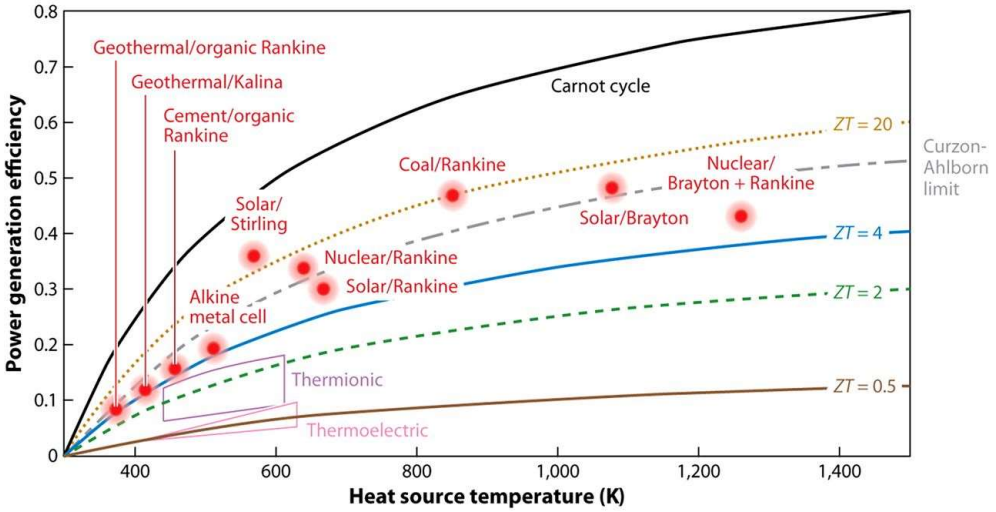

Figure 1.3 Thermoelectrics in the global landscape of energy conversion. The efficiency comparison of thermoelectrics and other energy-conversion technologies as a function of the heat-source temperature. The ZT values are assumed to be temperature independent, and the heat-sink temperature is set at room temperature.[2]

1.2 Strategy for enhancing thermoelectric performance

1.2.1. enhancing the power factor

The transport characteristics of the carrier are determined by the band structure of the material. Therefore, the power factor, which is the denominator part of the figure of merit ZT, can be improved through a strategy of changing the electronic band structure.[1] Representatively, there is a resonant level formation strategy to form a new state near the band, and a band convergence effect.

1.2.1.1. resonant level

Certain elements are introduced into the material to form a new density of state near the conduction band for the n-type and the valence band for the p-type, causing distortion in the original electronic band structure. The effective mass of the carrier is improved when the Fermi level is moved to the vicinity of the thus formed through proper doping. The effective mass can improve the Seebeck coefficient by the following equation, resulting in an improvement in the power factor.[3,4,5]

$$m^* = N_v^{2/3} m_b^*$$

where N_v is the band degeneracy, m^* is the band effective mass and m_b^* is the band effective mass of a single valley.

$$S = \frac{8\pi^2 \kappa_B^2}{3eh^2} m^* T \frac{\pi}{3n}^{2/3}$$

Figure 1.4 shows that m^* of PbTe was effectively increased due to the resonant level via Tl doping, leading to enhanced S as shown in Figure 4c. Such an effect has been found in Tl-doped PbTe, Al-doped PbSe, and some other materials, which are promising for the development of high performance TE materials.[3]

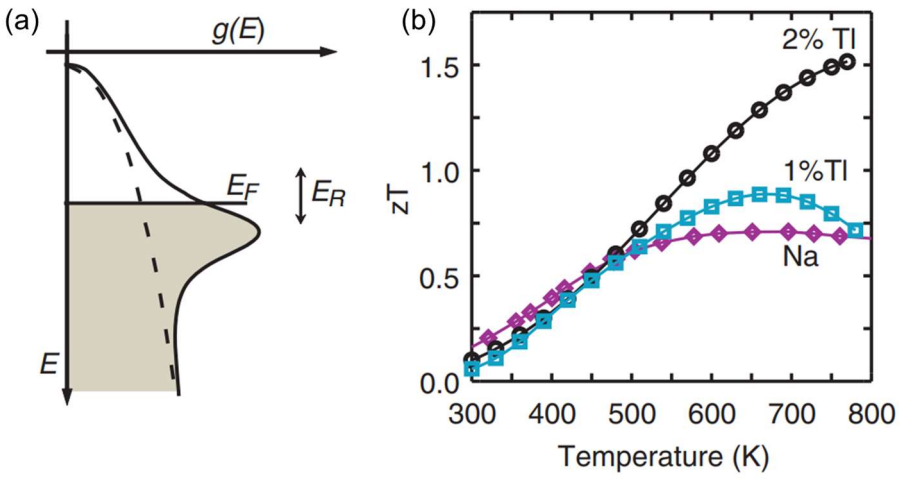

Figure 1.4. (a) Schematic representation of the density of electron states of the valence band of pure PbTe (dashed line) contrasted to that of Tl-PbTe in which a Tl-related level increases the density of states. The figure of merit ZT is optimized when the Fermi energy E_F of the holes in the band falls in the energy range E_R of the distortion. (b) The ZT values for $Tl_{0.02}Pb_{0.98}Te$ (black squares) and $Tl_{0.01}Pb_{0.99}Te$ (blue circles) compared to that of a reference sample of Na-PbTe (purple diamonds).[3]

1.2.1.2. Band convergence

As a way to improve the power factor, there is a way to improve the band degeneracy in the above equation.[6] The improvement of band degeneracy is caused by band convergence, which may be caused by doping of a specific element or an increase in temperature or a change in crystal structure. The most representative material to which the band convergence strategy is applied is PbTe, which uses the energy difference between the valence band of the L-band and the valence band of the Σ-band. When the energy gap of the two bands is reduced through factors such as doping of the element, the band degeneracy increases, and thus the carrier can have an improved effective mass. In addition, these heteroatoms are very effective strategies to improve the overall thermoelectric performance because they can act as a factor to reduce thermal conductivity at the same time.

In the sample in which Se was introduced into PbTe, a study was reported in which the energy gap of two valence bands was reduced as the temperature was increased and band degeneracy was increased. As N_v increased, effective mass increased without decreasing mobility, and as a result, ZT was greatly improved (Figure 1.5).[4]

In the case of SnTe, power factor increases when ΔE become smaller at high T – particularly ΔE = 0 eV at 900 K, $S^2\sigma$ showing the highest value. In the future, band convergence of materials with abundant constituents such as PbS, and Cu_2Cd- $SnTe_4$ should be investigated for large-scale applications.[7]

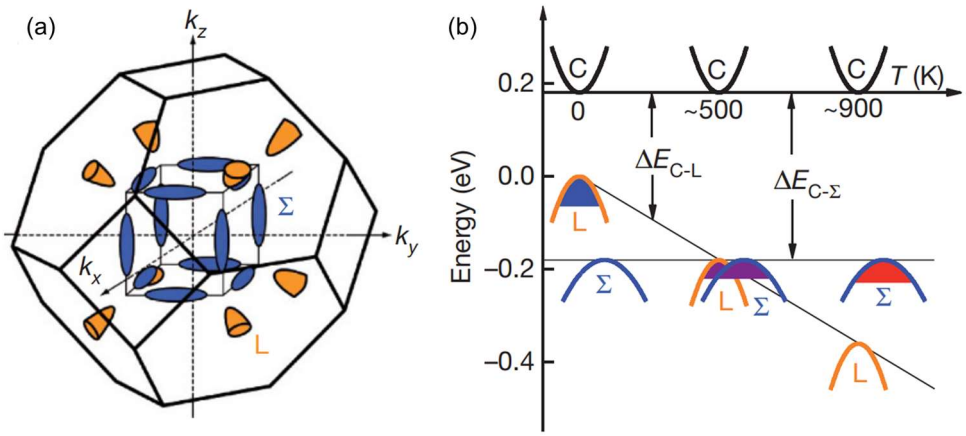

Figure 1.5. Valence band structure of $PbTe_{1-x}Se_x$. (a), Brillouin zone showing the low degeneracy hole pockets (orange) centered at the L point, and the high degeneracy hole pockets (blue) along the Σ line. The figure shows 8 half-pockets at the L point so that the full number of valleys, N_v, is 4, while the valley degeneracy of the Σ band is $N_v = 12$. (b), Relative energy of the valence bands in $PbTe_{0.85}Se_{0.15}$. At 500 K the two valence bands converge, resulting in transport contributions from both the L and Σbands. C, conduction band; L, low degeneracy hole band; Σ, high degeneracy hole band.[4]

1.2.2. Reducing the thermal conductivity

1.2.2.1 Nanostructuring

In 1993, Hicks proposed a proposal to lower the lattice thermal conductivity through a quantum confinement effect in a nanostructured material, studies on various low-dimensional materials related to this have been conducted.[8] In the low-dimensional material, the band gap of the semiconductor material may change or the characteristics of the carrier may be abnormally changed by the interface. Therefore, when the appropriate strategy is applied, the reduction of the power factor can be minimized, unlike the tendency to decrease the thermal conductivity. Self-assembled PbTe/Ag_2Te thin films[9] and PbSeTe-based superlattice have been reported.[10] In addition, a study on Bi_2Te_3 nanowires that improved ZT by dramatically lowering thermal conductivity through nanowires was also reported.[11] These studies have suggested a new possibility of improving the thermoelectric performance, which has been stagnant, but have limitations due to difficulties such as large-capacity and commercialization.

As interest in nanostructures has increased, strategies to introduce nanostructures into bulk materials have been attempted. Phonon, a medium for thermal conduction, has a short to long wavelength range. [12] An all-scale hierarchical architecturing has been reported to scatter all phonons in this wavelength range.[13] This strategy provides a material that has a complex combination of point defects for scattering

phonons with short wavelengths, grain boundaries and dislocation defects for scattering phonons in medium wavelengths, and mesoscale grains for scattering phonons in long wavelengths.[14] Through this, the lattice thermal conductivity is lowered to the amorphous limit level, and it is possible to improve the thermoelectric performance.

By providing phonon scattering of all sizes, ultra-high ZT of 2.2 to 915K was obtained due to the low κ_L of 915K in Na-doped p-type PbTe nanostructured with a endotaxially nanostructured with SrTe (Figure 1.6). [13] This strategy is effective to reduce κ_L towards the amorphous limit. In addition, the scale of these properties is still larger than the average free path of electrons, so it is important to achieve a high ZT, as the transport properties can remain almost the same. In addition, an all-scale hierarchical strategy was implemented by introducing nanostructures such as CdS, CdSe, and ZnSe into Na-doped PbSe, and at the same time, a ZT of 1.6 was achieved by minimizing carrier mobility through changes in the electronic band structure (Figure 1.7).[15]

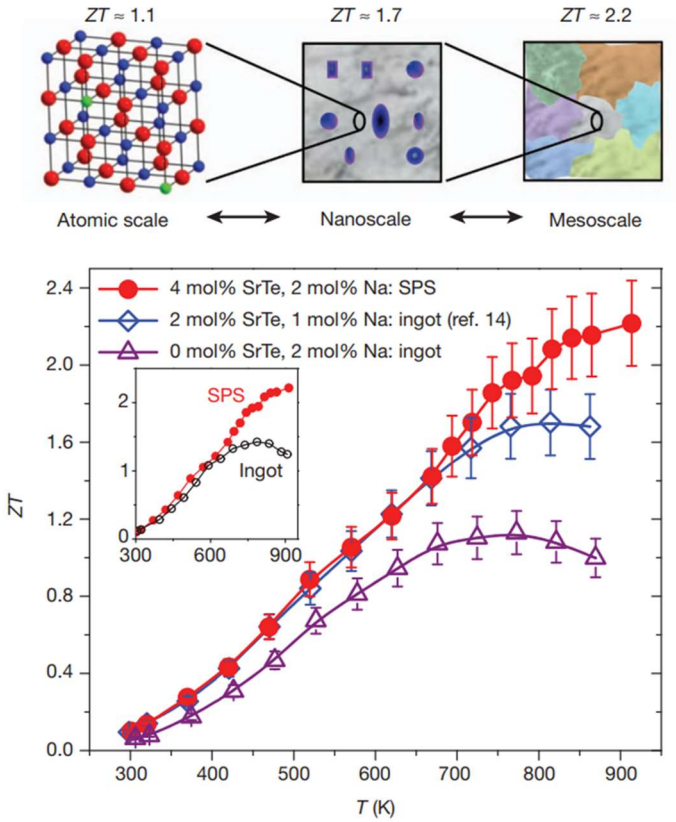

Figure 1.6. All-length-scale hierarchy in thermoelectric materials. (a) Maximum achievable ZT values for the respective length scales: the atomic scale (alloy scattering: red, Te; blue, Pb; green, dopant), the nanoscale (PbTe matrix, grey; SrTe nanocrystals, blue) to the mesoscale (grain-boundary scattering). (b) ZT as a function of temperature for an ingot of PbTe doped with 2 mol% Na (atomic scale), PbTe–SrTe(2 mol%) doped with 1 mol% Na (atomic plus nanoscale) and spark-plasma-sintered PbTe–SrTe(4 mol%) doped with 2% Na (atomic plus nano plus mesoscale).[13]

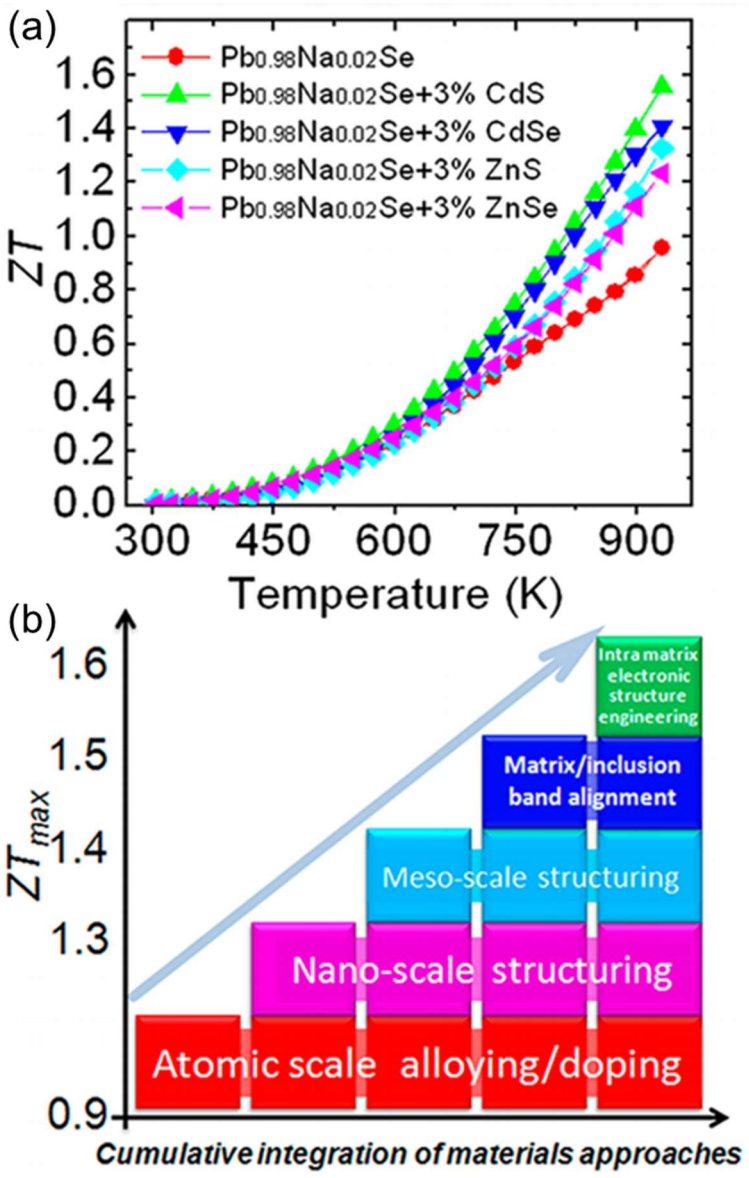

Figure 1.7. (a) Thermoelectric figure of merit ZT, as a function of temperature for $Pb_{0.98}Na_{0.02}Se$ with 3.0% second phases (CdS, CdSe, ZnS, and ZnSe). (b) Cumulative integration of material approaches as a function of ZT.[15]

1.2.2.2 Defect engineering

Defect is a factor that has many possibilities to change properties in thermoelectric materials.[16] Through the introduction of defects, the mobility of the carrier can be changed, and at the same time, it has the effect of doping. In addition, when a defect structure is generated through appropriate composition and formation conditions, the scattering of phonons can be improved.

The composition of $Pb_{1-x}Sb_{2x/3}Se$, which is composed of Sb with different oxidation numbers in PbSe and the vacancies are included. As a result of constructing such a composition, dislocations were randomly formed in the bulk material to maximize the phonon scattering.[17] The material has a thermal conductivity close to the amorphous limit, and ZT can be effectively improved. Research into forming nanostructures and dislocations in bulk materials using vacancy is currently in progress, and not only decreases thermal conductivity, but also improves thermoelectric performance with the results of changing the material's electronic band structure and carrier concentration. It is evaluated as a promising strategy for enhancing thermoelectric performances (Figure 1.8). K-doped off-stoichiometric $Bi_2Te_{3.14}$ is synthesized using a solution-based method. Instead of replacing Bi ions, K was found to exist in the interstitial and interlayer sites, pushing the Fermi level up to the conduction band as an electron donor, resulting in n-type conductivity and providing phonon scattering to enhance ZT. The other important role of lattice defects is to scatter phonons (Figure 1.9). [18]

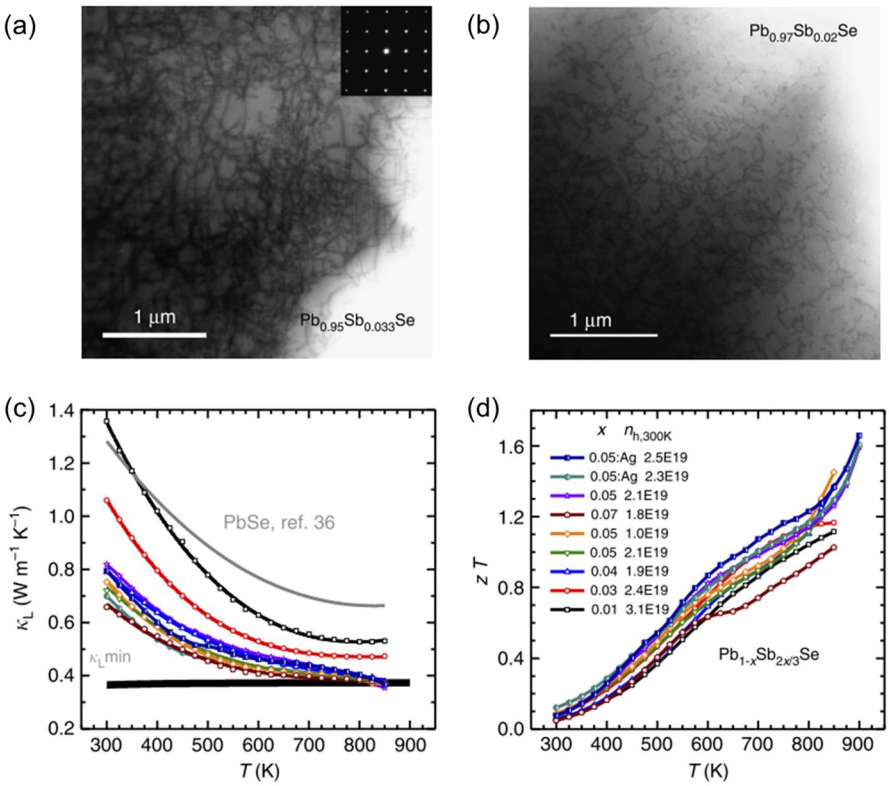

Figure 1.8. Microstructures and thermoelectric properties. Uniformly distributed dense dislocations in $Pb_{0.95}Sb_{0.033}Se$ solid solution (a) and $Pb_{0.97}Sb_{0.02}Se$ solid solution (b). The temperature-dependent lattice thermal conductivity (c) and thermoelectric figure of merit (d) for $Pb_{1-x}Sb_{2x/3}Se$ (x=0.01, 0.03, 0.04, 0.05 and 0.07) with or without Ag doping. The lattice thermal conductivity of PbSe (grey line) and estimated minimal lattice thermal conductivity (black line) are included for comparison. Dislocations due to cation vacancies lead to the lowest lattice thermal conductivity and the highest ZT in PbSe thermoelectrics.[17]

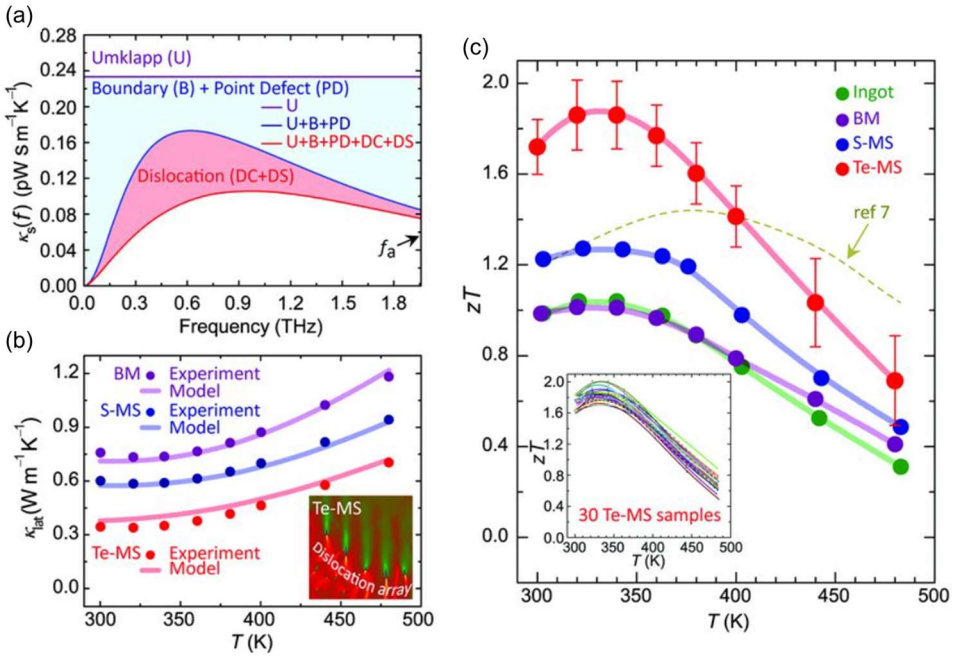

Figure 1.9. Full-spectrum phonon scattering in high-performance bulk thermoelectrics. (a) The inclusion of dislocation scattering (DC + DS) is effective across the full frequency spectrum. Boundary (B) and point defect (PD) are effective only at low and high frequencies. The acoustic mode Debye frequency is f_a.(B) Lattice thermal conductivity (κ_{lat})for $Bi_{0.5}Sb_{1.5}Te_3$ alloys produced by melt-solidification (ingot), solid-phase compaction (BM and S-MS), and liquid-phase compaction (Te-MS). The lowest κ_{lat} of Te-MS can be explained by the mid-frequency phonon scattering due to dislocation arrays embedded in grain boundaries (inset). (c) The figure of merit ZT as a function of temperature for $Bi_{0.5}Sb_{1.5}Te_3$ alloys. The data points (red) give the average of all 30 Te-MS samples (inset), which shows excellent reproducibility.[18]

1.3 SnSe

SnSe had not received attention as a thermoelectric material. In 2014, however, the thermoelectric performance of SnSe single crystal was reported by a research team at Northwestern University, making it the most popular next-generation thermoelectric material (Figure 1.10).[19] This paper measured the thermoelectric properties by growing the SnSe binary phase into a single crystal, rather than the complex composition of the basic thermoelectric material at the time, and reported the highest thermoelectric performance of 2.6 at that time. The main reason for this high performance is due to the very ultralow thermal conductivity with reasonable electrical conductivity. The two-atom-thick SnSe slabs are corrugated, creating a zig-zag accordion-like projection along the *b* axis (Figure 1.11).[20] The easy cleavage in this system is along the (100) planes. Owing to this layered, zig-zag accordion-like structure, SnSe demonstrates low anharmonicity and an intrinsically ultralow lattice thermal conductivity, making SnSe one of the world's least thermally conductive crystalline materials. Heat cannot travel well through this material because of its very "soft," accordion-like layered structure, which does not transmit vibrations well. While cooling from its high-temperature, higher symmetry phase (space group *Cmcm*, #63), SnSe undergoes a displacive (shear) phase transition at ~750–800 K, resulting in a lower symmetry *Pnma* (#62) space group (Figure 1.12). This phase transition preserves many of the advantageous transport properties of SnSe. The dynamic structural behavior of SnSe involving the reversible phase transition

helps to preserve the high power factor. The *Cmcm* phase, which is structurally related to the low temperature *Pnma* phase, exhibits a substantially reduced energy gap and enhanced carrier mobilities while maintaining the ultralow thermal conductivity thus yielding the record ZT.[21] Because of SnSe's layered structure, which does not conduct heat well, one end of the SnSe single crystal can get hot while the other remains cool. This idea can be paralleled with the idea of a posture-pedic mattress that does not transfer vibrations laterally. In the case of single crystal, it has high thermoelectric performance, but cleavage occurs very easily because the lattice has a layered structure. In addition, growing single crystals also has a very limited productivity, so there are big limitations on capacity and device size. Therefore, many studies have been conducted on polycrystalline SnSe as a substitute for this. However, polycrystalline showed relatively low electrical conductivity and high thermal conductivity, and showed very low thermoelectric performance compared to single crystal as follows.

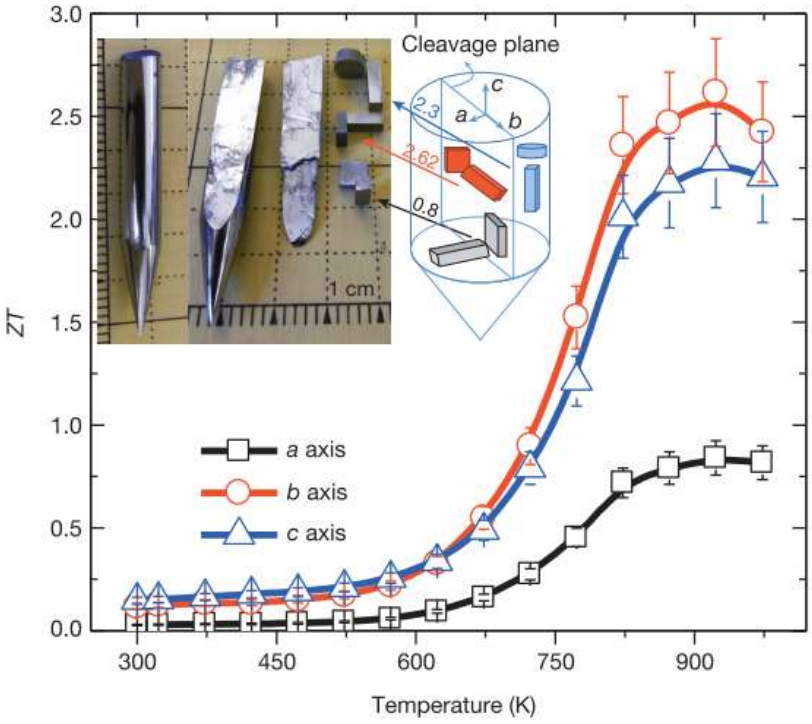

Figure 1.10. ZT values along different axial directions; the ZT measurement uncertainty is about 15% (error bars). Inset images: left, a typical crystal; right, a crystal cleaved along the (l00) plane, and specimens cut along the three axes and corresponding measurement directions. Inset diagram, how crystals were cut for directional measurements; ZT values are shown on the blue, red and grey arrows; colours represent specimens oriented in different directions.[19]

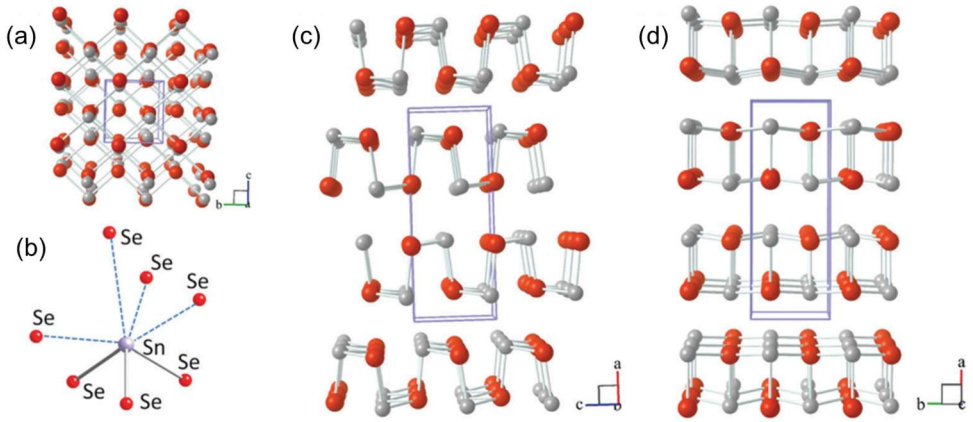

Figure 1.11. SnSe crystal structure *Pnma* at room temperature (Sn atoms are shown in gray and Se atoms in red) along the *a* axis and (b) highly distorted $SnSe_7$ coordination polyhedron with three short and four long Sn–Se bonds; (c and d) SnSe crystal structures along the *b* axis (showing the accordion like character) and *c* axis.

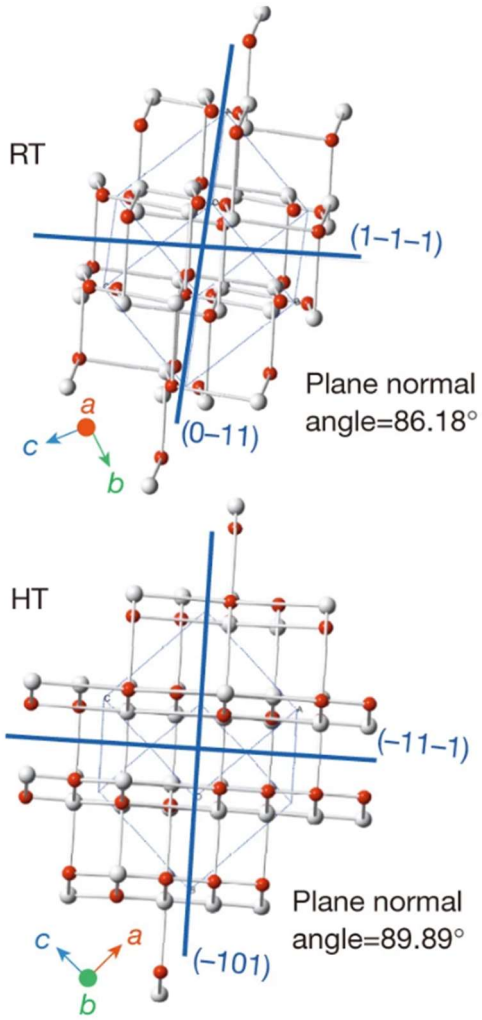

Figure 1.12. Simulated crystal structures of the phase at room temperature (RT; *Pnma*) and at high temperature (HT; *Cmcm*), viewing along the [211] and [121] directions; planes (1−1−1), (−101) and (0−11) are marked by blue lines.[19]

1.4 References

1. Zhu, T.; Liu, Y.; Fu, C.; Heremans, J. P.; Snyder, J. G.; Zhao, X., Compromise and Synergy in High-Efficiency Thermoelectric Materials. *Advanced Materials* **2017,** *29* (14), 1605884.

2. He, J.; Tritt, T. M., Advances in thermoelectric materials research: Looking back and moving forward. *Science* **2017,** *357* (6358), eaak9997.

3. Heremans, J. P.; Jovovic, V.; Toberer, E. S.; Saramat, A.; Kurosaki, K.; Charoenphakdee, A.; Yamanaka, S.; Snyder, G. J., Enhancement of Thermoelectric Efficiency in PbTe by Distortion of the Electronic Density of States. *Science* **2008,** *321* (5888), 554.

4. Pei, Y.; Shi, X.; LaLonde, A.; Wang, H.; Chen, L.; Snyder, G. J., Convergence of electronic bands for high performance bulk thermoelectrics. *Nature* **2011,** *473* (7345), 66-69.

5. Tan, G.; Shi, F.; Hao, S.; Chi, H.; Zhao, L.-D.; Uher, C.; Wolverton, C.; Dravid, V. P.; Kanatzidis, M. G., Codoping in SnTe: Enhancement of Thermoelectric Performance through Synergy of Resonance Levels and Band Convergence. *Journal of the American Chemical Society* **2015,** *137* (15), 5100-5112.

6. Gayner, C.; Kar, K. K.; Kim, W., Recent progress and futuristic development of PbSe thermoelectric materials and devices. *Materials Today Energy* **2018,** *9*, 359-376.

7. Hong, M.; Chen, Z.-G.; Pei, Y.; Yang, L.; Zou, J., Limit of ZT

enhancement in rocksalt structured chalcogenides by band convergence. *Physical Review B* **2016,** *94* (16), 161201.

8. Hicks, L. D.; Harman, T. C.; Dresselhaus, M. S., Use of quantum-well superlattices to obtain a high figure of merit from nonconventional thermoelectric materials. *Applied Physics Letters* **1993,** *63* (23), 3230-3232.

9. Ishida, A.; Yamada, T.; Tsuchiya, T.; Inoue, Y.; Takaoka, S.; Kita, T., Electrical and thermoelectrical properties of SnTe-based films and superlattices. *Applied Physics Letters* **2009,** *95* (12), 122106.

10. Rogacheva, E. I.; Nashchekina, O. N.; Meriuts, A. V.; Lyubchenko, S. G.; Dresselhaus, M. S.; Dresselhaus, G., Quantum size effects in n-PbTe⁄p-SnTe⁄n-PbTe heterostructures. *Applied Physics Letters* **2005,** *86* (6), 063103.

11. Hicks, L. D.; Dresselhaus, M. S., Effect of quantum-well structures on the thermoelectric figure of merit. *Physical Review B* **1993,** *47* (19), 12727-12731.

12. Toberer, E. S.; Zevalkink, A.; Snyder, G. J., Phonon engineering through crystal chemistry. *Journal of Materials Chemistry* **2011,** *21* (40), 15843-15852.

13. Biswas, K.; He, J.; Blum, I. D.; Wu, C.-I.; Hogan, T. P.; Seidman, D. N.; Dravid, V. P.; Kanatzidis, M. G., High-performance bulk thermoelectrics with all-scale hierarchical architectures. *Nature* **2012,** *489* (7416), 414-418.

14. Hong, M.; Chasapis, T. C.; Chen, Z.-G.; Yang, L.; Kanatzidis, M. G.; Snyder, G. J.; Zou, J., n-Type $Bi_2Te_{3-x}Se_x$ Nanoplates with Enhanced Thermoelectric Efficiency Driven by Wide-Frequency Phonon Scatterings and

Synergistic Carrier Scatterings. *ACS Nano* **2016,** *10* (4), 4719-4727.

15. Zhao, L.-D.; He, J.; Hao, S.; Wu, C.-I.; Hogan, T. P.; Wolverton, C.; Dravid, V. P.; Kanatzidis, M. G., Raising the Thermoelectric Performance of p-Type PbS with Endotaxial Nanostructuring and Valence-Band Offset Engineering Using CdS and ZnS. *Journal of the American Chemical Society* **2012,** *134* (39), 16327-16336.

16. Li, Z.; Xiao, C.; Zhu, H.; Xie, Y., Defect Chemistry for Thermoelectric Materials. *Journal of the American Chemical Society* **2016,** *138* (45), 14810-14819.

17. Chen, Z.; Ge, B.; Li, W.; Lin, S.; Shen, J.; Chang, Y.; Hanus, R.; Snyder, G. J.; Pei, Y., Vacancy-induced dislocations within grains for high-performance PbSe thermoelectrics. *Nature Communications* **2017,** *8* (1), 13828.

18. Kim, S. I.; Lee, K. H.; Mun, H. A.; Kim, H. S.; Hwang, S. W.; Roh, J. W.; Yang, D. J.; Shin, W. H.; Li, X. S.; Lee, Y. H.; Snyder, G. J.; Kim, S. W., Dense dislocation arrays embedded in grain boundaries for high-performance bulk thermoelectrics. *Science* **2015,** *348* (6230), 109-114.

19. Zhao, L.-D.; Lo, S.-H.; Zhang, Y.; Sun, H.; Tan, G.; Uher, C.; Wolverton, C.; Dravid, V. P.; Kanatzidis, M. G., Ultralow thermal conductivity and high thermoelectric figure of merit in SnSe crystals. *Nature* **2014,** *508*, 373.

20. Zhao, L.-D.; Chang, C.; Tan, G.; Kanatzidis, M. G., SnSe: a remarkable new thermoelectric material. *Energy & Environmental Science* **2016,** *9* (10), 3044-3060.

21. Chen, Z.-G.; Shi, X.; Zhao, L.-D.; Zou, J., High-performance SnSe thermoelectric materials: Progress and future challenge. *Progress in Materials Science* **2018,** *97*, 283-346.

Chapter 2 Improved thermoelectric performance of polycrystalline SnSe by controlling phase transition temperature

2.1 Introduction

Thermoelectric (TE) power generation can directly convert heat into electricity, thereby a promising renewable energy technology in automobiles and industrial power plants where the waste heat is abundant. Conversely, TE cooling can improve energy efficiency greatly in many cooling devices including fast seat cooling systems for automobiles and cooling systems for small electronic enclosures.[1-3] Unnecessariness of moving mechanical parts provides characteristic advantages of TE technology such as silent operation and consequent high reliability and mechanical stability. However, TE conversion efficiency has to be further improved yet for broader commercial markets. The efficiency of a TE material is determined by the dimensionless TE figure of merit $ZT = S^2\sigma T/\kappa$, where S is the Seebeck coefficient, σ the electrical conductivity, κ the thermal conductivity, T the absolute temperature, and $S^2\sigma$ power factor (PF). The κ of a material is the sum of contribution from lattice thermal conductivity κ_{lat} and electrical thermal conductivity κ_{elec} according to the Wiedemann-Franz law $\kappa_{elec} = L\sigma T$ where L is the Lorenz number.

Because the defining factors of *ZT* such as σ, *S*, and κ are closely correlated with each other, the improvement of *ZT* has been a difficult task. Indeed, progress in TE has been mainly propelled by introduction of new innovative strategies that contribute to achieving higher *ZT*. Artificially reducing the κ_{lat} without sacrifice in carrier mobility is the one of most successful among them and is obtained representatively by nanostructuring,[4-13] all-scale hierarchical architecturing,[14-16] and incorporating guest species in the cage-structure materials. Intrinsically low κ_{lat} is observed in specific materials that have a large molecular weight,[17] a complex crystal structure,[18] or a charge density wave distortion.[19] The *S* is enhanced by the band structure engineering,[20-23] valence band convergence,[24] quantum confinement effects,[25] and carrier filtering effect.[26] Multiples of those strategies can jointly contribute to enhance ZT as exemplified by PbTe system. For example, PbTe-8% SrTe exhibits remarkably high *ZT* of 2.5 at 923 K, which results synergistically from the boosted *S* by valence band convergence and extremely low κ_{lat} by nanostructuring.

In contrast to PbTe- and Bi_2Te_3-based materials that have been extensively studied for the last six decades, SnSe has been ignored for TE applications mainly because of seemingly high electrical resistivity. In 2014, Kanatzidis group revealed that SnSe shows a record high *ZT* of 2.6 at 923 K along the crystallographic *b*-axis when it is grown as a single crystal form. The surprisingly high *ZT* originates from unique crystal chemistry of SnSe.[27] First, the corrugated layered structure coupled

with highly distorted [$SnSe_7$] polyhedra provides anisotropic and anharmonic bonding characteristic, consequently giving rise to one of the lowest κ_{lat} values known for crystalline materials (< 0.4 W m^{-1} K^{-1} at 923K) by phonon scattering. Second, SnSe undergoes a displacive phase transition from the *Pnma* to *Cmcm* space group at 750-800 K.[28-30] The structural change causes significantly reduced band gap accompanied by increased carrier mobility while retaining ultralow κ_{lat}, thereby resulting in the abrupt rise of *ZT* near the temperature of phase transition (T_c).

It should be noted that close correlation of the crystal chemistry with the variation of ZT value of SnSe prompts to address two important issues for TE applications of SnSe.

Firstly, developing how to control the T_c is of paramount importance because only high temperature phase adopting the *Cmcm* space group exhibits high TE performance. Secondly, the structural advantages resulting in high ZT of single crystal SnSe may not be fully beneficial to its polycrystalline form that consists of randomly packed micro-crystallites. Indeed, the single crystal exhibits significant deviation in the ZT value along the crystallographic direction, for example, 2.6 and 0.8 at 923 K along the *b*- and the *a*-axis, respectively. In addition, bulk polycrystalline materials exhibit lower *PF* and higher κ_{lat} than single crystals,[27, 31] thereby much lower *ZT* than the latter.[32-37] For example, a maximum *ZT* of p-type Na- or K-doped SnSe[33] is 0.8 at 800 K and that of n-type 3% I- and 10% S-doped SnSe is 1.0 at 773 K.[34] In comparison, Na-doped single crystal shows a record high

device *ZT* of ~1.34 from 300 to 773 K.[31] Nonetheless, *ZT* of polycrystalline SnSe corresponding to or even higher ZT than that of the single crystal has to be pursued for practical applications because of its facile processability, low cost, and mechanical robustness. This should be a viable goal in that polycrystalline PbTe- and Bi_2Te_3-based TE materials outperform the corresponding single crystals.

Here we report a new strategy to improve TE properties of bulk polycrystalline SnSe, namely, controlling the temperature of phase transition (T_c) coupled with optimizing carrier concentration. We, for the first time, demonstrate that Pb alloying to form $Sn_{1-x}Pb_xSe$ solid solution facilitates the phase transition and reduces T_c at a rate of ~-3.2 K per mol% of Pb up to $x \sim 0.2$. For example, the T_c of SnSe at 795 K significantly drops to 730 K of $Sn_{0.8}Pb_{0.2}Se$. We also reveal that the decreased T_c downshifts the activating temperature of bipolar conduction that determines upturn temperature of σ and κ_{elec} and temperature of S_{max}. Consequently, the T_c directly affects transport properties of SnSe at its TE operating temperature and finally the value of *ZT*.

It should be noted that optimization of carrier concentration is essential to employ this strategy. Because Pb almost exclusively adopt +2 formal charge in contrast to Sn involving unavoidable evolution of Sn^{4+} impurity, incorporation of Pb inevitably reduce hole carrier concentration to give poor *S* value. To address this, we developed $Na_{0.01}(Sn_{1-x}Pb_x)_{0.99}Se$ ($x \leq 0.2$) system with Na hole doping to optimize the carrier concentration. Consequently, $Na_{0.01}(Sn_{0.96}Pb_{0.04})_{0.99}Se$ exhibits a high *ZT*

of 1.2 at 773 K, which is ~70% improved from undoped polycrystalline SnSe (ZT = ~0.7 at 823 K). The enhancement of ZT is attributed to the synergistic effect of an enhanced PF by reduced T_c and a decreased κ_{lat} by phonon scattering due to the formation of solid solution $Sn_{1-x}Pb_xSe$. Importantly, we use spherical aberration corrected scanning transmission electron microscopy (Cs-corrected STEM) to better understand the TE properties of $Na_{0.01}(Sn_{1-x}Pb_x)_{0.99}Se$ system and investigate effects of solid solution at the atomic level.

2.2 Experimental section

2.2.1 Synthesis. Polycrystalline SnSe-based materials were synthesized by a conventional high-temperature solid state reaction. Stoichiometric amounts of Sn chunk (99.999% American Elements, US), Se shot (99.999% 5N Plus, Canada), Na pieces (99.9%, Sigma-Aldrich, US), and Pb wire (99.99%, 5N Plus, Canada) were weighed and loaded into a 11 mm quartz tube. For Na-doped materials, the inner wall of the quartz tube was coated with carbon to prevent possible reaction between Na and the tube wall. The tube was evacuated to 10^{-4} Torr, flame sealed and then put into a 16 mm fused silica tube that was again evacuated and sealed. The larger quartz tube was used to protect the material from oxidation because the inner tube can be broken when cooling down due to the phase-transition. The double-sealed tube was placed in a furnace, heated to 1223 K in 12 h, held for 12h followed by a furnace cooling to room temperature. The obtained ingots were ground to a powder using a

mechanical grinder to reduce the particle sizes to < 45 μm in an Ar-filled glove box. The powders were loaded into a graphite die in an Ar-filled glove box and were densified at ~783 K for 5 min under an axial pressure of 50 MPa in a vacuum of ~1.4 × 10^{-2} Torr by a spark plasma sintering system (SPS-211Lx, Fuji Electronic Industrial Co., Japan). The chemical composition of the samples analyzed by EPMA and ICP-AES is close to the nominal one (Table 2.1).

2.2.2 Characterization. Powder X-ray diffraction (PXRD) analysis was performed using Cu Kα radiation on a diffractometer operating at 40 kV and 30 mA at room temperature (SmartLab Rigaku powder X-ray diffractometer, Japan). Temperature-dependent PXRD were performed on a diffractometer operating 45 kV 200 mA (SmartLab Rigaku powder X-ray diffractometer with high temperature accessory, PTC-evo, Japan). The T_c was measured on a differential scanning calorimeter (DSC 214 Polyma, Netzsch, Germany). The chemical composition was analyzed on a field emission electron probe microanalyzer (EPMA, JXA-8530F, JEOL, US) and an inductively coupled plasma atomic emission spectrometer (ICP-AES, Optima 8300, PerkinElmer, US).

2.2.3 Transport property measurements. The samples after SPS were cut for electrical and thermal property measurement using a diamond saw and polished with ethanol using a polishing machine (Model 650, South Bay Technology, US) under N_2 atmosphere. Electrical conductivity and Seebeck coefficient of disk-shaped samples were measured simultaneously under a helium atmosphere from room

temperature to 823 K using Netzsch SBA 458 instrument. Temperature-dependent Hall coefficient R_H of the samples was measured by a Hall effect measurement system (HMS8407, LakeShore, US) in magnetic fields of 1.5 T. The hole carrier concentration (n_H) and hole mobility (μ_H) were calculated by $n_H = 1/(e \cdot R_H)$ and $\mu_H = R_H \cdot \sigma$, respectively. A Netzsch LFA 457 MicroFlash instrument was used to measure the thermal diffusivity of samples coated with graphite. The thermal conductivity was calculated by $\kappa = D \cdot C_p \cdot \rho$, where D is thermal diffusivity, C_p is the heat capacity, and ρ is the density. The temperature-dependent C_p values were indirectly derived using a standard sample (Pyroceram). The density values were obtained using sample dimensions and weight. In this work, the electrical thermal conductivity (κ_{elec}) value was estimated from $\kappa_{elec} = L\sigma T$, where L is the Lorenz number. The L values as a function of temperature were obtained from previous studies.[27, 31] The κ_{lat} value was estimated by subtracting the κ_{elec} value from the κ_{tot} value: $\kappa_{lat} = \kappa_{tot} - \kappa_{elec}$.

2.2.4 Transmission electron microscopy. Cross-sectional samples for scanning TEM (STEM) were prepared by focused ion beams (FIB, Helios 650, FEG, FEI) with a dual beam microscope using gallium ion milling. Before the ion milling process, carbon was sputtered to preserve the sample by surface coating. The samples were further polished with a low-voltage and low-angle argon ion beam milling apparatus (NANO MILL, Model 1040, FISCHIONE). The atomic structures and chemical composition were examined using a spherical aberration-corrected JEM

ARM-200F microscope (Cold FEG Type, JEOL) equipped with a SDD type energy dispersive X-ray spectroscopy (EDS) detector (Solid Angle 0.9-sr, X-MaxN 100TLE, OXFORD) and electron energy loss spectroscopy (EELS) detector (965 GIF Quantum ER, GATAN) at 200 kV. In the high-angle annular dark-field (HAADF) STEM images, the point-to-point resolution was about 80 pm after the Cs-correction, and the angular range of the annular detector used was 68 mrad to 280 mrad. All images were acquired by a high-resolution CCD detector using a 2k × 2k pixel device (UltraScan 1000, GATAN). For STEM-EDS analyses, chemical maps were acquired with a probe size of 0.13 nm and a probe current of 40 pA. For STEM-EELS measurements, the energy dispersion was set at 0.1 eV ch^{-1}. The full-width at half-maximum of the zero-loss peak in vacuum was 0.8 eV. The convergence and collection semiangles were 19 and 19.8 mrad, respectively.

2.3 Results and discussion

2.3.1 Powder X-ray Diffraction and Phase-Transition Temperatures

Pb atoms form cubic rock-salt structure with chalcogene atoms (S, Se, Te). In contrast, Sn, its smaller congener in Group 14, shows different crystal chemistry. SnSe and SnS crystallizes in the orthorhombic GeS-type structure made of corrugated two-atom-thick [GeS] layers (Figure 1), whereas SnTe adopts the same cubic rock-salt structure as the Pb salts.

As a result, their alloys of $Sn_{1-x}Pb_xSe$ and Na-doped phases of $Na_{0.01}(Sn_{1-x}Pb_x)_{0.99}Se$ form GeS-type structure only up to $x \sim 0.2$ according to powder X-ray diffraction (PXRD) patterns (Figures 2.2a and 2.2b), in contrary to solid solutions of $Sn_{1-x}Pb_xTe$ ($0 \leq x \leq 1$) by isostructural SnTe and PbTe. Accordingly, alloying with larger mole% of Pb results in precipitation of PbSe as observed in $Sn_{0.7}Pb_{0.3}Se$. The refinement of XRD patterns reveals that the unit cell of the solid solutions expands along the *a*- and *b*- axes and contracts along the *c*-direction upon incorporation of larger Pb and Na atoms than Sn atom, indicating anisotropic expansion. Note that the effective ionic radii of Pb^{2+}, Na^{+}, and Sn^{2+} in octahedral geometry is 1.19, 1.02, and 0.87 Å, respectively.[39] For example, the lattice dimension of $Sn_{0.8}Pb_{0.2}Se$ is a = 11.601(6) Å, b = 4.197(1) Å, c = 4.424(1) Å, and V = 215.402 (9) $Å^3$ and that of SnSe is a =11.500(2) Å, b =4.158(2) Å, c =4.447(1) Å, V = 212.642 (8) $Å^3$ (Figure 2.3). Because a key element of exceptional thermoelectric properties of SnSe is the temperature-driven phase-change from the lower symmetry of *Pnma* space group to the higher *Cmcm*, we performed high-temperature PXRD studies for pristine SnSe, $Sn_{0.95}Pb_{0.05}Se$ and $Sn_{0.9}Pb_{0.1}Se$ (Figures 2.2c and 2.2d) on heating from 740 K to 830 K. The (011) reflection peak at $2\theta = 30.1^\circ$ corresponding to the *Pnma* space group gradually disappears in $Sn_{0.9}Pb_{0.1}Se$ from 700 to 830 K while it still keeps intensity for pristine SnSe. This observation demonstrates that Pb alloying decreases T_c of SnSe effectively, which is confirmed by DSC studies (Figure 2.4).

DSC data of $Sn_{1-x}Pb_xSe$ (x = 0, 0.05, 0.1, 0.15, 0.2) show the nearly linear decrease in T_c with increasing amount of Pb at a rate of ~-3.2 K per %Pb until the x value reaches to the solubility limit of ~0.2. For example, $Sn_{0.8}Pb_{0.2}Se$ undergoes phase transition at 730 K, which is 65 K lower than that of the pristine SnSe at 795K. This behavior can be understood in light of relationship between the defect formation and the Gibbs free energy ($G = H - TS$) that determines phase transition. Incorporating Pb in SnSe can be regarded as the defect formation in structure and would be endothermic because the resulting lattice disruption induces increase in enthalpy (H) of $Sn_{1-x}Pb_xSe$. At the same time, induced disorder also contributes to increase in its entropy (S). The $-TS$ term becomes more negative as the Pb content increases or the temperature increases. Accordingly, the minimum in Gibbs energy shifts to lower temperature at higher Pb content on heating. Then, the solid solution with more Pb could undergo phase transition at lower temperature. This finding is substantially important for SnSe-based thermoelectrics because the phase transition induces considerable reduction in band gap, followed by a bipolar conduction with rising temperature, ultimately contributing high ZT.[26]

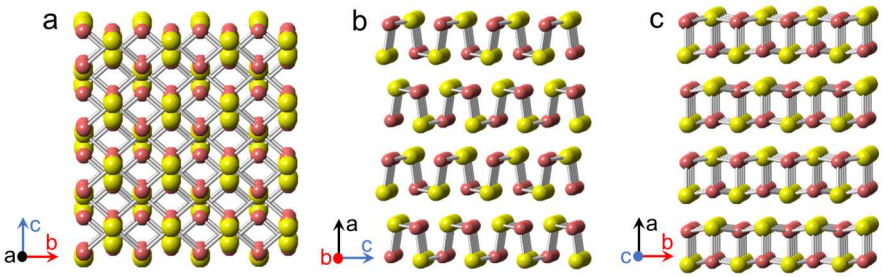

Figure 2.1. Crystal structure of a) along the *a* axis, b) along the *b* axis, and c) along the *c* axis for SnSe: Sn (yellow) and Se (red) atoms.

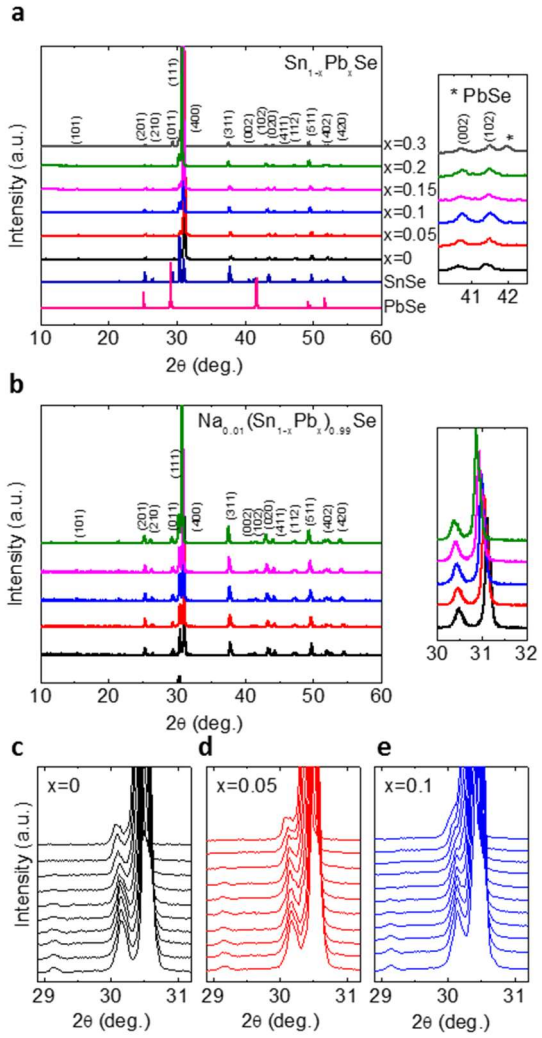

Figure 2.2 Powder X-ray diffraction (PXRD) patterns of (a) $Sn_{1-x}Pb_xSe$ (x = 0, 0.1, 0.2, 0.3) and (b) $Na_{0.01}(Sn_{1-x}Pb_x)_{0.99}Se$ (x = 0, 0.05, 0.1, 0.15, 0.2) and the peaks of PbSe phase are marked by asterisk, and temperature-dependent PXRD patterns of (c) SnSe, (d) $Sn_{0.95}Pb_{0.05}Se$, and (e) $Sn_{0.9}Pb_{0.1}Se$.

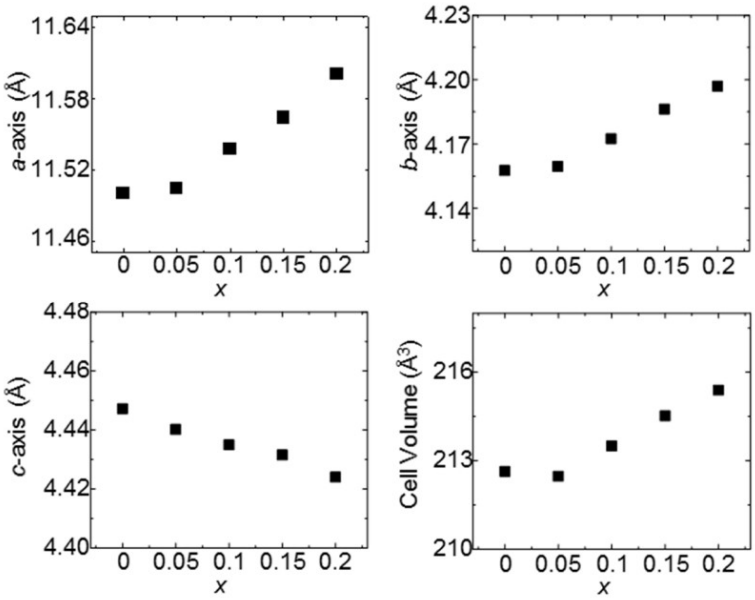

Figure 2.3. Lattice parameters and cell volume as a function of x for (a) $Sn_{1-x}Pb_xSe$ (x = 0, 0.05, 0.1, 0.15, 0.2)

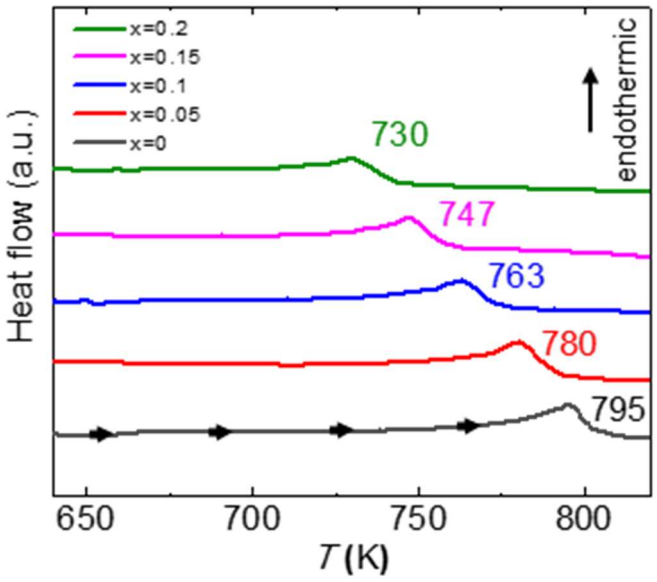

Figure 2.4. Differential scanning calorimetry analysis of $Sn_{1-x}Pb_xSe$ (x = 0, 0.05, 0.1, 0.15, 0.2) at a rate of 10 K min^{-1} on heating.

2.3.2 Thermoelectric Properties of $Sn_{1-x}Pb_xSe$

We investigated transport properties of $Sn_{1-x}Pb_xSe$ system to understand the correlation between T_c and TE performance. In this work, the TE transport properties including σ, *S*, and κ were measured perpendicular to the pressing direction of spark plasma sintering (SPS), unless noted otherwise. The temperature-dependent electrical conductivity (σ(*T*)) of SnSe keeps nearly a constant value up to ~535 K and abruptly increases with temperature (Figure 2.5a). Such a rapid upturn above ~525 K mainly results from the thermal excitation of minority carriers that are strongly related with the phase-transition.[26, 41] The σ(*T*) of $Sn_{1-x}Pb_xSe$ (x = 0, 0.05, 0.1, 0.15, 0.2) show the same trend as that of SnSe. The more Pb is alloyed, the lower σ is observed, especially at high temperature. For instance, the σ value for x = 0, 0.05, 0.1, 0.15, and 0.2 samples at 823 K is ~60, ~50, ~38, ~34, and ~28 S cm^{-1}, respectively. The reduced σ value upon Pb incorporation should result from the decrease in hole mobility (μ_H) and hole concentration (n_H), as confirmed by Hall effect measurement at 300 K (Figures 2.6a and 2.6b) The n_H value of x = 0, 0.05, 0.1, 0.15, and 0.2 samples at 300 K is ~2.52×10^{17}, ~2.89×10^{17}, ~2.42×10^{17}, ~7.41×10^{16}, and ~6.11×10^{16} cm^{-3}, respectively (Figure 2.6a). The n_H values of $Sn_{1-x}Pb_xSe$ remain nearly same for $x \leq 0.1$ and decrease afterwards as the Pb content reaches up to x = 0.2 probably because the Pb substitution more than 10% suppresses the generation of intrinsic Sn vacancies. The μ_H value at 300 K declines from ~46 cm^2 V^{-1} s^{-1} for x = 0 to ~11 cm^2 V^{-1} s^{-1} for x = 0.2 because of enhanced alloy scattering

with increasing Pb contents (Figure 2.6b).

The temperature-dependent Seebeck coefficient ($S(T)$) of $Sn_{1-x}Pb_xSe$ exhibits a dip at ~525 K followed by rapid decrease above ~575 K (Figure 2.5b). Such a dip is also found in polycrystalline SnSe reported by other research groups but is not observed in alkali metal-doped polycrystalline SnSe and undoped single crystalline SnSe. The rapid downturn of the $S(T)$ is consistent with the abrupt upturn of the $\sigma(T)$, plausibly due to a bipolar conduction. The maximum S values range between 510 and 550 μV K^{-1}, which is similar to that of undoped SnSe single crystal.[26] The power factors (PF, σS^2) of $Sn_{1-x}Pb_xSe$ (x = 0, 0.05, 0.1, 0.15, 0.2) remain almost constant up to ~525 K and suddenly increase afterwards (Figure 2.5c). The maximum PFs of ~5.6, ~5.0, ~4.3, ~3.9, and ~3.3 μW cm^{-1} K^{-2} are achieved at ~823 K for x = 0, 0.05, 0.1, 0.15, and 0.2, respectively. The temperature-dependent total thermal conductivity $\kappa_{tot}(T)$ of pristine SnSe decreases with rising temperature until 773 K and subsequently increases at higher temperatures because of bipolar conduction caused by the phase-transition (Figure 2.5d). The variation in $\kappa_{tot}(T)$ is nearly similar for all samples. However, the upturn temperature in $\kappa_{tot}(T)$ is lower with higher Pb mol%. The upturn temperature for x = 0.05, 0.1, 0.15, and 0.2 sample is ~723, ~623, ~573, and ~523 K, respectively. This is strongly related with the reduced T_c by the incorporation of Pb as confirmed by temperature-dependent PXRD and DSC data. Figure 4e shows that $\kappa_{tot}(T)$ is dominated by phonon contribution for all samples. The κ_{lat} values of $Sn_{1-x}Pb_xSe$ slowly decrease with temperature, for

example, $\kappa_{lat} \sim T^{-0.6}$ for $Sn_{0.95}Pb_{0.05}Se$ while that of SnSe follows a T^{-1} dependence, indicative of Umklapp process dominated phonon transport (Figure 2.5e). The deviation from T^{-1} dependence for $Sn_{1-x}Pb_xSe$ should be attributed to the reduction in T_c and/or optical phonon contribution.[42] Indeed, stabilization of $Sn_{1-x}Pb_xSe$ solid solution is effective for the reduction in κ_{lat} because of point defect scattering with thermal phonons. Nonetheless, because the bipolar conduction for $Sn_{1-x}Pb_xSe$ begins at lower temperature than pristine SnSe and wins over the effect of point defect scattering caused by Pb, the high temperature κ_{tot} values are larger than that of pristine SnSe. A maximum TE figure of merit ZT for x = 0.05, 0.1, 0.15, and 0.2 at 823 K is ~0.62, ~0.52, ~0.52, and ~0.44, respectively, which is lower than ~0.68 for pristine SnSe (Figure 2.5f). Because Pb almost exclusively adopts Pb^{2+} formal charge in contrast to Sn readily stabilizing Sn^{2+}/Sn^{4+}, incorporation of Pb into SnSe results in very low hole density of ~10^{17} cm^{-3}. Accordingly, Pb alloying alone could not enhance ZT despite the positive effect of downshifting T_c. Consequently, boosting hole concentration of $Sn_{1-x}Pb_xSe$ up to the order of ~10^{19} cm^{-3} is necessary to benefit the effect of tuning T_c.

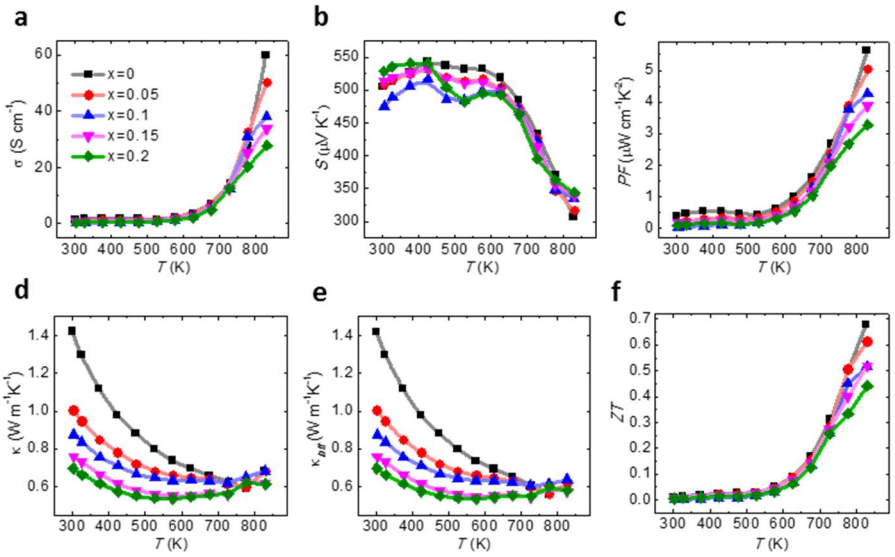

Figure 2.5. Temperature dependence of (a) electrical conductivity σ, (b) Seebeck coefficient *S*, (c) power factor *PF* (= σS^2), (d) total thermal conductivity κ_{tot}, (e) lattice thermal conductivity κ_{lat}, and (f) the TE figure of merit *ZT* of $Sn_{1-x}Pb_xSe$ (x = 0, 0.05, 0.1, 0.15, 0.2).

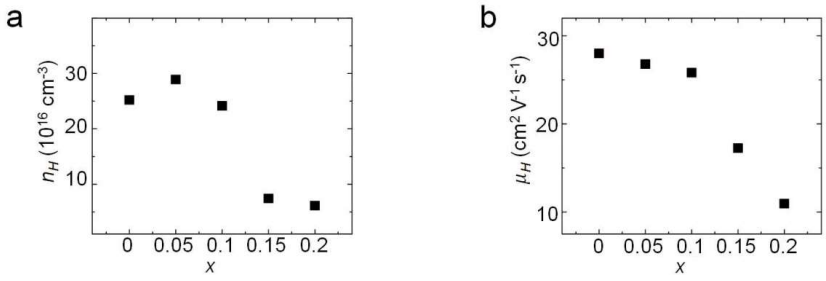

Figure 2.6. (a) Hall carrier concentration and (b) mobility at room temperature as a function of x for $Sn_{1-x}Pb_xSe$ (x = 0, 0.05, 0.1, 0.15, 0.2).

2.3.3 Thermoelectric Properties of $Na_{0.01}(Sn_{1-x}Pb_x)_{0.99}Se$ (x = 0, 0.05, 0.1, 0.15, 0.2)

To address poor hole density (n_H) of $Sn_{1-x}Pb_xSe$ system, we introduced sodium metal as a hole-dopant. 1% Na doping to $Sn_{1-x}Pb_xSe$ system effectively increases the n_H value at room temperature nearly two orders of magnitude larger than SnSe and $Sn_{1-x}Pb_xSe$: the n_H value for x = 0, 0.05, 0.1, 0.15, and 0.2 is ~4.81×10^{19}, ~4.31×10^{19}, ~4.11×10^{19}, ~3.26×10^{19}, and ~2.85×10^{19} cm^{-3}, respectively, in comparison with 2.52×10^{17} cm^{-3} of SnSe (Figure 2.7a). The n_H value of $Na_{0.01}(Sn_{1-x}Pb_x)_{0.99}Se$ decreases as x is raised from 0.1 to 0.2 probably due to the suppression of intrinsic Sn vacancies, which is consistent with the case of $Sn_{1-x}Pb_xSe$. However, the μ_H values at 300 K is significantly lower at ~6 $cm^2 V^{-1} s^{-1}$ for x = 0 and ~2 $cm^2 V^{-1} s^{-1}$ for x = 0.15 than ~46 $cm^2 V^{-1} s^{-1}$ of undoped SnSe. This implies that the substantial enhancement in the μ_H is necessary for heavily-doped SnSe-based polycrystalline materials for further enhancement of TE performance (Figure 2.7b).

The increased n_H value considerably improves the σ value, for example, ~59 S cm^{-1} of $Na_{0.01}Sn_{0.95}Pb_{0.05}Se$ in comparison with ~0.8 S cm^{-1} of $Sn_{0.95}Pb_{0.05}Se$ and ~1.6 S cm^{-1} of polycrystalline SnSe at 300 K (Figure 2.8a). For all samples, the σ value increases with temperature from 300 to ~373 K, and subsequently decreases with temperature until ~673 K, and finally increases quickly afterwards due to the bipolar conduction. This trend is different from monotonous metallic conduction behavior of single crystalline Na-doped SnSe from 300 to 773 K.[30] It should be noted

that the reduction in T_c by the incorporation of Pb downshifts the temperature of bipolar conduction and the consequent upturn temperature. As a result, high σ value at high temperature is recovered quickly, favorably contributing to high PF and ZT above 700 K. For example, the rapid upturn temperature of the σ value for x = 0.05, 0.1, 0.15, and 0.2 is ~673, ~623, ~623, and ~573 K, respectively.

The S value of $Na_{0.01}(Sn_xPb_{1-x}Se)$ increases with temperature up to 600-673 K and then decreases with further rising temperature (Figure 2.8b), showing similar trend to $Na_{0.01}Sn_{0.99}Se$ single crystal.[30] The room temperature S value of x = 0, 0.05, 0.1, 0.15, and 0.2 is ~141, ~140, ~154, ~139, and ~150 μV K^{-1}, respectively. The respective maximum S value (S_{max}) is ~325, ~378, ~331, ~320, and ~292 μV K^{-1} at 673, 673, 673, 623, and 623 K, respectively. Importantly, the temperature of the S_{max} is also strongly related with bipolar conduction as the upturn temperature of the σ. Accordingly, the reduced T_c by Pb incorporation lowers the temperature of the S_{max}. The maximum PFs for x = 0, 0.05, 0.1, 0.15, and 0.2 samples is ~5.2, ~6.3, ~4.6, ~4.2, and ~4.3 μW cm^{-1} K^{-2} 773 K, respectively (Figure 2.8c). A remarkable enhancement in PF value by ~20% for $Na_{0.01}(Sn_{0.99}Pb_{0.05})_{0.99}Se$ are achieved mainly due to the gain in σ value compared to $Na_{0.01}Sn_{0.99}Se$.

According to a previous study,[30] the κ_{tot} values of hole-doped SnSe single crystals of $Na_{0.01}Sn_{0.99}Se$ are higher than that of undoped SnSe because of the contribution from enhanced hole carriers. In contrast, the hole-doped polycrystalline SnSe shows nearly the same κ_{tot} value at 300 K as that of undoped SnSe. The

incorporation of Pb also influences on thermal transport properties significantly. The reduction in T_c by Pb alloying decreases the upturn temperature of the $\kappa_{tot}(T)$ (Figure 2.8d), for example, ~773, ~773, ~723, ~673, and ~673 K for x = 0, 0.05, 0.1, 0.15, and 0.2 samples, respectively. The high temperature κ_{tot} value of Pb alloyed SnSe is higher than that of pristine SnSe. For instance, the κ_{tot} value at 773 K for $Na_{0.01}(Sn_{0.08}Pb_{0.02})_{0.99}Se$ and $Na_{0.01}Sn_{0.99}Se$ is ~0.57 and ~0.44 W m^{-1} K^{-1}, respectively. This indicates that the higher Pb content gives rise to the larger κ_{tot} value at high temperature because a bipolar conduction becomes dominant at a relatively lower temperature with a higher Pb content. Accordingly, the delicate control of Pb alloying is important to achieve positive effect both on electrical and thermal transport properties. The variation of κ_{lat} (T) of $Na_{0.01}Sn_{0.99}Se$, $Na_{0.01}(Sn_{0.95}Pb_{0.05})_{0.99}Se$, and $Na_{0.01}(Sn_{0.9}Pb_{0.1})_{0.99}Se$ shows $T^{-1.2}$, $T^{-1.1}$, and $T^{-0.7}$ dependence (Figure 2.8e), respectively, revealing that the Umklapp phonon scattering is dominant for Na-doped materials with Pb substitution (x < 0.1). The sample of x = 0.05 exhibits the highest ZT of ~1.16 at ~773 K among all samples, which is attributed from remarkably improved PF of ~6.3 μW cm^{-1} K^{-2} and lower κ_{lat} of ~0.31 W m^{-1} K^{-1} at ~773 K compared to pristine SnSe. The corresponding ZT value of x = 0, 0.1, 0.15, and 0.2 samples is ~0.76, ~0.61, ~0.57, and ~0.45, respectively (Figure 2.8f).

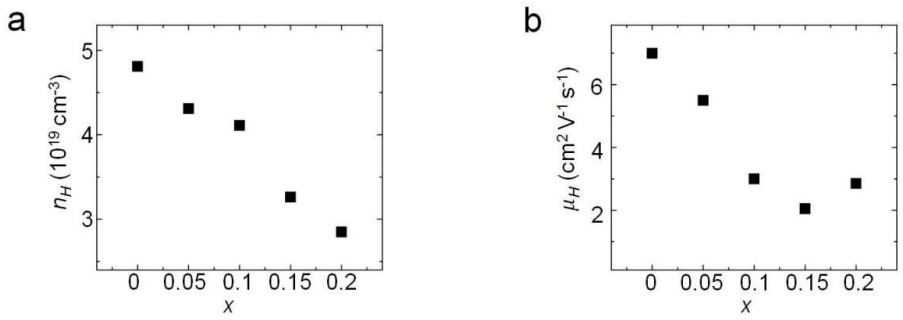

Figure 2.7. (a) Hall carrier concentration and (b) mobility at room temperature as a function of x for $Na_{0.01}(Sn_{1-x}Pb_x)_{0.99}Se$ (x = 0, 0.05, 0.1, 0.15, 0.2).

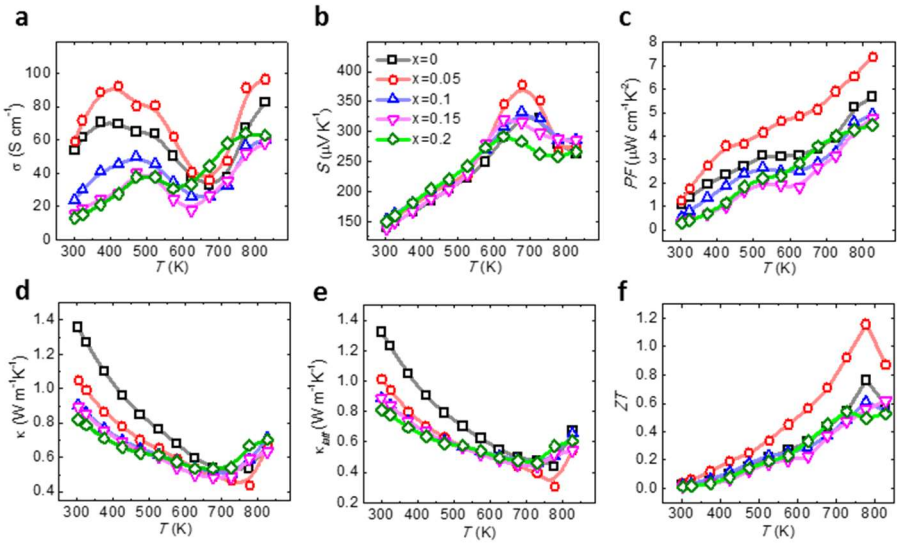

Figure 2.8. Temperature dependence of (a) electrical conductivity σ, (b) Seebeck coefficient *S*, (c) power factor *PF* (= σS^2), (d) total thermal conductivity κ_{tot}, (e) lattice thermal conductivity κ_{lat}, and (f) the TE figure of merit *ZT* of $Na_{0.01}(Sn_{1-x}Pb_x)_{0.99}Se$ (x = 0, 0.05, 0.1, 0.15, 0.2).

2.3.4 Thermoelectric Properties of $Na_{0.01}(Sn_{1-x}Pb_x)_{0.99}Se$ (x = 0, 0.03, 0.04, 0.05, 0.06)

We optimized $Na_{0.01}(Sn_{1-x}Pb_x)_{0.99}Se$ (x = 0, 0.03, 0.04, 0.05, and 0.06) system by controlling Pb incorporation delicately, considering the ZT of 1.16 at 773 K obtained from $Na_{0.01}(Sn_{0.95}Pb_{0.05})_{0.99}Se$. All samples show the "S-like" trend of $\sigma(T)$, but the σ value differs significantly by the alloying level of Pb both at 300 K and high-temperature (Figure 2.9a). It is remarkable that the Pb-incorporated samples show higher σ values at 773 K than $Na_{0.01}Sn_{0.99}Se$ whereas σ value of x = 0.06 at 300 K is nearly two times lower than that of $Na_{0.01}Sn_{0.99}Se$. The enhanced σ value by ~40 % at 773 K could be attributed to the decreased T_c by alloying Pb. The temperature-dependent Hall effect measurements for the representative samples of SnSe, $Na_{0.01}Sn_{0.99}Se$, $Sn_{0.96}Pb_{0.04}Se$, and $Na_{0.01}(Sn_{0.96}Pb_{0.04})_{0.99}Se$ provide deeper understanding for their electrical transport properties. The Hall coefficient $R_H(T)$ varies with temperature, indicative of multi-band electrical transport behavior (Figure 2.9b).

The n_H values is enhanced with rising temperature because of bipolar conduction and the effect is more evident for undoped SnSe and $Sn_{0.96}Pb_{0.04}Se$ than hole-doped $Na_{0.01}Sn_{0.99}Se$ and $Na_{0.01}(Sn_{0.96}Pb_{0.04})_{0.99}Se$ (Figure 2.9c). In the case of $Sn_{0.96}Pb_{0.04}Se$, the n_H value moderately increases from ~1.55×10^{17} to ~3.63×10^{17} cm^{-3} in the range of 300 – 523 K and subsequently rises up to ~2.38×10^{18} cm^{-3} at 673 K, which is similar trend to pristine SnSe. In contrast, for

$Na_{0.01}(Sn_{0.96}Pb_{0.04})_{0.99}Se$, the n_H value keeps nearly constant from 300 – 673 K, ranging between 1.07×10^{19} and 1.48×10^{19} cm^{-3}. The μ_H value increases with rising temperature from ~300 K to ~400 K and then decreases with further increase in temperature (Figure 2.9d). The abnormal rise of the μ_H value may be explained with a barrier-like scattering.[32] The corresponding S_{max} value is larger than $Na_{0.01}Sn_{0.99}Se$: ~380 μV K^{-1} at ~673 K for $Na_{0.01}(Sn_{0.95}Pb_{0.05})_{0.99}Se$ and ~320 μV K^{-1} at ~700 K for $Na_{0.01}Sn_{0.99}Se$ (Figure 2.9e). Such a difference could originate from the reduction in T_c by Pb alloying because the *Cmcm* phase could contribute to the increase in *S*. We compare the experimental *S* values at 300 K with the Pisarenko plot (Figure 2.9f) using two-band models[32] and full multivalley DFT band structure.[30] Experimental $S(n_H)$ values are roughly close to the Pisarenko line, indicating that multiple valence bands contribute to electrical transport properties of $Sn_{1-x}Pb_xSe$ and $Na_{0.01}(Sn_{1-x}Pb_x)_{0.99}Se$ mainly due to a very low energy separation (~0.02 eV) between the first two valence bands of SnSe.[30]

The highest *PF* of ~6.7 μW cm^{-1} K^{-2} at ~773 K for $x = 0.04$ is attributed to the combination of higher σ value and larger *S* value by reduced T_c via Pb incorporation, compared to $Na_{0.01}Sn_{0.99}Se$ (Figure 2.10a). The samples of $x = 0.04$, 0.05, and 0.06 show smaller κ_{tot} and κ_{lat} values persistently than $Na_{0.01}Sn_{0.99}Se$ over the entire temperature range (Figure 2.10b and 2.10c). $Na_{0.01}(Sn_{0.96}Pb_{0.04})_{0.99}Se$ exhibits the highest *ZT* of 1.18 at 773 K, which is enhanced by ~60% from pristine SnSe because of the simultaneous contributions from enhanced *PF* by decreased T_c

and reduced κ_{lat} by the effective point defect scattering due to the Pb alloying (Figure 2.10d).

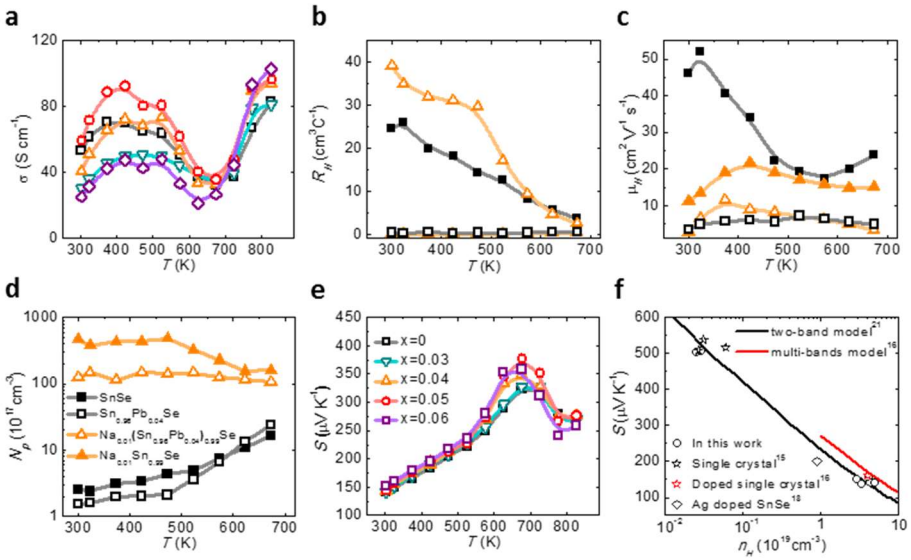

Figure 2.9. Temperature dependence of (a) electrical conductivity σ and (e) Seebeck coefficient S of $Na_{0.01}(Sn_{1-x}Pb_x)_{0.99}Se$ (x = 0, 0.03, 0.04, 0.05, 0.06), and temperature dependence of (b) Hall coefficient R_H, (c) hole concentration n_H, (d) hole mobility μ_H of SnSe, $Sn_{0.96}Pb_{0.04}Se$, $Na_{0.01}Sn_{0.99}Se$, and $Na_{0.01}(Sn_{0.96}Pb_{0.04})_{0.99}Se$, and (f) room temperature Seebeck coefficient S as a function of hole concentration (n_H).

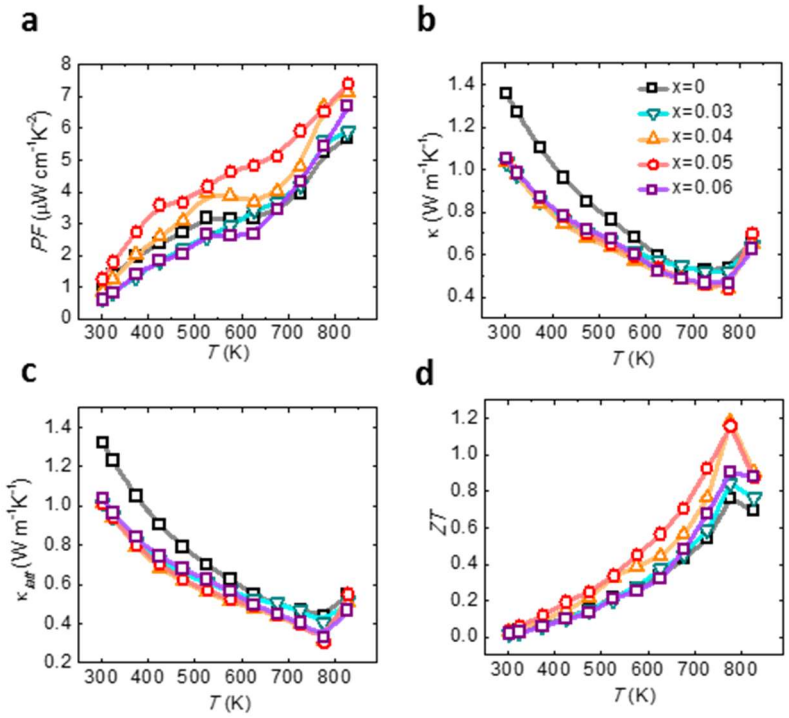

Figure 2.10. Temperature dependence of (a) power factor *PF* (= σS^2), (b) total thermal conductivity κ_{tot}, (c) lattice thermal conductivity κ_{lat}, and (d) the TE figure of merit *ZT* of $Na_{0.01}(Sn_{1-x}Pb_x)_{0.99}Se$ (x = 0, 0.03, 0.04, 0.05, 0.06).

2.3.5 Scanning Transmission electron microscopy (STEM)

We performed atomic resolution HAADF-STEM, EDS, and EELS studies to understand TE properties of $Na_{0.01}(Sn_{1-x}Pb_x)_{0.99}Se$. All specimens for TEM studies are dense pellets that are pressed by SPS. Typical cross-sectional bright-field (BF) STEM images of the SPS samples of $Sn_{0.96}Pb_{0.04}Se$ and $Na_{0.01}(Sn_{0.96}Pb_{0.04})_{0.99}Se$ viewed down the [010] axis demonstrate discernible nanoscale domains with a size of 5 – 10 nm evenly distributed in the matrix (Figures 2.12a and 2.12b). $Na_{0.01}(Sn_{0.96}Pb_{0.04})_{0.99}Se$ contains higher density of nanodots compared to $Sn_{0.96}Pb_{0.04}Se$. SnSe crystallizes in the GeS-type orthorhombic structure whereas PbSe adopt the rock salt-type cubic structure. According to the bulk phase diagram of two end members of SnSe and PbSe (Figure 2.11) as well as PXRD study discussed in this work, $Sn_{1-x}Pb_xSe$ ($x \leq 0.2$) solid solution is isostructural to SnSe. As a consequence, detailed characterization of crystal structure and compositional variance of such ubiquitous nanodots is essential to understand high TE performance of $Na_{0.01}(Sn_{1-x}Pb_x)_{0.99}Se$.

The selected area electron diffraction (SAED) pattern (inset of Figure 2.12b) on the $Na_{0.01}(Sn_{0.96}Pb_{0.04})_{0.99}Se$ demonstrates the diffraction spots based on SnSe-type structure along the [010] zone axis. Absence of extra diffraction spots exclude the presence of the second phase precipitates adopting PbSe-type rock-salt structure. Both high-magnification atomic-resolution high-angle annular dark-field (HAADF) and ABF-STEM images show that a higher intensity of signal, probably originated

from Pb-rich feature, is present across the nanodots compared to the matrix (Figures 2.12e and 2.12f). In addition, more irregular atomic arrangement near a nanoscale region is evident mainly due to compositional modulation between nanoscale region and matrix (inset of Figure 2.12f).

To probe compositional variance between the dots and the matrix, the STEM-energy dispersive X-ray spectroscopy (EDS) analysis was taken and it reveals that Pb is more abundant in the nanodots and Sn is richer in the surrounding matrix with no distinct difference in Se mol% in both regions (Figure 2.13). These observation demonstrates that both the nanodots and the matrix consists of $Sn_{1-x}Pb_xSe$ solid solution but abundance in Sn and Pb are different. This microscopic result confirms that nanoscale $Sn_{1-x}Pb_xSe$ solid solution also readily forms as bulk phase defined in phase diagram. A high-magnification annular BF STEM (ABF-STEM) image for $Na_{0.01}(Sn_{0.96}Pb_{0.04})_{0.99}Se$ focusing on the nanodots shows a coherent interface between nanodots and the matrix (Figure 2.12c). Edge dislocations marked by the red circle (top right inset, Figure 8c) are clearly observed in inverse fast Fourier transform (IFFT) image of (101) atomic planes (Figure 2.12d). In spite of the edge dislocations, the nanodots are almost coherent with the matrix. In the atomic scale, point defects by Pb substitution, lattice strain by solid solution, and mass fluctuation between the nanodots and the matrix could synergistically interrupt short-wavelength phonon transport while minimally affect hole carrier transport, explaining high σ and low κ_{lat} of $Na_{0.01}(Sn_{0.96}Pb_{0.04})_{0.99}Se$. If second phase

nanoprecipitates such PbSe formed, even lower thermal conductivity by additional mid-wavelength phonon scattering would be obtained to give higher *ZT* as shown in $Na_{1-x}Pb_xSe$ nanoparticles. The cross-sectional HAADF-STEM image taken on the nanodot of $Na_{0.01}(Sn_{0.96}Pb_{0.04})_{0.99}Se$ viewed down the b-axis clearly shows the layered structure based on SnSe. Because the contrast of HAADF-STEM image is approximately proportional to square of atomic number, apparently bigger and brighter atoms can be assigned to Sn or Pb and smaller and darker to Se (Figure 2.12g and 2.13). Elemental mapping STEM-EDS at the atomic level shows the atomic arrangements of the nanodots in $Na_{0.01}(Sn_{0.96}Pb_{0.04})_{0.99}Se$. Sn and Pb atoms that jointly contribute to red circles are totally disordered and the ordered PbSe is not observed. The green circles are Se atoms. Because Na is much lighter than other constituent elements, its presence and position could not be detected by STEM-EDS. Instead, we performed a STEM-EELS elemental scan profile at the atomic level to confirm the presence and relative location of sodium atoms in $Na_{0.01}(Sn_{0.96}Pb_{0.04})_{0.99}Se$. Figure 2.12k clearly shows the sodium $L_{2,3}$ edge of the EELS spectrum at 30 eV on $Na_{0.01}(Sn_{0.96}Pb_{0.04})_{0.99}Se$ confirming the presence of Na atoms, which is absent from the EELS spectrum of Na-free $Sn_{0.96}Pb_{0.04}Se$. The line profile of Na EELS across the nanodots and the matrix demonstrates that Na concentration is higher in the matrix than Pb-rich region.

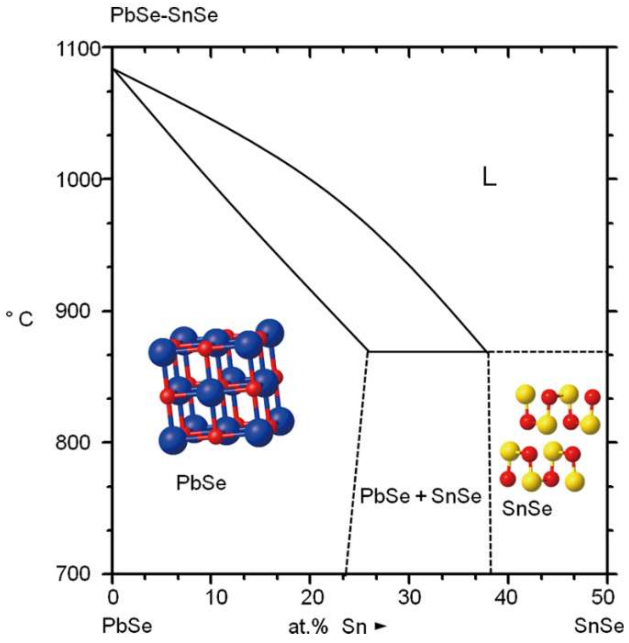

Figure 2.11. A bulk phase diagram of the PbSe-SnSe ternary system.

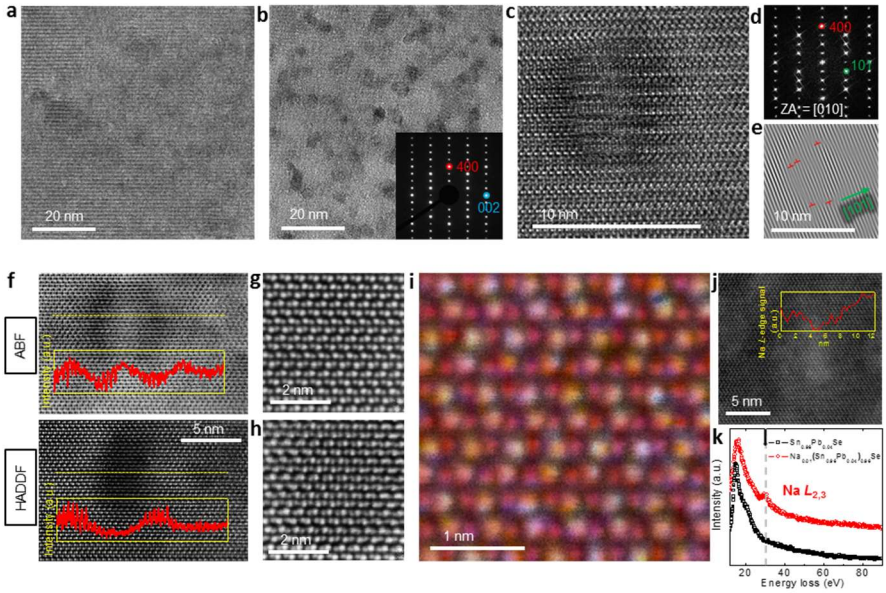

Figure 2.12. Cross-sectional scanning TEM (STEM) images of $Sn_{0.96}Pb_{0.04}Se$ and $Na_{0.01}(Sn_{0.96}Pb_{0.04})_{0.99}Se$, HAADF-STEM, ABF-STEM images, elemental mapping by STEM-EDS, and Na EELS data of $Na_{0.01}(Sn_{0.96}Pb_{0.04})_{0.99}Se$. (a) Typical bright-field (BF) STEM images of (a) $Sn_{0.96}Pb_{0.04}Se$, and (b) $Na_{0.01}(Sn_{0.96}Pb_{0.04})_{0.99}Se$. Inset: A selected area electron diffraction (SAED) pattern along [010] axis. (c) Magnified ABF-STEM image of a region containing nanodots for $Na_{0.01}(Sn_{0.96}Pb_{0.04})_{0.99}Se$. (d) A fast Fourier transform (FFT) image of (c) along [010] axis. (e) An inverse fast Fourier transform (IFFT) image of (101) atomic planes of (c). Red arrows indicate edge dislocations. (f) ABF-STEM and HAADF-STEM atomic-resolution images of a region including a nanodot for $Na_{0.01}(Sn_{0.96}Pb_{0.04})_{0.99}Se$. Inset: The signal intensity of Z-contrast is shown across nanodots as a line profile. (g) Magnified atomic-

resolution HAADF-STEM image of a matrix for $Na_{0.01}(Sn_{0.96}Pb_{0.04})_{0.99}Se$. (h) Magnified atomic-resolution HAADF-STEM image of a region including a nanodot for $Na_{0.01}(Sn_{0.96}Pb_{0.04})_{0.99}Se$. (i) A STEM-EDS elemental mapping of (h). (j) Line profile of Na EELS across nanodots for $Na_{0.01}(Sn_{0.96}Pb_{0.04})_{0.99}Se$. Inset: The signal intensity of Na *L*-edge is shown across nanodots as a line profile. (k) Na EELS data for $Sn_{0.96}Pb_{0.04}Se$ and $Na_{0.01}(Sn_{0.96}Pb_{0.04})_{0.99}Se$. The black arrow indicates an energy of Na $L_{2,3}$ edge.

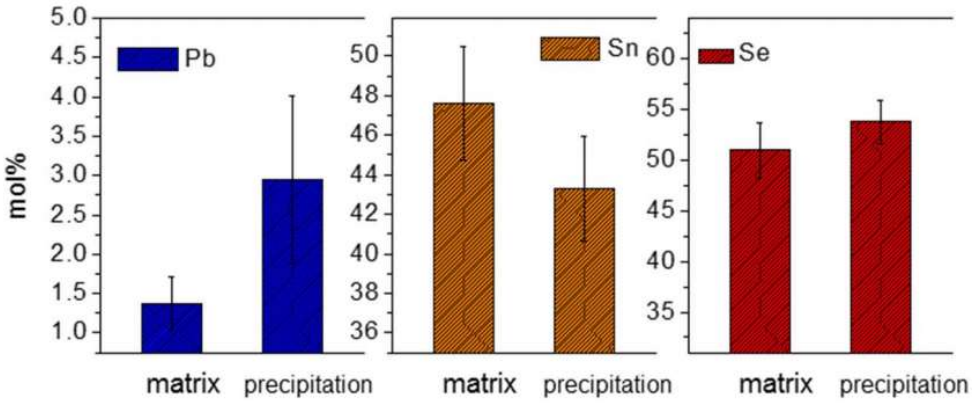

Figure 2.13. Elemental analysis on nanostructures and their surrounding matrix in the $Na_{0.01}(Sn_{0.96}Pb_{0.04})_{0.99}Se$ sample by STEM-EDS.

2.3.6 Theoretical calculation

To support this, we performed theoretical calculations on lattice thermal conductivities for the samples of pristine, Pb alloyed, and Na-doped and Pb alloyed SnSe with consideration of various well-known scattering mechanisms based on the models of Umklapp (U), Umklapp combined with point defects (U+PD), U+PD with interfaces, and U+PD with interfaces and dislocations. Figure 2.14 shows the calculated κ_{lat} curves in comparison with experimental values. The calculation results clearly demonstrate that experimental κ_{lat} values for Na doped and Pb alloyed samples are located well below the κ_{lat} curve based on the U +PD model over the entire temperature range, indicating multiple phonon scatterings occur. Considering both nano- structuring and dislocations observed in STEM studies in this work as the significant source of phonon scattering, our theoretical model fits well with experimental values.

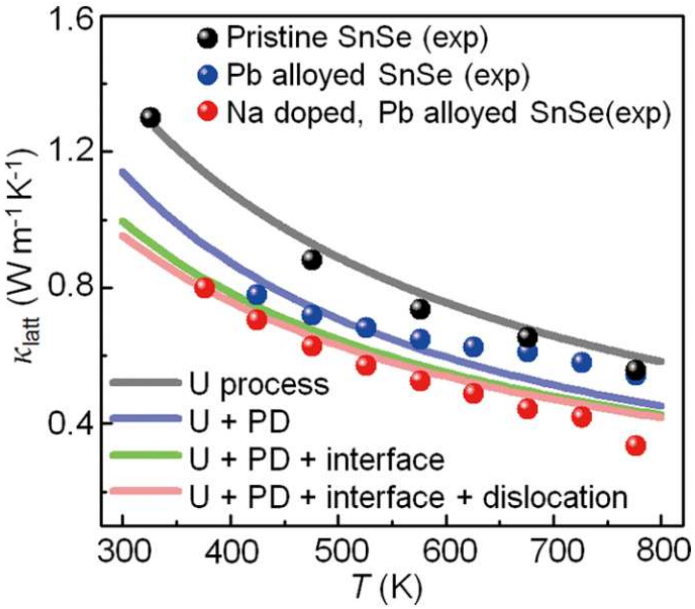

Figure 2.14. Calculated κ_{lat} with application of various scattering mechanisms in comparison with the experiment values for the samples of pristine SnSe, Pb alloyed $Sn_{0.95}Pb_{0.05}Se$, Na doped and Pb alloyed $Na_{0.01}(Sn_{0.95}Pb_{0.05})_{0.99}Se$.

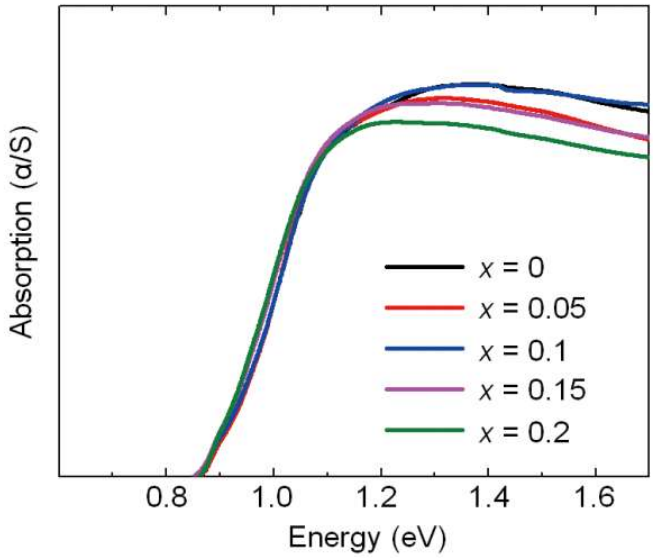

Figure 2.15. Optical absorption spectra of $Sn_{1-x}Pb_xSe$ (x = 0 – 0.2)

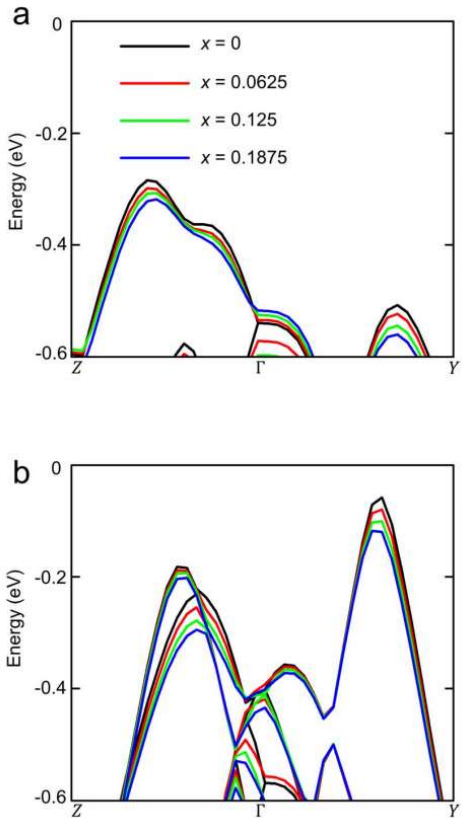

Figure 2.16. Electronic structures for (a) *Pnma* and (b) *Cmcm* of $Sn_{1-x}Pb_xSe$ (x = 0, 0.0625, 0.125, 0.1875) focused on the valence band maxima.

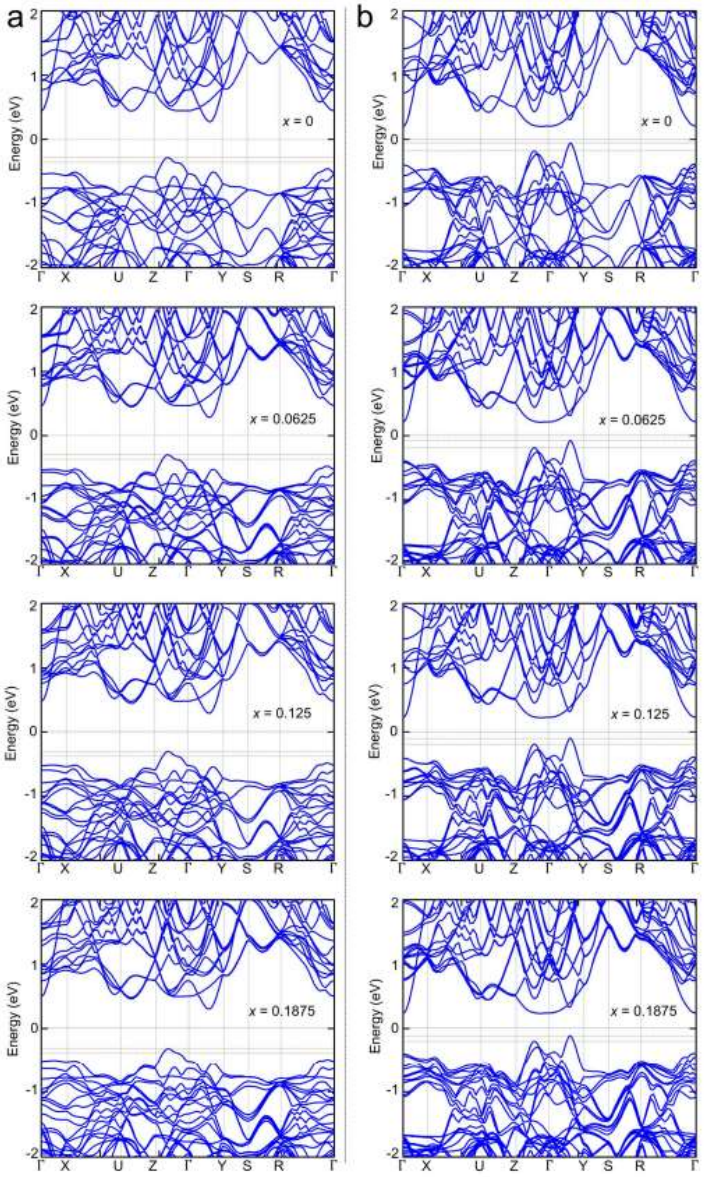

Figure 2.17. Electronic structures for (a) *Pnma* and (b) *Cmcm* of $Sn_{1-x}Pb_xSe$ (x = 0, 0.0625, 0.125, 0.1875)

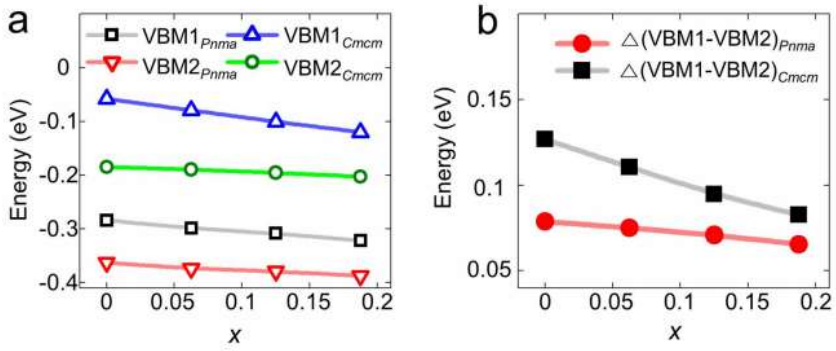

Figure 2.18. (a) The energy variations of the valence band maxima and (b) their differences as a function of *x* for $Sn_{1-x}Pb_xSe$ (x = 0, 0.0625, 0.125, 0.1875)

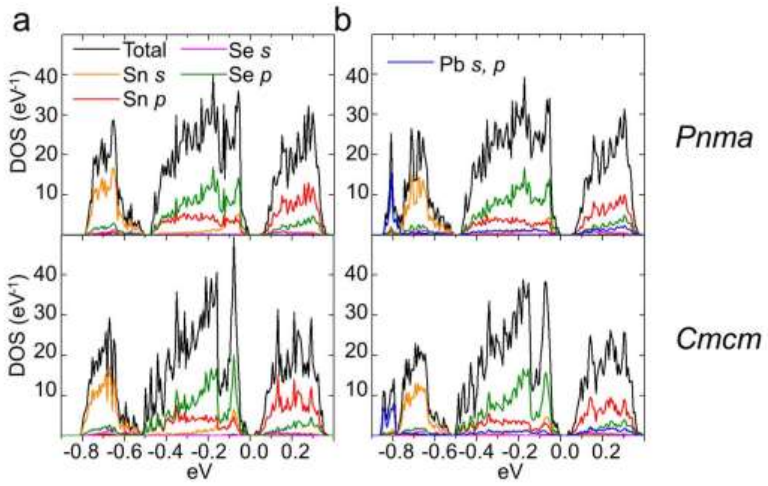

Figure 2.19. The projected density of states of *Pnma* and *Cmcm* phases of (a) SnSe and (b) $Sn_{0.8125}Pb_{0.1875}Se$

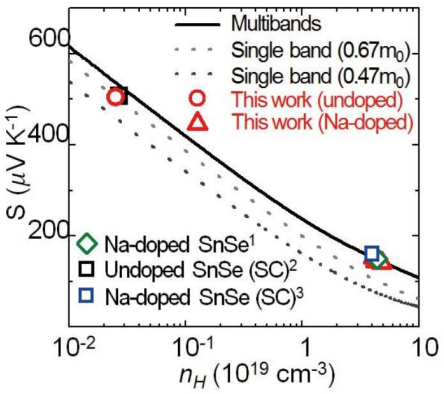

Figure 2.20. Seebeck coefficient as a function of hole concentration (n_H) at room temperature. We calculated the Pisarenko relation between S and n_H using a single parabolic band (SPB) and a multivalley band (MVB) models for SnSe, and compared the results with the experimental S values at 300 K for $Sn_{0.95}Pb_{0.05}Se$ and $Na_{0.01}(Sn_{0.95}Pb_{0.05})_{0.99}Se$ in this work as well as for the previous reports. The S values for undoped samples from this (i.e. $Sn_{0.95}Pb_{0.05}Se$) and the previous work are well fitted by the SPB model with the effective mass of $m = 0.67m_0$ (m_0: free electron mass). In contrast, those for Na-doped samples are close to the MVB model, suggesting that the presence of multiple valleys in the valence band plays an important role in Seebeck coefficients for this heavily doped system as reported previously. Since only 0.02 eV differs between the first light and heavy valence bands, the activated heavy valence band by hole doping can push the Fermi level down. However, PbSe alloying marginally affects S values, which is consistent with the results of our electronic structure calculations showing that it negligibly disturbs the VBM.

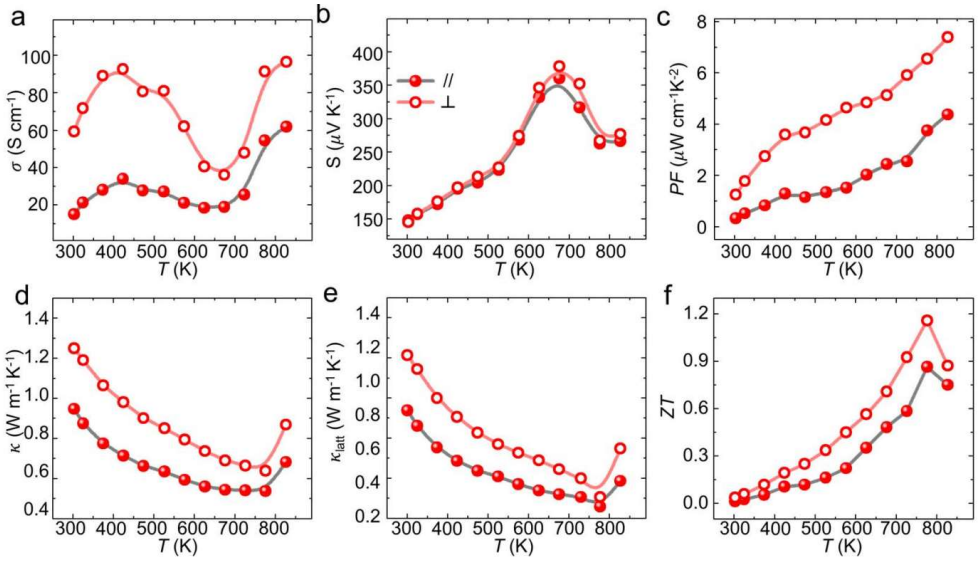

Figure 2.21. Temperature dependence of (a) electrical conductivity, (b) Seebeck coefficient, (c) power factor, (d) total thermal conductivity, (e) lattice thermal conductivity, and (f) figure of merit ZT of $Na_{0.01}(Sn_{0.95}Pb_{0.05})_{0.99}Se$ measured parallel (//) and perpendicular to the press direction (⊥) of spark plasma sintering.

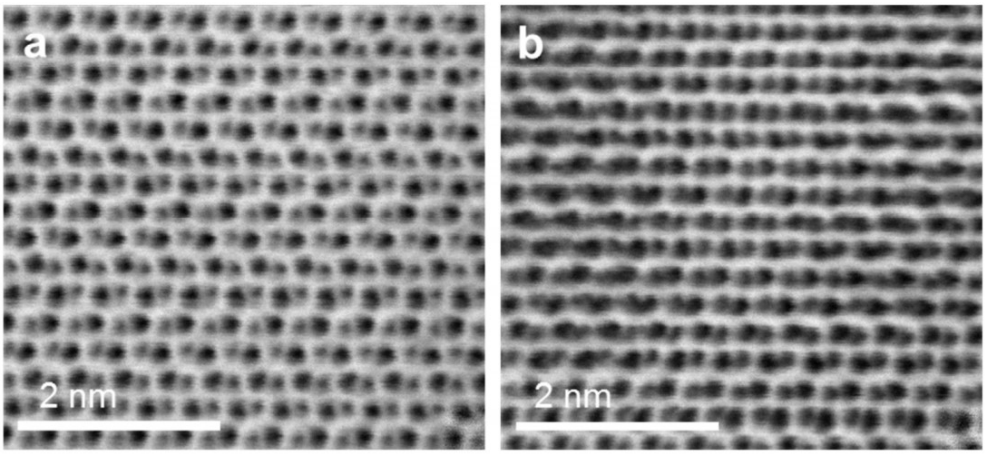

Figure 2.22. High-magnification atomic-resolution annular bright-field STEM image focusing on (a) the matrix and (b) the nanodot therein**.**

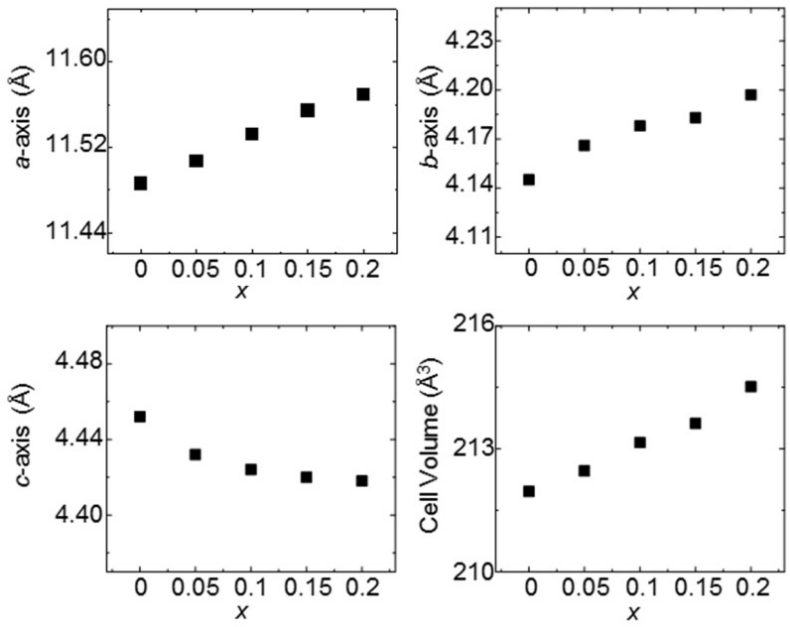

Figure 2.23. Lattice parameters and cell volume as a function of x for (a) $Sn_{1-x}Pb_xSe$ (x = 0, 0.05, 0.1, 0.15, 0.2) and (b)$Na_{0.01}(Sn_{1-x}Pb_x)_{0.99}Se$ (x = 0, 0.05, 0.1, 0.15, 0.2).

Table 2.1. Chemical compositions of the samples of $Sn_{1-x}Pb_xSe$ (x = 0, 0.05, 0.1, 0.15, 0.2) and $Na_{0.01}(Sn_{1-x}Pb_x)_{0.99}Se$ (x = 0, 0.05, 0.1, 0.15, 0.2) analyzed by electron probe micro-analysis (EPMA) and inductively coupled plasma atomic emission spectroscopy (ICP-AES). Standard deviation for analyzed compositions is given.

Nominal compositions	Analyzed compositions (EPMA+ICP-AES)
SnSe	$SnSe_{1.013(4)}$
$Sn_{0.95}Pb_{0.05}Se$	$Sn_{0.95}Pb_{0.051(1)}Se_{1.02(2)}$
$Sn_{0.9}Pb_{0.1}Se$	$Sn_{0.9}Pb_{0.100(1)}Se_{1.01(1)}$
$Sn_{0.85}Pb_{0.15}Se$	$Sn_{0.85}Pb_{0.152(1)}Se_{1.01(1)}$
$Sn_{0.8}Pb_{0.2}Se$	$Sn_{0.8}Pb_{0.199(2)}Se_{1.01(2)}$
$Na_{0.01}Sn_{0.99}Se$	$Na_xSn_{0.99}Se_{1.01(1)}$
$Na_{0.01}(Sn_{0.95}Pb_{0.05})_{0.99}Se$	$Na_{0.010(1)}(Sn_{0.95}Pb_{0.050(1)})_{0.99}Se_{1.01(2)}$
$Na_{0.01}(Sn_{0.9}Pb_{0.1})_{0.99}Se$	$Na_{0.010(1)}(Sn_{0.9}Pb_{0.100(1)})_{0.99}Se_{1.00(3)}$
$Na_{0.01}(Sn_{0.85}Pb_{0.15})_{0.99}Se$	$Na_{0.010(1)}(Sn_{0.85}Pb_{0.149(1)})_{0.99}Se_{1.00(2)}$
$Na_{0.01}(Sn_{0.8}Pb_{0.2})_{0.99}Se$	$Na_{0.010(1)}(Sn_{0.8}Pb_{0.192(3)})_{0.99}Se_{1.01(1)}$

Table 2.2. Apparent density of the samples of $Sn_{1-x}Pb_xSe$ (x = 0, 0.05, 0.1, 0.15, 0.2) and $Na_{0.01}(Sn_{1-x}Pb_x)_{0.99}Se$ (x = 0, 0.05, 0.1, 0.15, 0.2).

Nominal compositions	Density (g/cm^3)
SnSe	5.978
$Sn_{0.95}Pb_{0.05}Se$	6.190
$Sn_{0.9}Pb_{0.1}Se$	6.390
$Sn_{0.85}Pb_{0.15}Se$	6.445
$Sn_{0.8}Pb_{0.2}Se$	6.548
$Na_{0.01}Sn_{0.99}Se$	5.893
$Na_{0.01}(Sn_{0.95}Pb_{0.05})_{0.99}Se$	6.072
$Na_{0.01}(Sn_{0.9}Pb_{0.1})_{0.99}Se$	6.228
$Na_{0.01}(Sn_{0.85}Pb_{0.15})_{0.99}Se$	6.326
$Na_{0.01}(Sn_{0.8}Pb_{0.2})_{0.99}Se$	6.468

2.4 Conclusion

We find that Pb is not only an effective alloying element showing the solubility limit of ~20 % for Sn in SnSe, but the amount of Pb substitution also reduced the *Pnma*-to-*Cmcm* phase change temperature with a controllable manner ranging from 795 K to 730 K. A detailed STEM study reveals that there are prevalent $Sn_{1-x}Pb_xSe$ nanodots that are Pb-rich SnSe-PbSe solid solution compared to the matrix. These nanodots show coherent interfaces with the matrix, implying a facile charge transport and hard phonon transport. We demonstrate that both the enhancement in *PF* by reduced T_c and the reduction in κ_{lat} by alloy scattering simultaneously work for Na-doped $Sn_{1-x}Pb_xSe$ system. Consequently, the 1% Na and 4 % Pb codoped SnSe shows the enhancement in the *PF* value (~6.7 μW cm^{-1} K^{-2}) at ~773 K by ~30% and the reduction in the κ_{lat} value (~0.31 W m^{-1} K^{-1}) at ~773 K by ~30% compared to $Na_{0.01}Sn_{0.99}Se$. A maximum *ZT* of ~1.2 was achieved at ~773 K for $Na_{0.01}(Sn_{0.96}Pb_{0.04})_{0.99}Se$, being 50 – 70 % higher than SnSe (*ZT* ~ 0.7) and $Na_{0.01}Sn_{0.99}Se$ (*ZT* ~ 0.8), indicating that the adjustment of T_c in SnSe is effective for a significant enhancement in *ZT*.

2.5 References

1. Bell, L. E., *Science* **2008,** *321* (5895), 1457-1461.

2. Zeier, W. G.; Zevalkink, A.; Gibbs, Z. M.; Hautier, G.; Kanatzidis, M. G.; Snyder, G. J., *Angew. Chem. Int. Ed.* **2016,** *55* (24), 6826-6841.

3. Tan, G.; Zhao, L. D.; Kanatzidis, M. G., *Chem Rev* **2016,** *116* (19), 12123-12149.

4. Hsu, K. F.; Loo, S.; Guo, F.; Chen, W.; Dyck, J. S.; Uher, C.; Hogan, T.; Polychroniadis, E. K.; Kanatzidis, M. G., *Science* **2004,** *303* (5659), 818-821.

5. He, J.; Sootsman, J. R.; Girard, S. N.; Zheng, J.-C.; Wen, J.; Zhu, Y.; Kanatzidis, M. G.; Dravid, V. P. *J. Am. Chem. Soc*. **2010**, *132*, 8669.

6. Vineis, C. J.; Shakouri, A.; Majumdar, A.; Kanatzidis, M. G. *Adv. Mater*. **2010**, *22*, 3970.

7. Biswas, K.; He, J.; Zhang, Q.; Wang, G.; Uher, C.; Dravid, V. P.; Kanatzidis, M. G., *Nat Chem* **2011,** *3* (2), 160-166.

8. Zhao, L. D.; Lo, S. H.; He, J.; Li, H.; Biswas, K.; Androulakis, J.; Wu, C. I.; Hogan, T. P.; Chung, D. Y.; Dravid, V. P.; Kanatzidis, M. G. *J. Am. Chem. Soc*. **2011**, *133*, 20476.

9. Zhao, L. D.; He, J.; Wu, C. I.; Hogan, T. P.; Zhou, X.; Uher, C.; Dravid, V. P.; Kanatzidis, M. G. *J. Am. Chem. Soc*. **2012**, *134*, 7902.

10. Zhao, L. D.; He, J.; Hao, S.; Wu, C. I.; Hogan, T. P.; Wolverton, C.; Dravid, V. P.; Kanatzidis, M. G. *J. Am. Chem. Soc*. **2012**, *134*, 16327.

11. He, J.; Zhao, L.-D.; Zheng, J.-C.; Doak, J. W.; Wu, H.; Wang, H.-Q.; Lee, Y.; Wolverton, C.; Kanatzidis, M. G.; Dravid, V. P. *J. Am. Chem. Soc*. **2013**, *135*, 4624.

12. Tan, G.; Zhao, L.-D.; Shi, F.; Doak, J. W.; Lo, S.-H.; Sun, H.; Wolverton, C.; Dravid, V. P.; Uher, C.; Kanatzidis, M. G. *J. Am. Chem. Soc*. **2014**, *136*, 7006.

13. Zhao, L.-D.; Zhang, X.; Wu, H.; Tan, G.; Pei, Y.; Xiao, Y.; Chang, C.; Wu, D.; Chi, H.; Zheng, L.; Gong, S.; Uher, C.; He, J.; Kanatzidis, M. G. *J. Am. Chem. Soc*. **2016**, *138*, 2366−2373.

14. Biswas, K.; He, J.; Blum, I. D.; Wu, C.-I.; Hogan, T. P.; Seidman, D. N.; Dravid, V. P.; Kanatzidis, M. G., *Nature* **2012,** *489* (7416), 414-418.

15. Lee, Y.; Lo, S. H.; Androulakis, J.; Wu, C. I.; Zhao, L. D.; Chung, D. Y.; Hogan, T. P.; Dravid, V. P.; Kanatzidis, M. G. *J. Am. Chem. Soc.* **2013**, *135*, 5152.

16. Zhao, L. D.; Hao, S. Q.; Lo, S. H.; Wu, C. I.; Zhou, X. Y.; Lee, Y.; Li, H.; Biswas, K.; Hogan, T. P.; Uher, C.; Wolverton, C.; Dravid, V. P.; Kanatzidis, M. G. *J. Am. Chem. Soc*. **2013**, *135*, 7364.

17. Brown, S. R.; Kauzlarich, S. M.; Gascoin, F.; Snyder, G. J., *Chem. Mater.*

2006, *18* (7), 1873-1877.

18. Kurosaki, K.; Kosuga, A.; Muta, H.; Uno, M.; Yamanaka, S., *Appl Phys Lett* **2005,** *87* (6), 061919.

19. Rhyee, J. S.; Lee, K. H.; Lee, S. M.; Cho, E.; Il Kim, S.; Lee, E.; Kwon, Y. S.; Shim, J. H.; Kotliar, G., *Nature* **2009,** *459* (7249), 965-968.

20. Heremans, J. P.; Jovovic, V.; Toberer, E. S.; Saramat, A.; Kurosaki, K.; Charoenphakdee, A.; Yamanaka, S.; Snyder, G. J., *Science* **2008,** *321* (5888), 554-557.

21. Heremans, J. P.; Wiendlocha, B.; Chamoire, A. M., *Energy Environ. Sci.* **2012,** *5* (2), 5510-5530.

22. Tan, G.; Shi, F.; Hao, S.; Chi, H.; Bailey, T. P.; Zhao, L.-D.; Uher, C.; Wolverton, C.; Dravid, V. P.; Kanatzidis, M. G. *J. Am. Chem. Soc*. **2015**, *137*, 11507.

23. Pei, Y. Z.; Shi, X. Y.; LaLonde, A.; Wang, H.; Chen, L. D.; Snyder, G. J., *Nature* **2011,** *473* (7345), 66-69.

24. Hicks, L. D.; Dresselhaus, M. S., *Phys Rev B* **1993,** *47* (19), 12727-12731.

25. Heremans, J. P.; Thrush, C. M.; Morelli, D. T., *Phys Rev B* **2004,** *70* (11), 115334.

26. Zhao, L. D.; Lo, S. H.; Zhang, Y.; Sun, H.; Tan, G.; Uher, C.; Wolverton, C.; Dravid, V. P.; Kanatzidis, M. G., *Nature* **2014,** *508* (7496), 373-377.

27. Chattopadhyay, T.; Pannetier, J.; Vonschnering, H. G., *J. Phys. Chem. Solids*

1986, *47* (9), 879-885.

28. Peters, M. J.; Mcneil, L. E., *Phys Rev B* **1990,** *41* (9), 5893-5897.

29. Baumgardner, W. J.; Choi, J. J.; Lim, Y. F.; Hanrath, T., *J Am Chem Soc* **2010,** *132* (28), 9519-9521.

30. Zhao, L. D.; Tan, G. J.; Hao, S. Q.; He, J. Q.; Pei, Y. L.; Chi, H.; Wang, H.; Gong, S. K.; Xu, H. B.; Dravid, V. P.; Uher, C.; Snyder, G. J.; Wolverton, C.; Kanatzidis, M. G., *Science* **2016,** *351* (6269), 141-144.

31. Sassi, S.; Candolfi, C.; Vaney, J.-B.; Ohorodniichuk, V.; Masschelein, P.; Dauscher, A.; Lenoir, B., *Appl Phys Lett* **2014,** *104* (21), 212105.

32. Chen, C. L.; Wang, H.; Chen, Y. Y.; Day, T.; Snyder, G. J., *J. Mater. Chem. A* **2014,** *2* (29), 11171-11176.

33. Zhang, Q.; Chere, E. K.; Sun, J. Y.; Cao, F.; Dahal, K.; Chen, S.; Chen, G.; Ren, Z. F., *Adv Energy Mater* **2015,** *5* (12), 1500360.

34. Tang, G.; Wei, W.; Zhang, J.; Li, Y.; Wang, X.; Xu, G.; Chang, C.; Wang, Z.; Du, Y.; Zhao, L.-D., *J Am Chem Soc* **2016,** *138* (41), 13647-13654.

35. Wei, T. R.; Tan, G. J.; Zhang, X. M.; Wu, C. F.; Li, J. F.; Dravid, V. P.; Snyder, G. J.; Kanatzidis, M. G., *J Am Chem Soc* **2016,** *138* (28), 8875-8882.

36. Chen, Y. X.; Ge, Z. H.; Yin, M. J.; Feng, D.; Huang, X. Q.; Zhao, W. Y.; He, J. Q., *Adv. Funct. Mater.* **2016,** *36* (37), 6836-6845.

37. Woolley, J. C.; Berolo, O., *Mater Res Bull* **1968,** *3* (5), 445-450.

38. Volykhov, A. A.; Shtanov, V. I.; Yashina, L. V., *Inorg Mater* **2008,** *44* (4), 345-

356.

39. Shannon, R. D., *Acta Crystallogr A* **1976,** *32*, 751-767.

40. Atkins, P.; de Paula, J., *Physical Chemistry*. Oxford University Press: 2006.

41. Zhao, L.-D.; Chang, C.; Tan, G.; Kanatzidis, M. G., *Energy Environ. Sci.* **2016,** *9* (10), 3044-3060.

42. Toberer, E. S.; Zevalkink, A.; Snyder, G. J., *J. Mater. Chem.* **2011,** *21* (40), 15843-15852.

Chapter 3. Defect engineering for high-performance SnSe thermoelectrics

3.1 Introduction

Thermoelectric (TE) technology can directly produce electrical potential through temperature gradients, and plays a big role in recovering waste heat and consequently increasing overall energy efficiency [1] [2] [3]. The technology is green, noiseless and free of moving parts, making it the next generation energy harvesting technology. For thermoelectric materials, semiconductors are generally used, and their thermoelectric performance is expressed through a dimensionless figure of merit ZT = $S^2\sigma T/\kappa_{tot}$, where S is the Seebeck coefficient, σ is the electrical conductivity, their product is the power factor (PF), T is absolute temperature, and κ_{tot} is the total thermal conductivity which is sum of electronic(κ_{ele}) and lattice(κ_{lat}) thermal conductivity.

Recently, single crystal SnSe reported a high thermoelectric figure of merit ZT of 2.6 at 923 K as a result of ultralow thermal conductivity [4]. Polycrystalline type SnSe research is required for scale-up and commercialization, and is currently being actively researched[5]. However, since thermoelectric performance is lower than that of single crystal, further research is required [6]. The biggest factor of low performance is higher thermal conductivity than single crystal.

There are two strategies to reduce the thermal conductivity of polycrystalline SnSe.

First, it is to identify the cause of the high thermal conductivity of polycrystalline SnSe compared to the single crystal. We recently discovered that the cause is due to Sn oxide, and has reported a study of the thermal conductivity and thermoelectric performance of the single crystal level through the ball mill and the reduction process. Second is to reduce the thermal conductivity through extrinsic factors. Already studied thermoelectric materials such as Bi_2Te_3, PbSe, and PbTe have increased phonon scattering through strategies such as alloying, nanostructuring[7,8], hierarchiral architectures [9,10], and atomic discordant [11], thereby reducing thermal conductivity. In recent years, defect engineering strategies have come into the spotlight [12,13,14], creating a predecessor network within the grain to induce stress in the lattice to independently lower thermal conductivity while minimizing the effect on electrical transport properties. The introduction of these defects not only leads to scattering caused by defects at the atomic level, but also forms nano- and micro-scale defects by forming energetically stable structures, and can cause phonon scattering in a wide wavelength range. Since SnSe is an orthorhombic structure unlike the isotropic structure material to which the strategy is mainly applied, it is difficult to grow dislocation in a random direction, and it has been considered that doping or alloying has a more difficult crystal structure than other materials.

In this study, the cation composition defect and indium were intentionally introduced in the synthesis. Annealing above the phase transition temperature resulted in the most energy stable structure, and STEM observation revealed that the

microstructure changes with annealing time. Nanostructures of In_2Se_3 with several nanometers of thickness and lengths of several nanometers were formed, which maximize the scattering of phonons to achieve thermal conductivity similar to that of single crystals. In addition, the introduction of Indium improves the Seebeck coefficient through the change of the electronic band structure, thereby minimizing the reduction of the power factor despite the low thermal conductivity. As a result of this strategy, a high ZT performance of 2.0 was recorded.

3.2 Experimental section

Reagents. The following reagents were used as obtained unless note otherwise: Sn chunk (99.999% American Elements, US), Se shot (99.999% 5N Plus, Canada), Na pieces (99.9%, Sigma-Aldrich, US), and In shot (99.9%, American Elements, US).

Synthesis. To synthesize polycrystalline SnSe ingots a stoichiometric mixture of constituent elements were loaded to an evacuated fused silica tube (~ 10^{-4} Torr). To preventing glass attack, carbon coated silica tube used. The total weight of starting materials was typically ~13 g. The sealed tube was placed in the furnace and heated to 1223 K for 24 h and quenching in the cold water. The reaction tube was inserted into a larger evacuated silica tube to protect the material from oxidation in the case of cracks of the inner tube due to the phase transition during annealing process. The double sealed tube was heated to 823 K for a certain time and cooling naturally. The obtained ingot was powdered by a mechanical grinder, sieved to under 45 μm.

Compacting powders. Powders were loaded in a BN-coated graphite die in an Ar-filled glovebox and cold-pressed manually. The die was taken out of the glovebox and placed in a spark plasma sintering (SPS) system (SPS-211Lx, Fuji Electronic Industrial Co., Japan) under an Ar flow (99.99% purity). Powder samples in the die were densified at ~ 783 K for 5 min under an axial pressure of 50 MPa in a vacuum of ~ 1.4×10^{-2} Torr using SPS. Typical images of SPS-processed pellets and their dimensions are given in Figure.

Powder X-ray diffraction (XRD). Powder XRD analysis was performed using a SmartLab Rigaku powder X-ray diffractometer (Cu Kα graphite-monochromatized radiation) operating at 40 kV and 30 mA at room temperature.

UV-vis spectroscopy. Optical absorption measurement was performed on powders by using the UV-Vis-NIR spectrophotometer (Shimadzu UV-3600 Plus) at room temperature.

Emission electron probe micro analyzer (EPMA). The elements distribution analysis was characterized using a JEOL JXA-8530FPlus Hyper Probe field emission operating at 15 kV at room temperature.

Thermogravimetric analysis (TGA) The thermogravimetric analysis was conducted by a Netzsch TG 209 F1 Libra in alumina crucible under a Ar flow, in the temperature range from room temperature to 823 K with a rate of 10 K min^{-1}

Electrical and thermal transport property measurements. The samples after SPS

were cut and polished into a rectangular shape with a length of 13 mm and thickness of ~ 2 mm under a N_2 atmosphere. The electrical conductivity and Seebeck coefficient were measured simultaneously under an Ar atmosphere from room temperature to 823 K using a Netzsch SBA 458 Nemesis system. Temperature-dependent Hall coefficients (R_H) of the samples were measured by a Lake Shore HMS8407 Hall effect measurement system in a magnetic field of 1.5 T. The hole carrier concentration (n_H) and hole mobility (μ_H) were calculated by $n_H = 1/(e \cdot R_H)$ and $\mu_H = R_H \cdot \sigma$, respectively. A Netzsch LFA 457 MicroFlash instrument was used to measure the thermal diffusivity of the samples coated with graphite. The thermal conductivity was calculated from $\kappa_{tot} = D \cdot C_p \cdot \rho$, where D is the thermal diffusivity, C_p is the heat capacity, and ρ is the mass density of the specimens. The temperature-dependent C_p values were indirectly derived using a standard sample (Pyroceram). The ρ values used were obtained using their geometrical dimensions and masses). The total thermal conductivity κ_{tot} is the sum of the lattice (κ_{lat}) and electronic thermal (κ_{ele}) conductivities. κ_{ele} is proportional to the electrical conductivity (σ) according to the Wiedemann−Franz law ($\kappa_{ele} = L \cdot \sigma \cdot T$), where L is the temperature-dependent Lorenz number and T is the absolute temperature. An L value as a function of temperature were obtained from previous studies. The κ_{lat} value was estimated by subtracting the κ_{ele} value from the κ_{tot} value: $\kappa_{lat} = \kappa_{tot} - \kappa_{ele}$.

Transmission electron microscopy. Cross-sectional samples for scanning TEM (STEM) were prepared by focused ion beams (FIB, Helios 650, FEG, FEI) with a

dual beam microscope using gallium ion milling. Before the ion milling process, carbon was sputtered to preserve the sample by surface coating. The specimens were further polished with a low-voltage and low-angle argon ion beam milling apparatus (NANO MILL, Model 1040, FISCHIONE). The atomic structure and chemical composition were investigated employing a spherical aberration-corrected JEM ARM-200F microscope (Cold FEG Type, JEOL) equipped with a SDD type energy dispersive X-ray spectroscopy (EDS) detector (Solid Angle 0.9-sr, X-MaxN 100TLE, OXFORD) and electron energy loss spectroscopy (EELS) detector (965 GIF Quantum ER, GATAN) at 200 kV, which are installed at the National Center for Inter-university Research Facilities (NCIRF) at Seoul National University. In the high-angle annular dark-field (HAADF) STEM images, the point-to-point resolution was approximately 80 pm after the Cs-correction, and the angular range of the annular detector used was 68 mrad to 280 mrad. All images were recorded by a high-resolution CCD detector using a 2 k × 2 k pixel device (UltraScan 1000, GATAN). For STEM-EDS analyses, chemical maps were taken with a probe size of 0.13 nm and a probe current of 40 pA. For STEM-EELS measurements, the energy dispersion was set at 0.1 eV ch^{-1}. The full-width at half-maximum of the zero-loss peak in vacuum was 0.8 eV. The convergence and collection semiangles were 19 and 19.8 mrad, respectively.

3.3 Results and discussion

As a first variable, samples were constructed by varying the vacancy content. As a result of analyzing all samples synthesized through XRD pattern analysis, it was confirmed that all samples did not have different impurity phases and showed the structure of SnSe, *Pnma* (Figure 3.1). In addition, cell parameters and cell volume tended to decrease as vacancy was introduced (Table 3.1). Figure 3.2 shows the thermoelectric properties of $Na_{0.01}(Sn_{1-x}In_{0.01})_{0.99}Se$ (Figure 3.2). In the case of a sample in which vacancy is introduced, a sample with x=0.03 has a lower electrical conductivity than a $Na_{0.01}Sn_{0.99}Se$ sample. However, all indium-containing samples have a higher Seebeck coefficient. In the Pisarenko plot, the Seebeck coefficient of the sample containing all indium is located close to the multiband, not the single band (Figure 3.3). Due to the enhancement effect of the Seebeck coefficient, x=0.03 samples showed the highest power factor of 6 $\mu W\ cm^{-1}K^{-2}$ in all sample groups. Also, as the content of vacancy increases, the thermal conductivity tends to decrease. The lattice thermal conductivity excluding the electronic thermal conductivity also tends to decrease according to the vacancy content. The sample with x=0.03 showed a ZT value of about 2.0 through improved power factor and reduced thermal conductivity. Therefore, it was confirmed that x=0.03 is the optimal composition for high ZT.

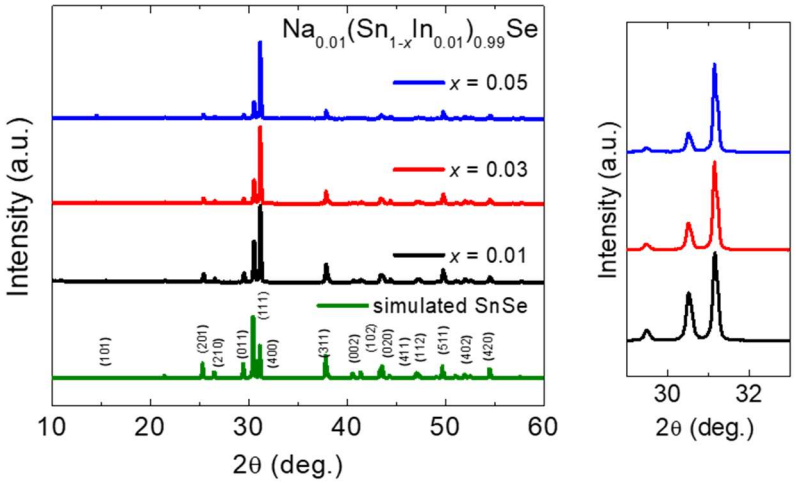

Figure 3.1. Powder X-ray diffraction patterns of $Na_{0.01}(Sn_{1-x}In_{0.01})_{0.99}Se$ (x = 0.01, 0.03, 0.05) in comparison with that of the theoretical calculation for SnSe (The International Centre for Diffraction Data (ICDD) PDF 01-075-6133). SPS processed ingots were ground to fine powders for the measurement.

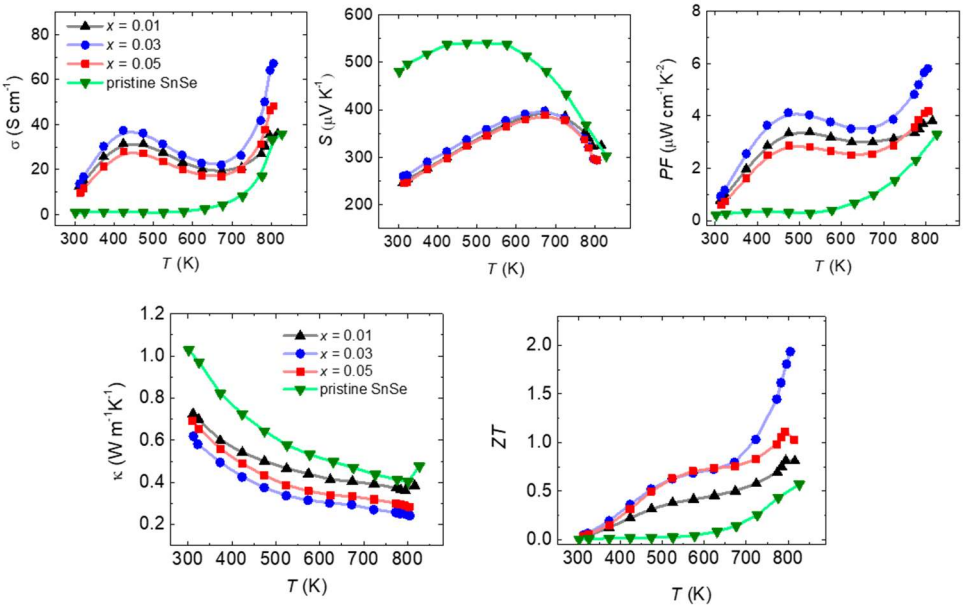

Figure 3.2. Temperature dependence of (a) electrical conductivity σ, (b) Seebeck coefficient *S*, (c) power factor *PF* (= σS^2), (d) total thermal conductivity κ_{tot}, (e) the TE figure of merit *ZT* of $Na_{0.01}(Sn_{1-x}In_{0.01})_{0.99}Se$ (x = 0.01, 0.03, 0.05)**.**

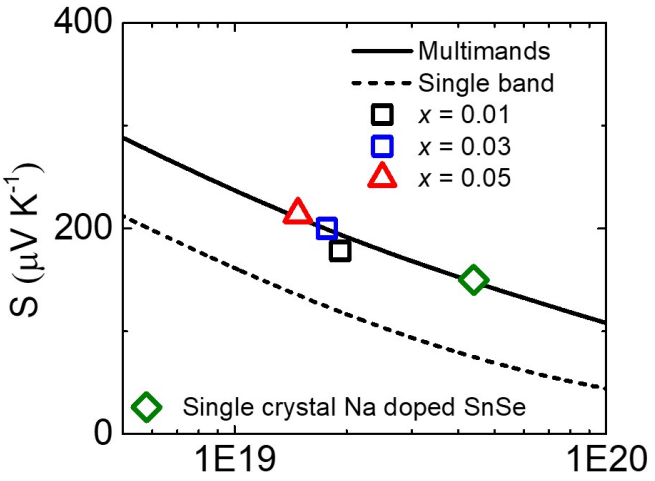

Figure 3.3. Seebeck coefficient as a function of hole concentration (n_H) at room temperature. We calculated the Pisarenko relation between S and n_H using a single parabolic band (SPB) and a multivalley band (MVB) models for SnSe, and compared the results with the experimental S values at 300 K for $Na_{0.01}(Sn_{1-x}In_{0.01})_{0.99}Se$ (x = 0.01, 0.03, 0.05)**.**

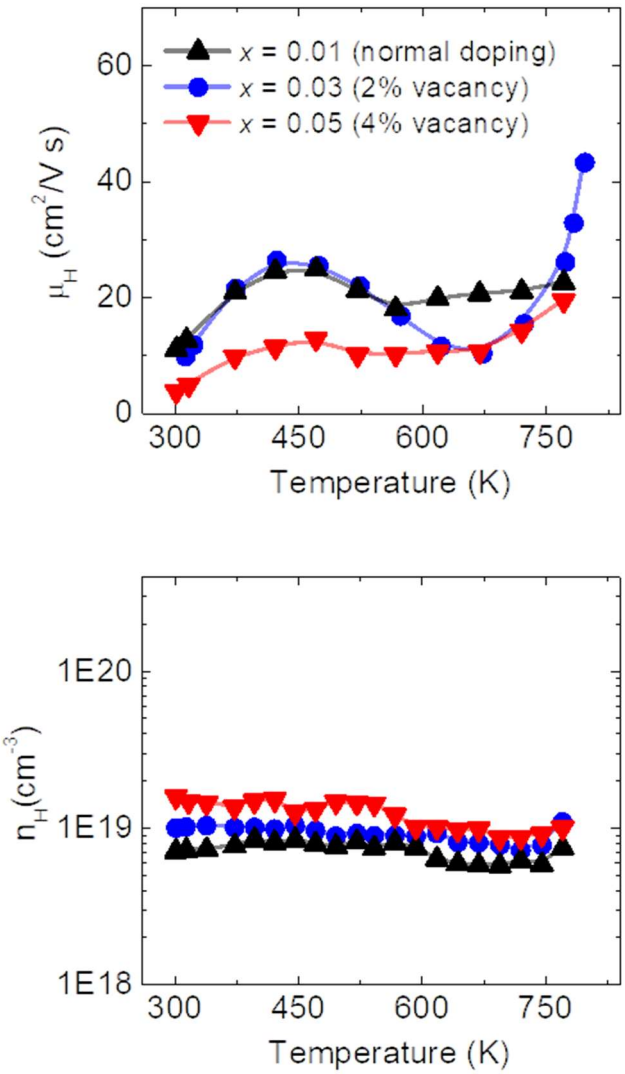

Figure 3.4. Temperature-dependent carrier mobility and carrier concentration for $Na_{0.01}(Sn_{1-x}In_{0.01})_{0.99}Se$ (x = 0.01, 0.03, 0.05)**.**

Table 3.1. Cell parameters and cell volume of $Na_{0.01}(Sn_{1-x}In_{0.01})_{0.99}Se$.

Sample	a(Å)	b(Å)	c(Å)	Volume(Å^3)
SnSe	11.4943	4.1526	4.4346	211.67
$Na_{0.01}Sn_{0.99}Se$	11.4959	4.1517	4.4365	211.74
$Na_{0.01}(Sn_{0.99}In_{0.01})_{0.99}Se$	11.5030	4.1559	4.4432	212.41
$Na_{0.01}(Sn_{0.97}In_{0.01})_{0.99}Se$	11.4999	4.1541	4.4417	212.19
$Na_{0.01}(Sn_{0.95}In_{0.01})_{0.99}Se$	11.4990	4.1534	4.4409	212.10

In additional experiments, it was confirmed that even if the composition was the same, the thermal conductivity decreased with annealing time. Through this, a new sample group was constructed using the time of annealing as a variable.

The composition of $Na_{0.01}(Sn_{0.97}In_{0.01})_{0.99}Se$ was synthesized and samples were prepared according to the annealing time at 823 K after quenching. All samples don't show any difference in the XRD pattern with annealing time and any impurity phases are not shown (Figure 3.5). The scanning transmission energy microscopy images according to the annealing time is presented in Figure 3.6. In order to prevent damage and deformation of the sample during the observation, observation was carried out with a composition except for Na, $Sn_{0.97}In_{0.01}Se$. as-quenched sample shows a number of point defects over the entire surface (Figure 3.6a). The aliovalent impurities such as Indium or vacancies constitute the point defects. Some points defects are arrayed. The sample annealed for 12 hours the similar arrangement with as-quenched sample. However, each defect forms line defect which length is tens-of-nanometer. After 24 hours annealing, the short-line defects are connected and forms several hundred nanometer line defects. The number of short line defects decreases compared to the as-quenched and 12 hours annealed sample. All line defects are aligned in the same direction. In the sample annealed for 48 hours, long bands are formed along the same direction. in the low-mag images of the sample (Figure 3.7), several bands are presented over the entire grain and the length of the lines are several micrometers. The 96 hours annealed sample also has band

microstructure but more fully formed than the 48 hours annealed sample. Further, the number of vacancy clusters around the band is reduced. This observation clearly shows that with increase of annealing time, the microstructure of SnSe changes significantly, from well-distributed vacancy clusters to aligned band formed by secondary phases along the specific direction.

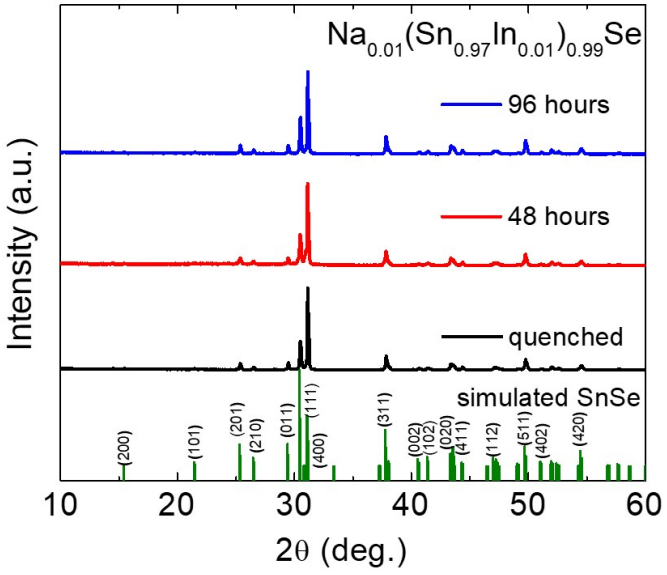

Figure 3.5. Powder X-ray diffraction patterns of $Na_{0.01}(Sn_{0.97}In_{0.01})_{0.99}Se$ according to the annealing time in comparison with that of the theoretical calculation for SnSe (The International Centre for Diffraction Data (ICDD) PDF 01-075-6133). SPS processed ingots were ground to fine powders for the measurement.

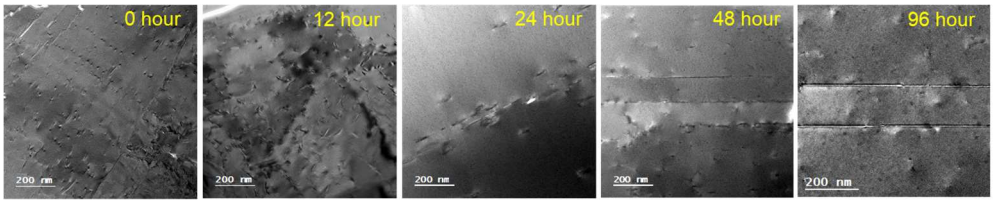

Figure 3.6. Cs corrected scanning transmission electron microscope (STEM) images of $Sn_{0.97}In_{0.01}Se$ sample according to the annealing time. a) as-quenched, b) 12 hours, c) 24 hours, d) 48 hours and e) 96 hours annealed sample.

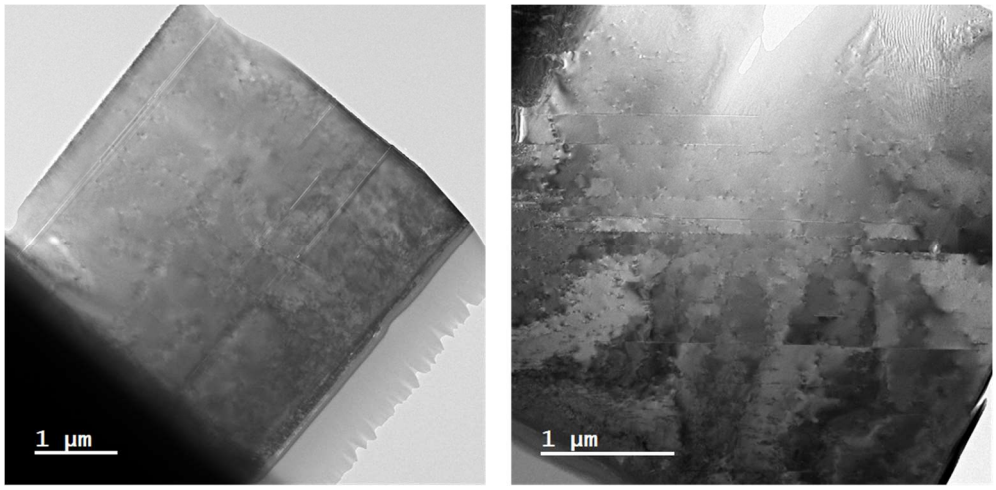

Figure 3.7. Typical low-magnification images of STEM for $Sn_{0.97}In_{0.01}Se$**.**

As-quenched sample show only point defects without line defects. Figure 3.8a shows the HAADF images around the point defect. In the top and bottom part, atoms can clearly be distinguished. However, in the center part, the image is blurred and the spots which indicate the atom location are crumbled. Furthermore, the parallel slabs are crooked to the downward at the defect part (yellow guideline). To analyze the lattice strain induced by point defect cluster, geometric phase analysis (GPA) is used. The lattice strain distribution maps along the *xx* (Figure 3.8b) and *yy* (Figure 3.8c) show the existence of both compressive and tensile strains at the center of the image. The Fast Fourier Transformed pattern on the Figure 3.9a is clearly indexed as the SnSe structure along the [001] zone axis, indicating absence of the secondary phases. Atomic resolution HAAFD and BF STEM images are presented in Figure 3.9b and 3.9c, respectively. In the point defect part, there are a dark spots and the Sn and Se atom is not able to be distinguished. These dark area is attributed to the point defect clusters which is vacancy-rich depleted zone [15]. Consequently, these defect clusters act as a point of phonon dispersion and as-quenched sample shows lower thermal conductivity compared to the pristine SnSe.

Figure 3.10 is an STEM observation image of a sample annealed for 12 hours. The atoms are aligned in the direction perpendicular to the a-axis. However, unlike the SnSe matrix, it can be seen that the position of the atoms in the image is not clear, and the difference in contrast between atoms is not large. It can be seen from the FFT image that the crystallinity is not good because the peak for the corresponding part

does not appear correctly. Also, as shown in Figure 3.10b, it can be thought that it is an intermediate step of the process of transition to another phase by arranging atoms in a curved form without being regularly arranged in the changing part. Through the EDS analysis, it can be confirmed that the corresponding part has a relatively low Sn content and a high In content compared to the SnSe matrix part (Figure 3.11).

Figure 3.13 shows the STEM images and analysis of the sample with 48 hours annealing. In the Figure 3.13a, there are many lines along the same horizon direction with several microns. Furthermore, some defect clusters are arranged in the same direction with the band. It is intermediate state while the defect clusters form the band. In the high-magnification image focused the band, another layered structure phases are formed. Band grow along the a-axis of the SnSe structure and consist of 5-layer width and the width is around 5nm. Figure 3.13c and d shows the phase change point from *Pnma* orthorhombic structure to layered structure. The layers below the change point are crooked, in contrast with the change completed zone (Figure 3.13b). Figure 3.13e, f, g and h shows the band STEM images containing change point, inverse FFT, lattice strain distribution maps along the *xx* and *yy*, respectively. In the band, there are many dislocations and high degree of strain over the 15% along both *xx* direction and *yy* direction is applied due to the formation of other phases.

Here, it is necessary to provide a detailed structural analysis for the secondary phases between the slabs of SnSe matrix. Figure 3.14a shows the atomic resolution

STEM images focused the boundary between SnSe phase and second phase. The new phase is layer structure and each layer consist of 5 atoms along the out-of-layer direction. The light atom and heavy atom are alternatively arrayed. As a result of superimposing the SnSe structure on the matrix area and In_2Se_3 on the band area in Figure 1, it can be confirmed that they match with the same periodicity. Figure 3.14b represents a [001] zone axis FFT pattern, showing obvious additional spots marked with red circles besides the fundamental Bragg peaks from the SnSe matrix. These additional spots are actually from the secondary phases forming band. In the Figure 3.14c, elements mapping results shows that band area is In-rich and Sn-poor zone compared to the SnSe matrix. EDS mapping in STEM observation and EPMA analysis confirm that indium is much distributed in the band but is uniformly distributed in the SnSe structure matrix (Figures 3.15 and 3.16). In the In-rich zone, Sn is also located the same cation position with Indium (Figure 3.17). Se is relatively homogeneously distributed. Taken together, it can be concluded that the precipitated phase forming the band is In_2Se_3 structure.

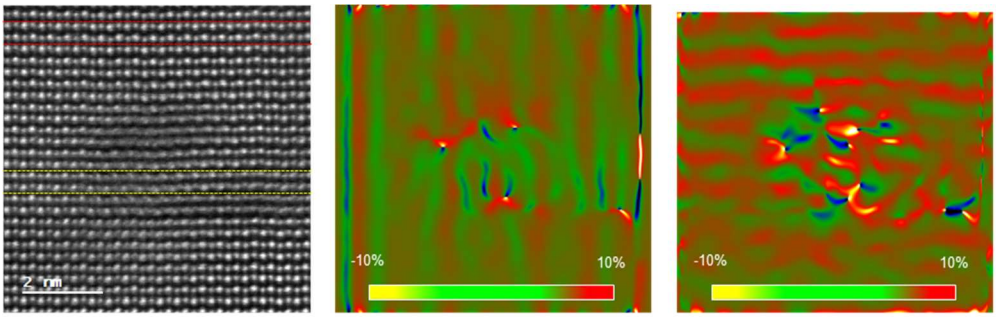

Figure 3.8. a) Cs-corrected scanning transmission electron microscope image focusing vacancy cluster of as-quenched $Sn_{0.97}In_{0.01}Se$ sample, the corresponding strain mapping images along the (b) *xx* direction and (c) *yy* direction.

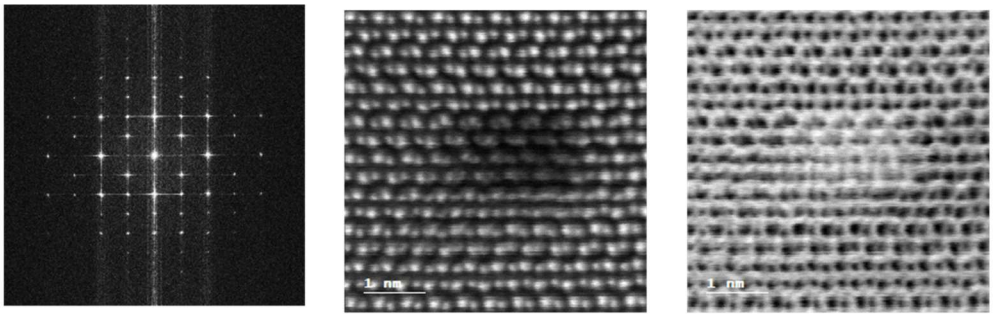

Figure 3.9. (a)FFT images the corresponding Figure 3.8 images. STEM images of vacancy cluster at atomic magnification observed in (b)HAADF mode and (c)BF mode.

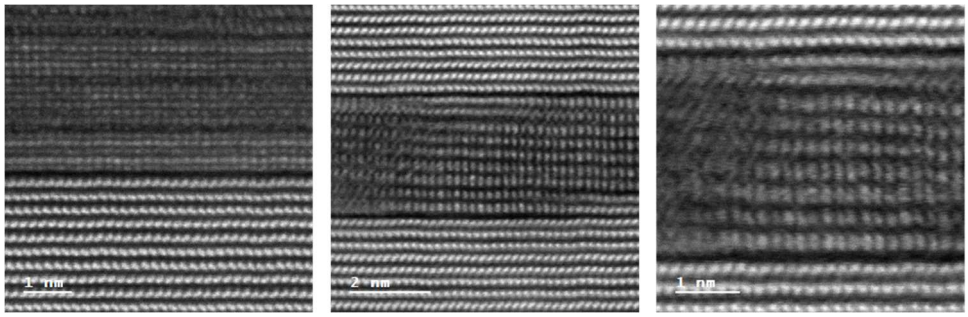

Figure 3.10. Cs-STEM image of $Sn_{0.97}In_{0.01}Se$ sample annealed for 12 hours. a) Image of the segment where the boundary between the SnSe matrix and the new phase. b) In the intermediate stage of transition, the boundary image of the new phase and the SnSe matrix and (c) the enlarged image of the new phase.

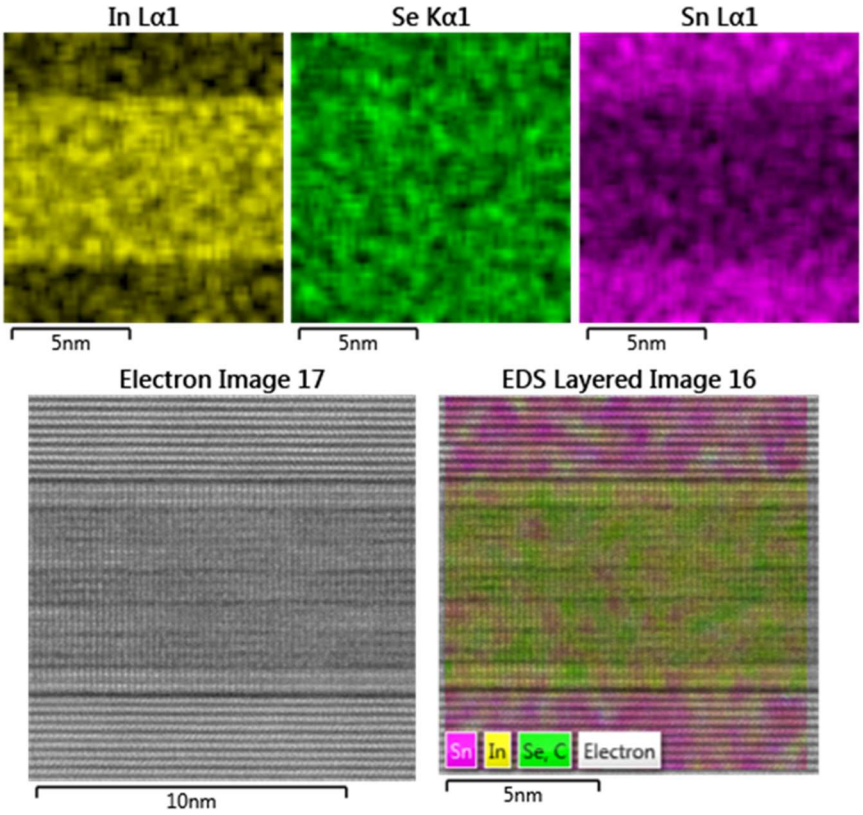

Figure 3.11. Quantitative elemental mapping images taken at heterostructure for 12 hours annealed $Sn_{0.97}In_{0.01}Se$ sample.

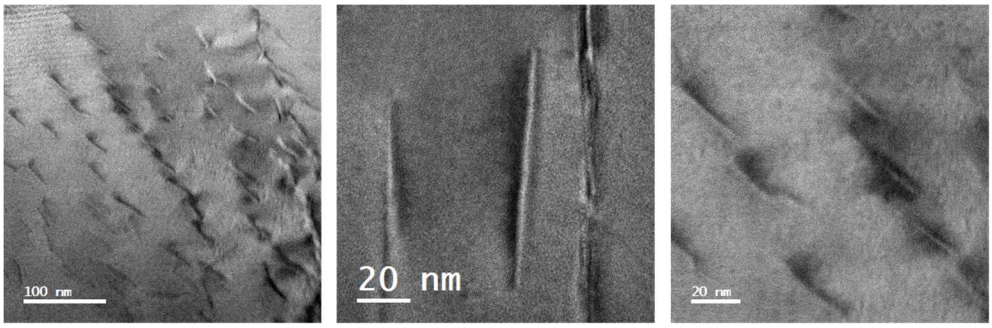

Figure 3.12. Typical low-magnification Cs-STEM image of $Sn_{0.97}In_{0.01}Se$ sample annealed for 12 hours. Vacancy gathered and connected by lines of tens of nanometers in length, and showed a certain direction.

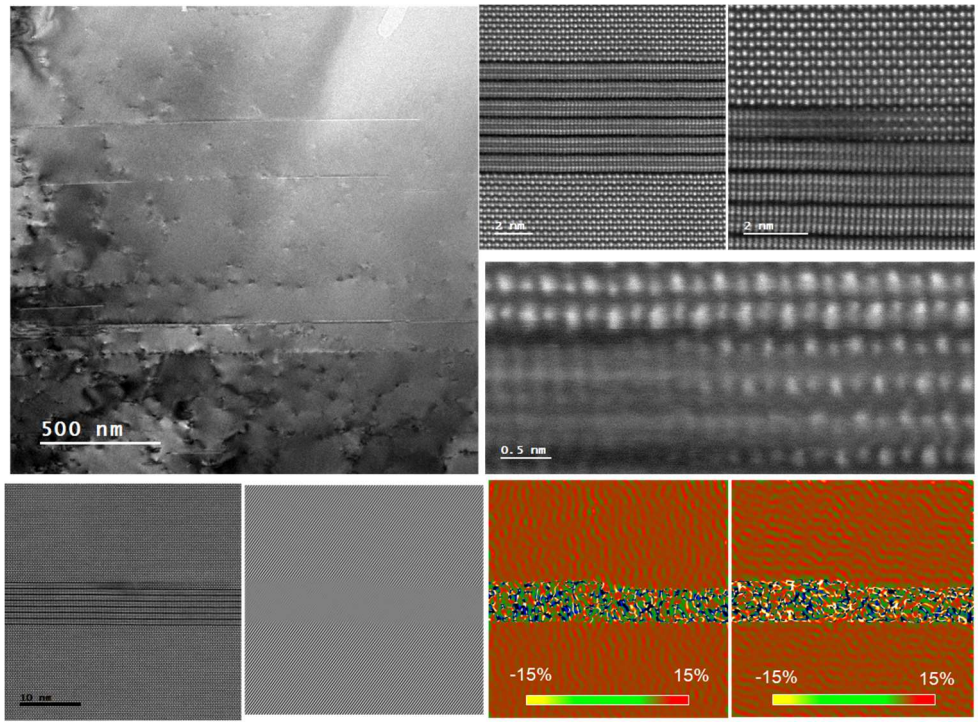

Figure 3.13. Cs-STEM image of $Sn_{0.97}In_{0.01}Se$ sample annealed for 48 hours. a) Low magnification image showing several micro-length bands and aligned vacancy clusters. b) The boundary image where the phase separation of the SnSe and the band is completed. c) The boundary image showing the phase separation points and (d) the enlarged image. e) Boundary image including phase transition point, (f) corresponding inverse FFT image of the part, and strain mapping image along (g) the *xx* direction and (h) *yy* direction.

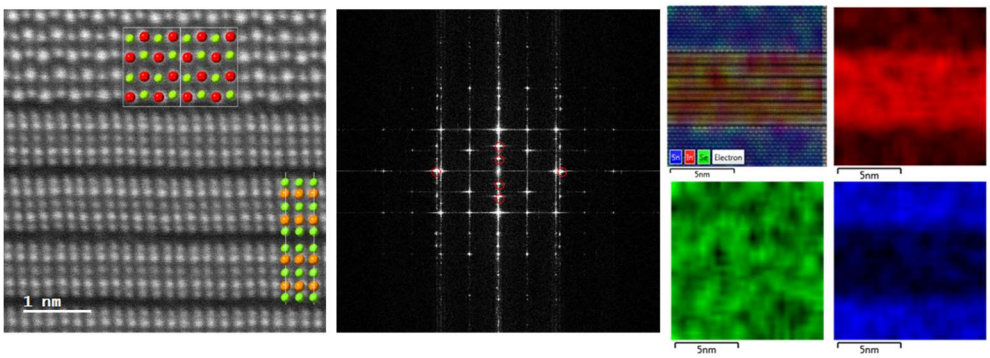

Figure 3.14. a) atomic resolution Cs-STEM image of boundary on SnSe matrix and In_2Se_3 phase and (b) corresponding FFT images. (c) Elemental mapping by STEM-EDS scanned on the entire area of heterostructure. It is created by combining EDS signals directly recorded from (d) In, (e) Se, and (f) Sn atoms, respectively.

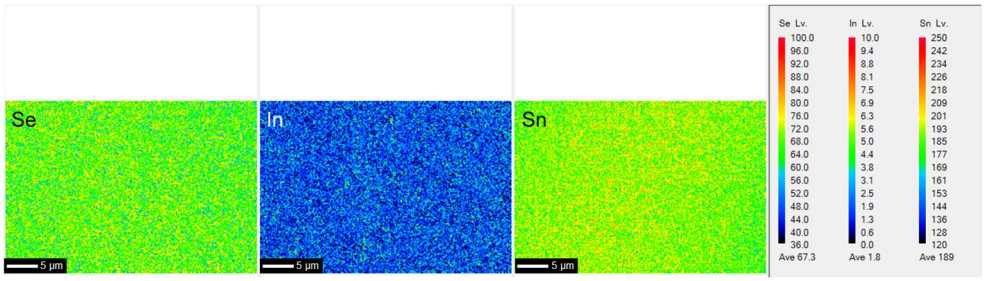

Figure 3.15. EPMA elemental mapping images of $Sn_{0.97}In_{0.01}Se$. At this resolution, no heterostructure of nano-nm thickness was observed.

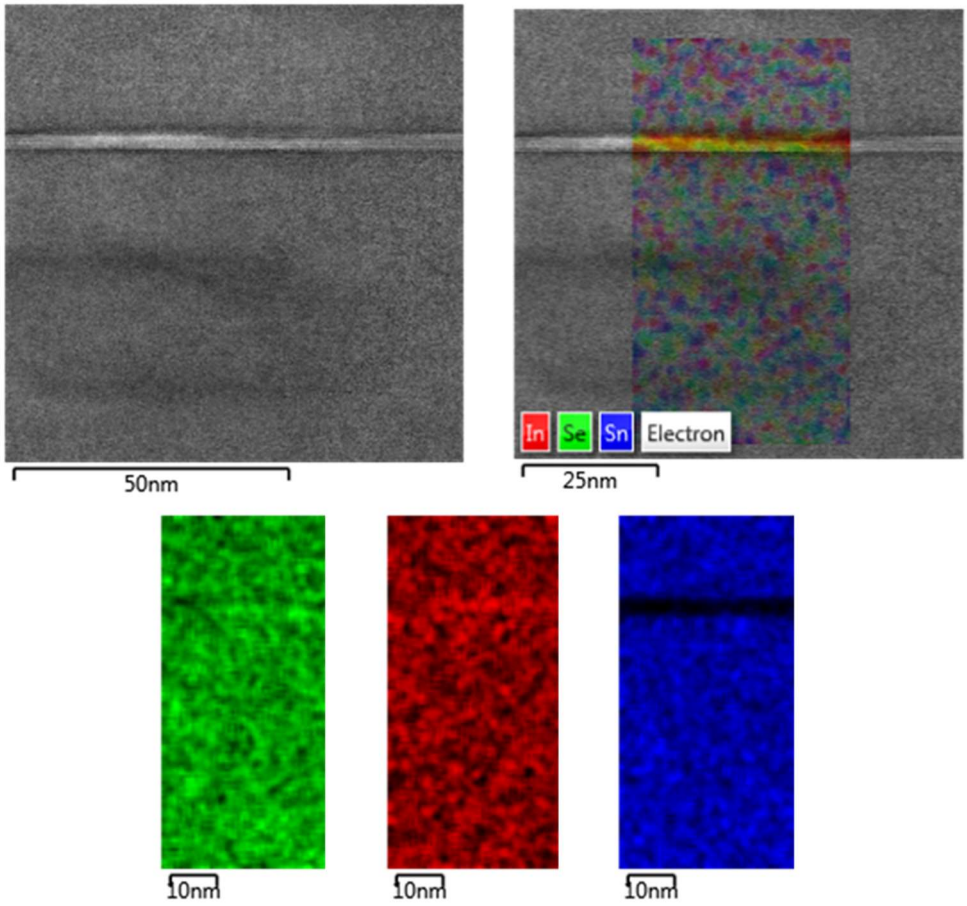

Figure 3.16. Typical Cs-STEM image and quantitative elemental analysis by STEM-EDS for the heterostructure area of $Sn_{0.97}In_{0.01}Se$.

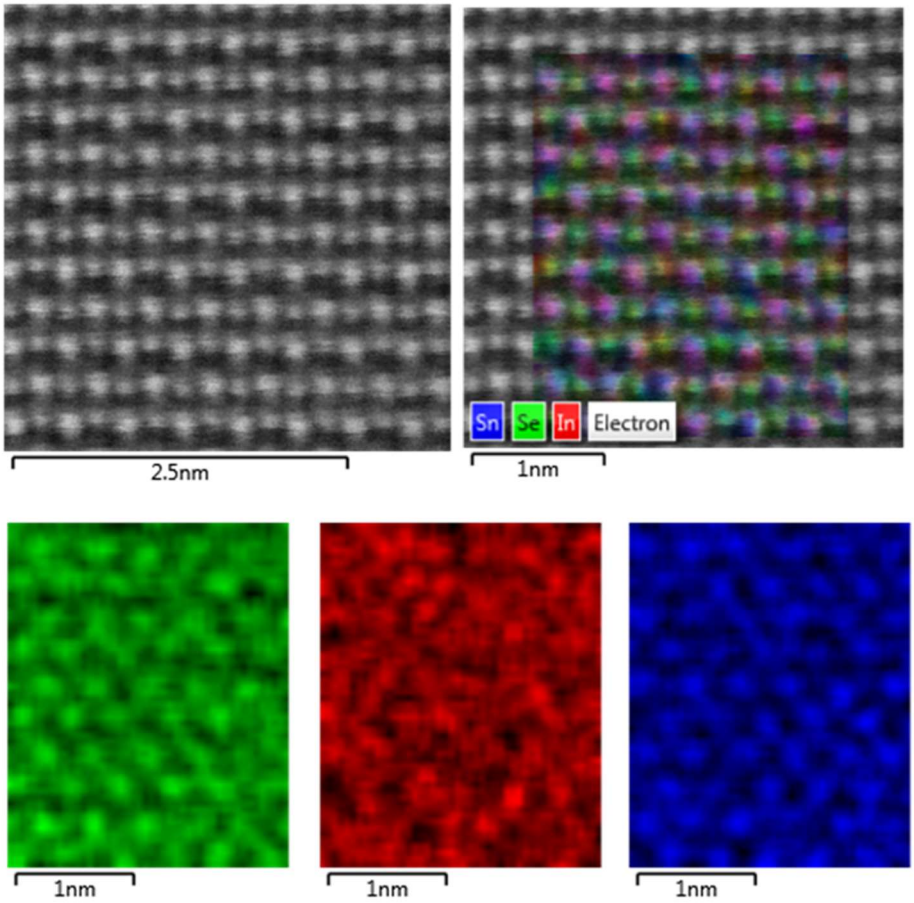

Figure 3.17. Atomic-resolution Cs-STEM image and quantitative elemental analysis by STEM-EDS for the matrix of $Sn_{0.97}In_{0.01}Se$.

Our HAADF-STEM and STEM-EDS results suggest the formation mechanism of second-phase band in SnSe. In the quenched sample, vacancies form the defect cluster over the samples. During the annealing, the heat energy is applied to sample and defect cluster start to diffuse. The defect clusters are arranged in a specific direction (Figures 3.6b and 3.6c). We observed that the more defect cluster accumulation according the annealing time, the longer dislocation is formed by climb process, confirming the mechanism of vacancy-driven dislocations. Finally, they form the In_2Se_3-structure band with several nanometers. It must be thermodynamically favorable for In^{3+} to pair with vacancies for reducing charge imbalance and lattice strains in the $Sn^{2+}Se^{2-}$ lattice. In^{3+} and Sn^{2+} also show the significantly different preference for coordination geometry. Accordingly, being located in the band could be energetically favorable to Indium atoms. Further, the In_2Se_3 phase is a composition with less cation considering only the number of atom. It can be more energetically stable to gather the defect clusters together to form a cation-poor phases than the defect clusters are randomly distributed in the SnSe matrix. In previous research which study in-grain dislocation and climb process in PbTe or PbSe, the dislocation is randomly propagated and connected like a net, resulting from isotropic structure of the matrix. However, in the SnSe structure, *Pnma* orthorhombic structure which is anisotropic, the band is formed between the slabs of the SnSe. It requires larger energy to break the in-slab short Sn-Se bonding than the slab-slab long Sn-Se bonding. Consequently, it is thermodynamically

favorable for the band to be located between the slabs. To support this proposed mechanism, $Sn_{0.93}In_{0.01}Se$ sample, which contains higher contents of vacancy is prepared by the same means. In the STEM analysis, the $SnSe_2$ structure band is observed and the number of the band is similar to the $Sn_{0.97}In_{0.01}Se$ (Figure 3.18). However, it consists of 10 layers with 10 nm thickness. When quenching the sample, it contains much more defect clusters. Therefore, the band can be formed much easily and thickly during annealing process.

Further, to confirm the cause of band formation, $Sn_{0.98}Se$, which is a composition containing only vacancy and not indium, was prepared. Synthesis proceeded in the same way and annealing time proceeded for 48 hours. As a result of observation through STEM, it was confirmed that 'band' was formed between slabs of SnSe (Figure 3.19). However, the difference from the sample containing indium is that the In_2Se_3 phase is not formed and the $SnSe_2$ phase is formed. As shown in the figure, the band is composed of a layered structure, and each layer is composed of three atoms in the thickness direction, and each atom is not distinguishable in the length direction. Also, peak information of a specific phase could not be found through FFT analysis. It can be seen that the heavy Sn atom is located in the middle through the contrast in the thickness direction, and light Se is located up and down, and the intensity analysis shows that it has the same interlayer distance as the distance between Sn in the $SnSe_2$ structure. The reason for not distinguishing the atoms in the longitudinal direction is that the $SnSe_2$ phase in the zone-axis direction of the SnSe

matrix is not oriented in a crystal direction having a specific integer index. In Figure S, the possible arrangement of atoms for the STEM image is inserted. The reason for the formation of the $SnSe_2$ phase is that when sufficient energy is applied to the vacancy, such as a sample indium is introduced, it is more energetically stable to form the $SnSe_2$ phase along the direction in which it is easy to grow than evenly distributed in the SnSe matrix. In addition, another form of $SnSe_2$ was also observed at the end of the band, and has a structure oriented in the direction of about 60 degrees to the b-axis direction(Figure 3.20).

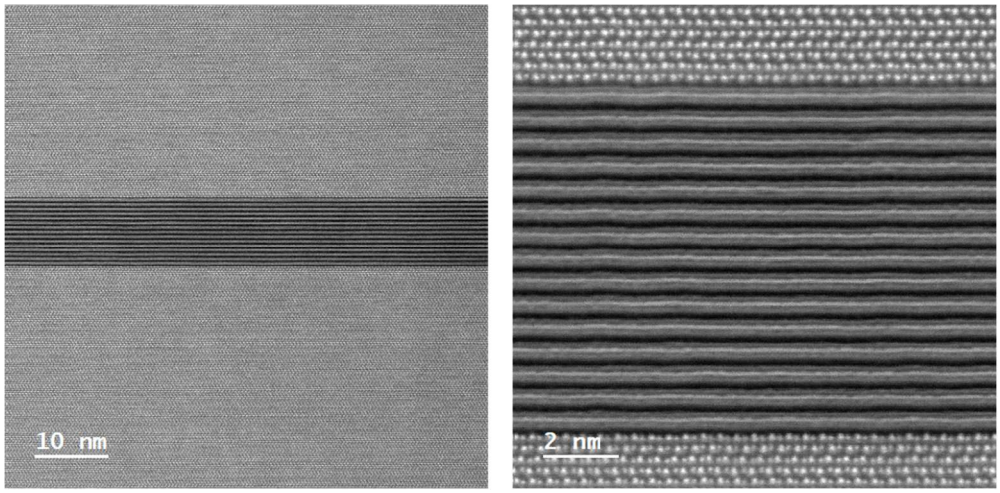

Figure 3.18. Typical dark field (DF) Cs-STEM image of $Sn_{0.93}In_{0.01}Se$. A thick microstructure composed of 15 heterostructure layers is formed.

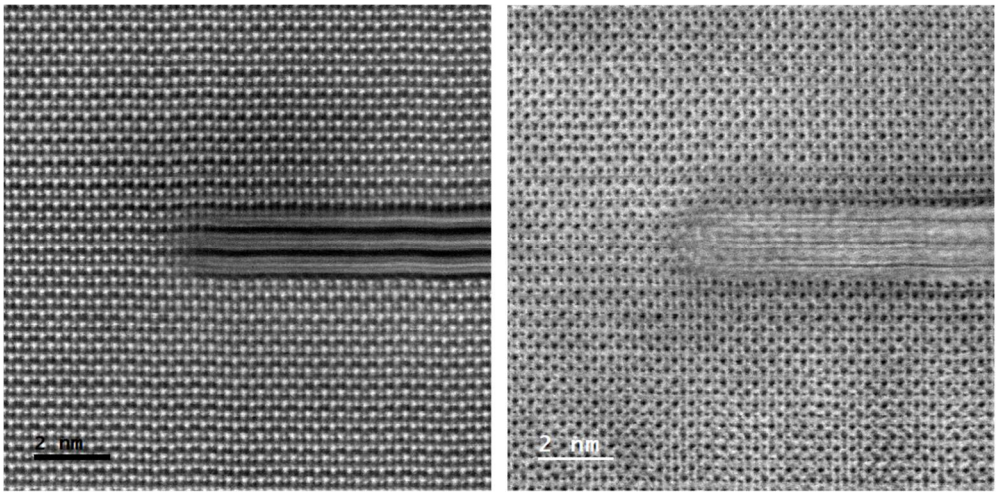

Figure. 3.19. Cs-STEM image of the segment where the boundary between the SnSe matrix and the heterostructure for $Sn_{0.98}Se$. (a) HAADF mode and (b) BF mode.

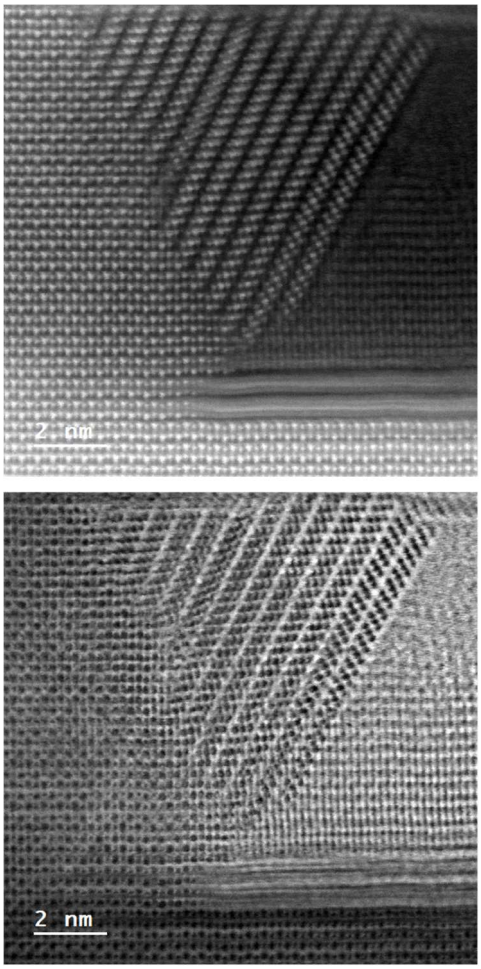

Figure 3.20. Cs-STEM image of the twisted area where the boundary between the SnSe matrix and the heterostructure for $Sn_{0.98}Se$. (a) HAADF mode and (b) BF mode.

Thermoelectric properties

The effect of the content of vacancies on thermoelectric properties was investigated and the results are described in detail in Figure 3.2. From that results, the sample of $Na_{0.01}(Sn_{0.97}In_{0.01})_{0.99}Se$ exhibits the lowest thermal conductivity and the highest thermoelectric performance. The annealing time was set as a variable and the experimental group was constructed according to the annealing time (as-quenched, 48 hours, 96 hours annealed sample). The thermoelectric properties of undoped and 1% Na-doped SnSe were also plotted in the Figure 3.21 as a control for comparison. Unless otherwise noted, all measurements are properties in a direction parallel to the press direction of SPS.

Figure 3.21 shows the electrical conductivity of the samples. The sample undergone 48 hours annealing have higher electrical conductivity than other samples over the entire temperature range. Note that sudden increase of electrical conductivity at more than 723 K is due to the phase transition of SnSe from *Pnma* to *Cmcm* structure. The sample annealed for 48 hours shows 13.69 64 S/cm at room temperature and reaches a maximum of 64 S/cm at 800 K, which is about 1.5 and 2 times higher than that of quenched sample and pristine SnSe, respectively. The carrier concentration of all $Na_{0.01}(Sn_{0.97}In_{0.01})_{0.99}Se$ samples was almost same as ~9×10^{18} cm^{-3} at 300 K (Figure 3.22). the 48 hours annealed sample shows the highest carrier mobility of 11 cm^2/Vs among the samples. As a result of high temperature Hall effect measurement from 300K to 773K, the as-quenched sample and the sample annealed for 48 hours showed

a constant carrier concentration up to 700 K, and tended to decrease slightly above 700 K, resulting from the scattering between major carriers of high concentration. Although there was no significant difference in carrier concentration, the samples annealed for 48 hours showed higher mobility than the as-quenched sample over the entire temperature range. This shows that it is more advantageous for the charge carrier to move through the band formed matrix than through the matrix in which the vacancy clusters are distributed. Additional annealing can lead to the formation of thicker bands, resulting in more scattering of charge carriers.

The all $Na_{0.01}(Sn_{0.97}In_{0.01})_{0.99}Se$ samples show p-type character and a lower Seebeck coeffieicnt than the pristine SnSe sample, and this is consistent with a lower hole carrier concentration (Figure 3.21b). The Seebeck coefficients of all $Na_{0.01}(Sn_{0.97}In_{0.01})_{0.99}Se$ show almost same values over the entire temperature which monotonously increase to reach ~+400 $\mu V\ K^{-1}$at 673K and then decline to ~+305 $\mu V\ K^{-1}$ at 800K

As shown in the Pisarenko plot which is relation between Seebeck coefficient and carrier concentration, $Na_{0.01}(Sn_{0.97}In_{0.01})_{0.99}Se$ samples are well fitted by a DOS effective mass of 1.0 m_e. The 1% Na-doped SnSe and undoped SnSe have slightly lower value of 0.8 m_e and 0.47 m_e, respectively (Figure 3.23). this result is consistence with the band calculation results. The introduction of indium leads to a change in the valence band and thereby a higher effective mass compared to undoped and 1% Na-doped SnSe.

Because of the improved σ in the entire temperature, the sample annealed 48 hours shows the highest power factor for 5.81 μW $cm^{-1}K^{-2}$ at 800 K while that of pristine SnSe and $Na_{0.01}Sn_{0.99}Se$ is 3.28 μW $cm^{-1}K^{-2}$ and 4.31 μW $cm^{-1}K^{-2}$, respectively.

Figures 3.21d and 3.21e show the temperature-dependent total and lattice thermal conductivity for undoped, 1% Na-doped SnSe and $Na_{0.01}(Sn_{0.97}In_{0.01})_{0.99}Se$ (quenched, 48 hours, 96 hours annealed) samples. As-quenched sample exhibits lower total and lattice thermal conductivity over the entire temperature range compared to undoped and 1% Na-doped SnSe. Further, in Figure 3.2, the $Na_{0.01}(Sn_{0.99}In_{0.01})_{0.99}Se$ sample which does not contain the artificial vacancy shows higher thermal conductivity than $Na_{0.01}(Sn_{0.97}In_{0.01})_{0.99}Se$ from room temperature to 800 K. Formation of vacancy clusters make the lattice distortion and strain to be applied, thus causing phonon scattering.

The annealed samples exhibit lower lattice thermal conductivity than as-quenched sample over the entire temperature range, demonstrating that formation of dislocation can reduce thermal conductivity much efficiently than distribution of the vacancy cluster over the matrix. The 48 hours annealed sample shows the higher lattice thermal conductivity than the 96 hours annealed sample up to 723 K. Above 773 K, 48 hours annealed sample shows lower lattice thermal conductivity than 96 hours annealed sample. The 48 hours annealed sample reaches a minimum lattice thermal conductivity of 0.16 W $m^{-1}K^{-1}$ at 800 K.

This value is about half of and is also lower than the that of undoped and Na-doped

SnSe single crystals along the a-axis. This observation can be ascribed to vacancy clusters that remain in the matrix of 48 hours annealed sample as observed in the STEM. The additional annealing for 48 hours causes the remaining clusters to form the band, which further lowers the thermal conductivity.

The 48 hours annealed sample exhibits the highest figure of merit, ZT of ~2.00 at 773 K among the sample series, which is attributed simultaneously from enhanced power factor and remarkably lowered κ_{tot} and κ_{lat}. These value is about two times higher that of polycrystalline 1% Na-doped SnSe and three about times that of polycrystalline undoped SnSe.

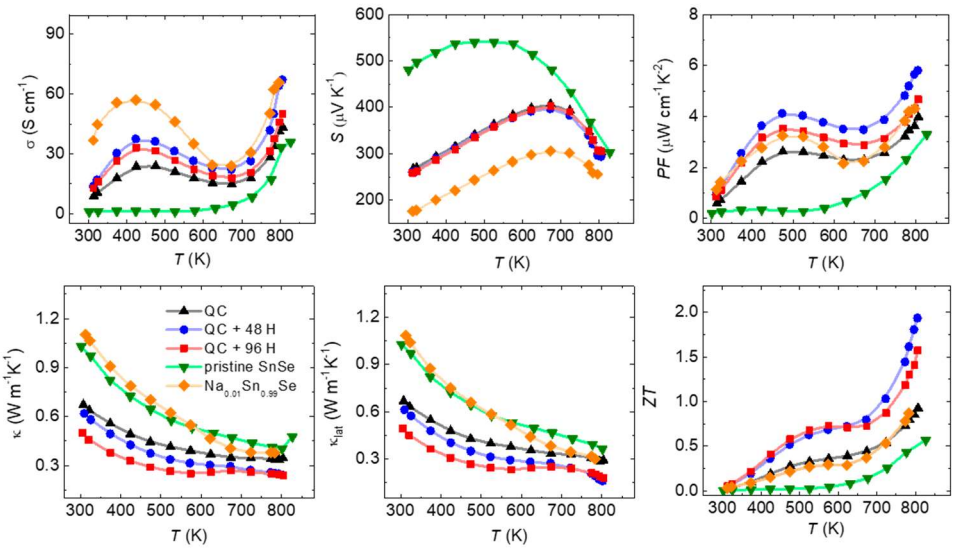

Figure 3.21. Temperature-dependent (a) electrical conductivity, (b) Seebeck coefficient, (c) power factor, (d) total thermal conductivity, (e) lattice thermal conductivity, and (f) figure of merit, ZT for as-quenched, 48 hours annealed, 96 hours annealed $Na_{0.01}(Sn_{0.97}In_{0.01})_{0.99}Se$, pristine SnSe and $Na_{0.01}Sn_{0.99}Se$.

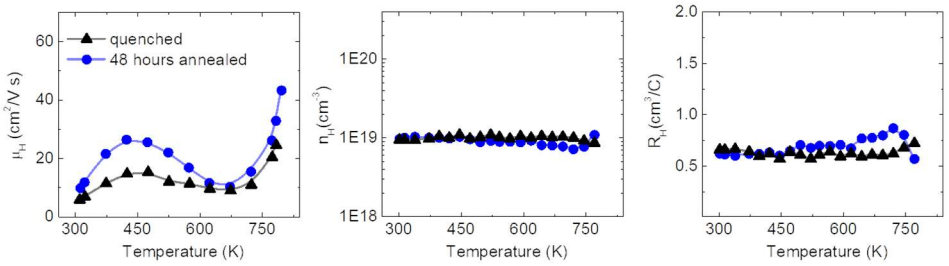

Figure 3.22. Temperature-dependent Hall measurement results for quenched and 48 hours annealed $Na_{0.01}(Sn_{0.97}In_{0.01})_{0.99}Se$. (a) Hall mobility, (b) carrier concentration, (c) Hall coefficient.

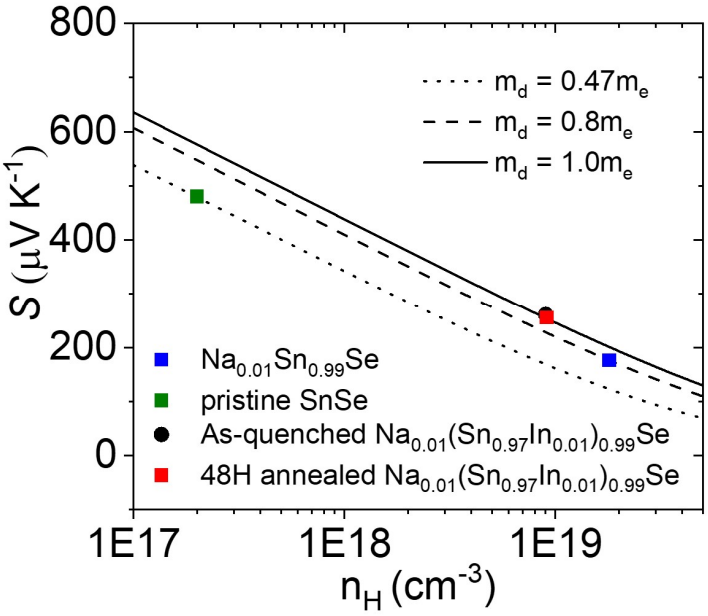

Figure 3.23. Seebeck coefficient as a function of hole concentration (n_H) at room temperature. We calculated the Pisarenko relation between S and n_H using a single parabolic band (SPB) and a multivalley band (MVB) models for SnSe, and compared the results with the experimental S values at 300 K for as-quenched and 48 hours annealed $Na_{0.01}(Sn_{0.97}In_{0.01})_{0.99}Se$.

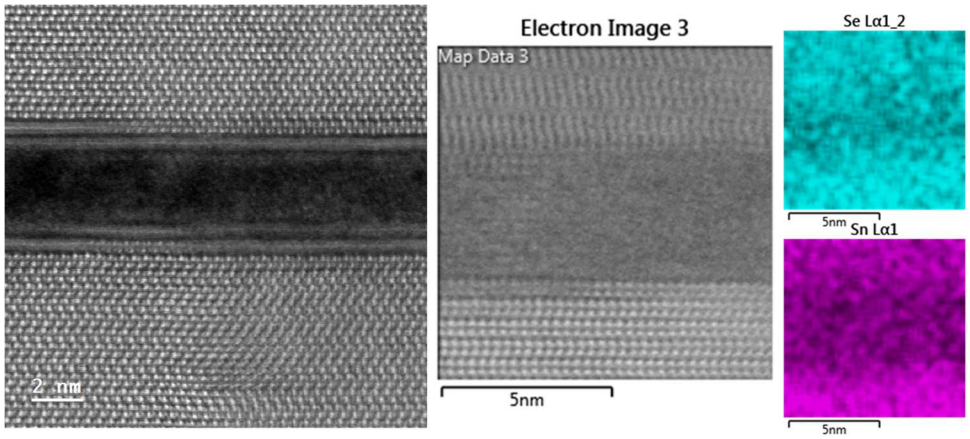

Figure 3.24. Typical Cs-STEM image and quantitative elemental analysis by STEM-EDS for the segment between matrix and heterostructure of $Sn_{0.98}Se$. Amorphous phase is formed between the slabs.

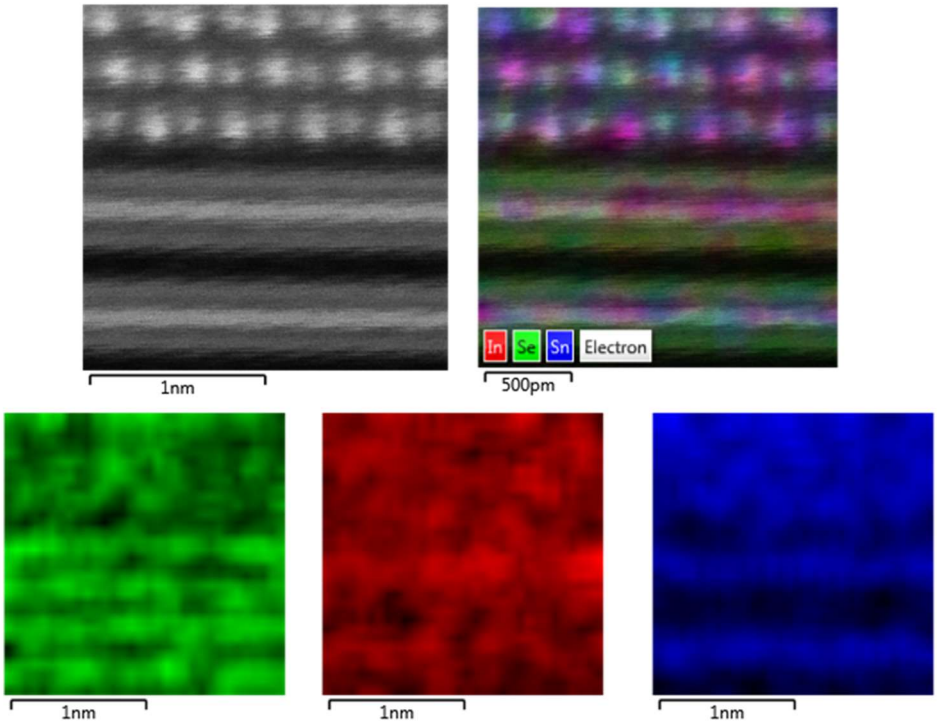

Figure 3.25. Atomic-resolution Cs-STEM image and quantitative elemental analysis by STEM-EDS for the segment between matrix and heterostructure of $Sn_{0.98}Se$.

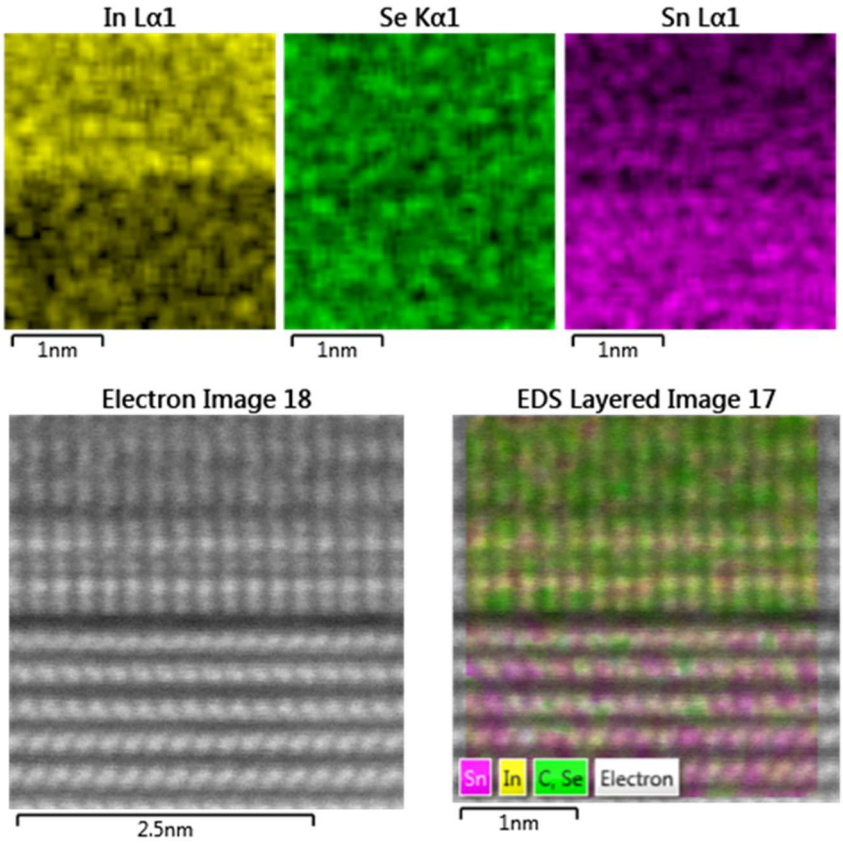

Figure 3.26. Atomic-resolution Cs-STEM image and quantitative elemental analysis by STEM-EDS for the segment between matrix and heterostructure of 12 hours annealed $Na_{0.01}(Sn_{0.97}In_{0.01})_{0.99}Se$.

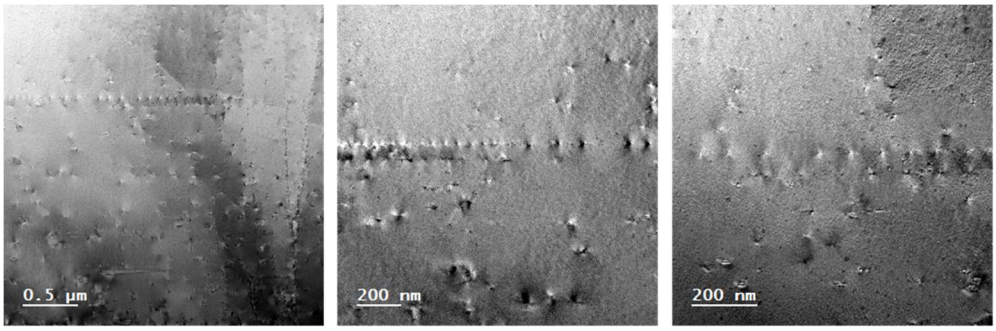

Figure 3.27. Typical Cs-STEM images of as-quenched $Sn_{0.97}In_{0.01}Se$. Vacancy clusters are aligned along the specific direction.

3.4 Conclusion

As a result, the microstructure was observed by annealing SnSe containing 2% of vacancies and 1% of indium above the phase transition temperature, thereby suggesting a band formation mechanism. It was found that the vacancies gathered between slabs to form a layer, and indium plays a role in forming a new crystalline phase. the bands having the thickness of several nanometers and the length of several micrometers in the energetically stable direction are different from the previous defects grow and dislocation formation along the random direction in the conventional isotropic crystal structure. The formation of vacancy clusters causes strain of the lattice, and the thermal conductivity becomes lower as the process of forming bands. In the band-formed samples, the scattering of phonons was maximized, resulting in lower thermal conductivity than single crystal SnSe. Indium-containing samples also showed an improved Seebeck coefficient, which was revealed by theoretical calculations as a result of band structure changes. The improved thermal conductivity, Seebeck coefficient and lower thermal conductivity combined resulted in a high thermal performance of ~2.0. We have found a mechanism by which dislocation grows in a material with anisotropic crystal structure, which allows us to control the thermal conductivity of the material. Our results enable us to independently control the thermal conduction properties of bulk materials and can be applied to various fields based on thermal conduction, including thermoelectrics.

3.5 References

1. Tan, G.; Zhao, L.-D.; Kanatzidis, M. G., Rationally Designing High-Performance Bulk Thermoelectric Materials. *Chemical Reviews* **2016,** *116* (19), 12123-12149.

2. He, J.; Tritt, T. M., Advances in thermoelectric materials research: Looking back and moving forward. *Science* **2017,** *357* (6358), eaak9997.

3. Jood, P.; Ohta, M.; Yamamoto, A.; Kanatzidis, M. G., Excessively Doped PbTe with Ge-Induced Nanostructures Enables High-Efficiency Thermoelectric Modules. *Joule* **2018,** *2* (7), 1339-1355.

4. Zhao, L.-D.; Lo, S.-H.; Zhang, Y.; Sun, H.; Tan, G.; Uher, C.; Wolverton, C.; Dravid, V. P.; Kanatzidis, M. G., Ultralow thermal conductivity and high thermoelectric figure of merit in SnSe crystals. *Nature* **2014,** *508*, 373.

5. Lee, Y. K.; Ahn, K.; Cha, J.; Zhou, C.; Kim, H. S.; Choi, G.; Chae, S. I.; Park, J.-H.; Cho, S.-P.; Park, S. H.; Sung, Y.-E.; Lee, W. B.; Hyeon, T.; Chung, I., Enhancing p-Type Thermoelectric Performances of Polycrystalline SnSe via Tuning Phase Transition Temperature. *Journal of the American Chemical Society* **2017,** *139* (31), 10887-10896.

6. Zhao, L.-D.; Chang, C.; Tan, G.; Kanatzidis, M. G., SnSe: a remarkable new thermoelectric material. *Energy & Environmental Science* **2016,** *9* (10), 3044-3060.

7. Kanatzidis, M. G., Nanostructured Thermoelectrics: The New Paradigm?

Chemistry of Materials **2010,** *22* (3), 648-659.

8. Biswas, K.; He, J.; Zhang, Q.; Wang, G.; Uher, C.; Dravid, V. P.; Kanatzidis, M. G., Strained endotaxial nanostructures with high thermoelectric figure of merit. *Nature Chemistry* **2011,** *3* (2), 160-166.

9. Biswas, K.; He, J.; Blum, I. D.; Wu, C.-I.; Hogan, T. P.; Seidman, D. N.; Dravid, V. P.; Kanatzidis, M. G., High-performance bulk thermoelectrics with all-scale hierarchical architectures. *Nature* **2012,** *489* (7416), 414-418.

10. Tan, G.; Hao, S.; Cai, S.; Bailey, T. P.; Luo, Z.; Hadar, I.; Uher, C.; Dravid, V. P.; Wolverton, C.; Kanatzidis, M. G., All-Scale Hierarchically Structured p-Type PbSe Alloys with High Thermoelectric Performance Enabled by Improved Band Degeneracy. *Journal of the American Chemical Society* **2019,** *141* (10), 4480-4486.

11. Hodges, J. M.; Hao, S.; Grovogui, J. A.; Zhang, X.; Bailey, T. P.; Li, X.; Gan, Z.; Hu, Y.-Y.; Uher, C.; Dravid, V. P.; Wolverton, C.; Kanatzidis, M. G., Chemical Insights into PbSe–x%HgSe: High Power Factor and Improved Thermoelectric Performance by Alloying with Discordant Atoms. *Journal of the American Chemical Society* **2018,** *140* (51), 18115-18123.

12. Chen, Z.; Ge, B.; Li, W.; Lin, S.; Shen, J.; Chang, Y.; Hanus, R.; Snyder, G. J.; Pei, Y., Vacancy-induced dislocations within grains for high-performance PbSe thermoelectrics. *Nature Communications* **2017,** *8* (1), 13828.

13. Wu, Y.; Chen, Z.; Nan, P.; Xiong, F.; Lin, S.; Zhang, X.; Chen,

Y.; Chen, L.; Ge, B.; Pei, Y., Lattice Strain Advances Thermoelectrics. *Joule* **2019,** *3* (5), 1276-1288.

14. Zhou, C.; Lee, Y. K.; Cha, J.; Yoo, B.; Cho, S.-P.; Hyeon, T.; Chung, I., Defect Engineering for High-Performance n-Type PbSe Thermoelectrics. *Journal of the American Chemical Society* **2018,** *140* (29), 9282-9290.

15. Lin, Y. R.; Chen, L. G.; Hsieh, C. Y.; Chang, M. T.; Fung, K. Y.; Hu, A.; Lo, S. C.; Chen, F. R.; Kai, J. J., Atomic Configuration of Point Defect Clusters in Ion-Irradiated Silicon Carbide. *Scientific Reports* **2017,** *7* (1), 14635.

Chapter 4. Revealing intrinsic charge and thermal transport properties of SnSe - Removal of surface SnO_x by a chemical reduction process.

4.1 Introduction

One remarkable discovery is SnSe that consists of earth crust-abundant and eco-friendly elements. Once this system was ignored for thermoelectric applications because of high electrical resistivity. However, when grown as a single crystal form, pristine p-type SnSe crystals show a ZT of 2.6 at 923 K along the *b* axis(*26*). Br-doped n-type crystals exhibit a ZT of 2.8 at 773 K along the *a* axis(*29*). Such record high ZT values are attributed to intrinsic ultralow lattice thermal conductivity (κ_{lat}) (0.11 W $m^{-1}K^{-1}$) due to strong anharmonic and anisotropic bonding in the structure, rather than application of complex strategies. However, serious debates have arisen on its ultralow κ_{lat}, because most polycrystalline SnSe and its relevant phases were reported to show higher κ_{lat} values than the corresponding single crystals, leading to much lower ZTs than those of the latter. These results are strikingly contrary to the general understanding, given that polycrystals tend to exhibit lower κ_{lat} values than single crystals by virtue of additional phonon scattering at grain boundaries. Two mechanisms were evoked for this unusual observation. First, the exposure to air

could oxidize the surface of SnSe powders, obscuring intrinsically ultralow κ_{lat}. Second, vast off-stoichiometric defects were recently observed in SnSe single crystals with ultralow κ_{lat} by aberration-corrected transmission electron microscope(*30*). They are suggested as the origin of a deviation in κ_{lat} between poly- and single crystals. However, these issues are still controversial. Admittedly, the form of single crystals is unsuitable for mass production and broad applications, because synthesizing them is a time-consuming, labor-intensive, and expensive process. Because of highly anisotropic layered structure, SnSe single crystals are also prone to mechanical cracks. On those accounts, the prime interest in thermoelectrics has been realizing polycrystalline SnSe-based materials with comparable ZT to their single crystals.

Here we report that a combined process of ball mill and reduction efficiently removes tin oxides layers on powders of SnSe-based materials, revealing their intrinsically ultralow κ_{lat} and exceptionally high ZT. First, 1% Na-doped SnSe-5%PbSe powders, namely $Na_{0.01}(Sn_{0.95}Pb_{0.05})_{0.99}Se$, were ball-milled for increasing surface area and consequently maximizing the effect of reduction. Then, they were reduced under 4% H_2/Ar atmosphere at 613 K for 6 hours to clean off oxide residues on the surface and subsequently consolidated by spark plasma sintering (SPS). The resulting dense specimen exhibits the lowest κ_{lat} reported to date for any crystalline materials of 0.11 W $m^{-1}K^{-1}$ and a maximum ZT (ZT_{max}) ~2.5 at 773 K parallel to the press direction of SPS (Fig. 1a). The obtained ZT is more than six-fold larger than

~0.6 of its pristine phase along the same direction. A ball mill process prior to reduction is essential. Without it, ZT moderately increases to ~1.1. A ball process by itself does not improve ZT. The ball milled and reduced (denoted as BR hereafter) sample outperforms p-type undoped SnSe single crystals up to 773 K and shows a comparable ZT_{max} to the latter (Fig. 1b). The achieved ZT_{max} is much higher than ZT_{max} ~2.0 at 773 K of p-type Na-doped SnSe single crystals(*25*). Remarkably, the BR sample also displays a high ZT_{max} ~1.8 at 773 K perpendicular to the press direction.

4.2 Experimental section

Reagents. The following reagents were used as obtained unless note otherwise: Sn chunk (99.999% American Elements, US), Se shot (99.999% 5N Plus, Canada) and Na pieces (99.9%, Sigma-Aldrich, US).

Synthesis. All procedures for synthesis and sample preparations were carried out in an Ar-filled glovebox (99.99 % purity), in which the level of moisture and oxygen is kept at 0 and less than 1 ppm. To eliminate the oxide layer in the Sn surface, Sn chunks were placed to a graphite sheet that was washed by ethanol and heated to 473 K in 2 h, held for 6 h, and cooled to room temperature under a 4% H_2/96% Ar flow at a rate of 200 mL min^{-1}. The morphology of Sn chunk turned from angled-shape to round-shape because reaction temperature is near the melting temperature (~505 K). However, there is no visible change on the surface color and luster. The resulting Sn chunks were loaded into a carbon-coated and evacuated fused-silica tube (~10^{-4} Torr). The tube was heated to 1273 K in 8 h, held for 6 h, and cooled to room temperature. The Sn ingot was obtained by breaking the tube in glovebox. On top and surface of the Sn ingot, there is black, ash-like impurity. To eliminate this impurity, the surface of the ingot was cut by knife. These heating, cooling and cutting the surface procedure was repeated for 3 times (the placing temperature was change to 873 K and 723 K, respectively). After these repeats, there is no black impurity and the surface of Sn ingot shows totally silver-color. For synthesizing $Sn_{0.995}Se$ p-type with *x* mole% Na ingots, an appropriate ratio of Na, Sn and Se reagents was loaded to a

carbon-coated and evacuated fused-silica tube (~10^{-4} Torr). The total weight of reactants was about 13 g. The tube was heated to 1223 K in 8 h, held for 12 h, followed by quenching to ice water. The obtained ingot was annealed at 773 K for 48 h and naturally cooled to room temperature. The product was pulverized by hand grinding. For further chemical reduction with H_2, the powders were heated to 613 K in 2 h, held for 6 h, and cooled to room temperature in 8 h under a 4% H_2/96% Ar flow at a rate of 200 mL min^{-1}.

Compacting powders. Powders were loaded in a BN-coated graphite die in an Ar-filled glovebox and cold-pressed manually. The die was taken out of the glovebox and placed in a spark plasma sintering (SPS) system (SPS-211Lx, Fuji Electronic Industrial Co., Japan) under an Ar flow (99.99% purity). Powder samples in the die were densified at ~ 783 K for 5 min under an axial pressure of 50 MPa in a vacuum of ~ 1.4×10^{-2} Torr using SPS.

Powder X-ray diffraction (XRD). XRD analysis was performed on powder and bulk samples using a SmartLab Rigaku X-ray diffractometer (Cu Kα graphite-monochromatized radiation) operating at 40 kV and 30 mA at room temperature.

Electrical and thermal transport property measurements. The samples after SPS were cut and polished into a rectangular shape with a length of 13 mm and thickness of ~ 2 mm under a N_2 atmosphere (99.99% purity). The electrical conductivity and Seebeck coefficient were measured simultaneously under an Ar atmosphere from

room temperature to 823 K using a Netzsch SBA 458 Nemesis system. Temperature-dependent Hall coefficients (R_H) of the samples were obtained on a Lake Shore HMS8407 Hall effect measurement system in a magnetic field of 1.5 T. The hole carrier concentration (n_H) and hole mobility (μ_H) were calculated by the relations, $n_H = 1/(e \cdot R_H)$ and $\mu_H = R_H \cdot \sigma$, respectively. A Netzsch LFA 457 MicroFlash instrument was employed to take the thermal diffusivity of the samples coated with graphite. The samples are disk shape with a diameter of 8 mm and thickness of 1 to 2 mm. The thermal conductivity was calculated from $\kappa_{tot} = D \cdot C_p \cdot \rho$, where D is the thermal diffusivity, C_p is the heat capacity, and ρ is the mass density of the specimens. The temperature-dependent C_p values were derived from previous study (single crystal Na doped SnSe, SCIENCE). The ρ values used were obtained by their geometrical dimensions and masses. The total thermal conductivity κ_{tot} is the sum of the lattice (κ_{lat}) and electronic thermal (κ_{ele}) conductivities. κ_{ele} is proportional to the electrical conductivity (σ) according to the Wiedemann−Franz law ($\kappa_{ele} = L \cdot \sigma \cdot T$), where L is the temperature-dependent Lorenz number and T is the absolute temperature. An L value with respect to temperature were obtained from previous studies. The κ_{lat} value was estimated by subtracting the κ_{ele} value from the κ_{tot} value: $\kappa_{lat} = \kappa_{tot} - \kappa_{ele}$.

4.3 Results and discussion

A sample of composition SnSe-5%PbSe doped p-type with 1 mole% Na was synthesized in ingot form by melting constituent elements, pulverized, and sieved to

less than 45μm. The obtained pristine powders were either ball milled (denoted as BM) or reduced at 613 K for 6 hours (RD). They were also ball milled and subsequently reduced (BR). These four kinds of samples were consolidated into dense pellets by spark plasma sintering (SPS). The relative density to a theoretical value of pristine, BM, RD, and BR SPS specimens is typically 96.5, 96.8, 93.5, 94.1 % (Table 4.1). All procedures for sample preparation including grinding, sieving, ball-milling of powders as well as opening reaction tubes were strictly performed in an argon atmosphere (99.99% purity). All synthesized members adopt SnSe crystal structure with no impurity according to their powder X-ray diffraction (PXRD) patterns (Fig. 4.2). The BM sample features a broad peak width due to the nanoscale (20 – 50 nm) and partially amorphized powders by a ball mill process. High crystallinity is recovered in the BR sample by a reduction process at 613 K.

It is important to note that all materials of chalcogenides must be prone to oxidation when exposed to air, and they have a different extent of sensitivity to oxidation. Tin (Sn) chalcogenide materials have to be dealt with a special care. It is well known that Sn can resist on chemical corrosion and is not readily oxidized. However, the reason is the presence of its oxide thin film on the surface that prohibits further oxidation. On that account, powders of tin chalcogenide materials can be coated with oxide thin film either inherently originating from starting reagents or an exposure to air. Furthermore, Sn can adopt both divalent and slightly more stable tetravalent formal oxidation states. They always coexist in Sn-containing materials

of chalcogenides, oxides, and halides, giving unavoidable vacancies in cationic lattices in their structures. This fact is a major challenge in improving optoelectronic performances of Sn-based halide perovskite compounds. As a result, restricting the evolution of SnO, SnO_2, and $SnSe_2$ should be a key to unveiling inherent thermoelectric properties of SnSe-based materials. Indeed, tetragonal SnO_2 shows total thermal conductivity (κ_{tot}) of ~98 and ~55 W m^{-1} K^{-1} along the *c* and *a* axes, respectively, at room temperature[30]. SnO has κ_{tot} of ~2 W m^{-1} K^{-1} at room temperature, and it readily transforms to SnO_2 at high temperature. As a consequence, their presence even at the very low level can damage TE performance of SnSe-based materials significantly by raising κ_{tot} hugely and depressing electrical conductivity due to electron scattering at the interface. Because as-grown SnO_2 typically shows a considerable degree of unintentional n-type conductivity, its presence is critical to electrical transport property of intrinsic p-type semiconductor SnSe[31].

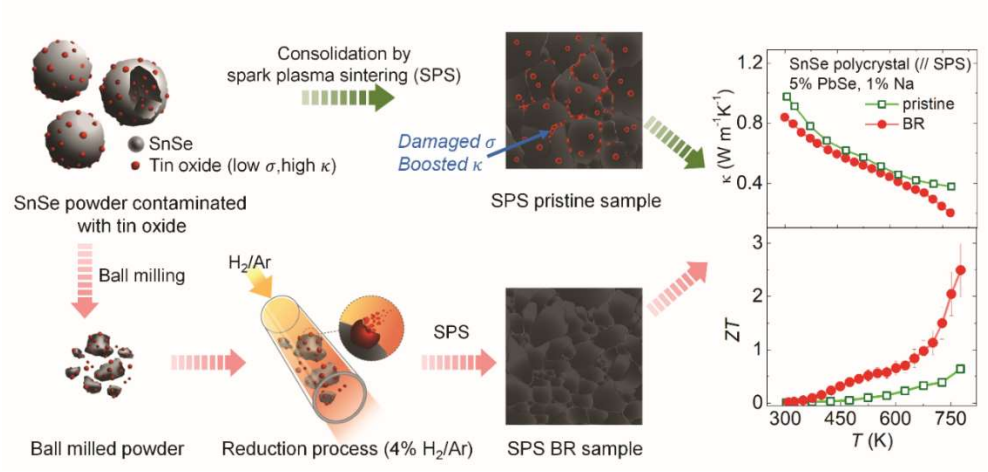

Figure 4.1 A schematic illustration of the oxide removal process and its effect on thermoelectric properties.

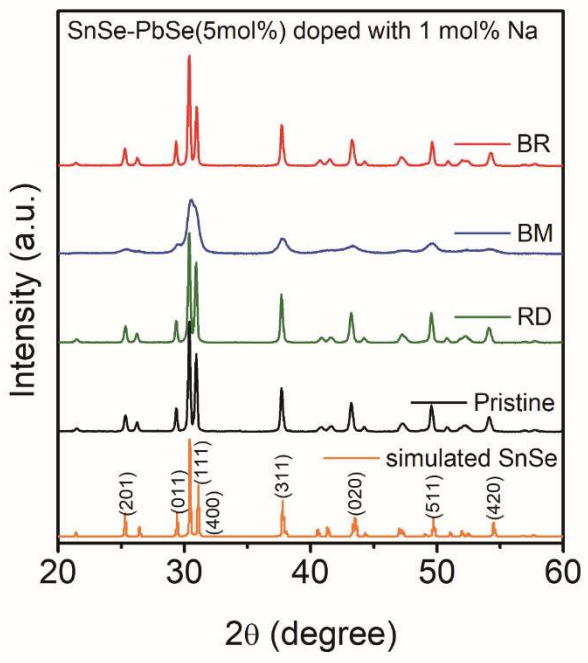

Figure 4.2 Powder X-ray diffraction patterns of pristine, BM, RD, and BR samples in comparison with that of the theoretical calculation for SnSe (The International Centre for Diffraction Data (ICDD) PDF 01-075-6133). SPS processed ingots were ground to fine powders for the measurement.

Table 4.1 The mass densities and relative densities to the theoretical values for the pristine, BM, RD, and BR samples.

Nominal compositions and conditions	Density (g/cm^3)	Relative density (%)
pristine SnSe-PbSe(5 mol%) doped with 1 mol% Na	6.07	96.5
Reduced SnSe-PbSe(5 mol%) doped with 1 mol% Na	6.09	96.8
Ball-mill SnSe-PbSe(5 mol%) doped with 1 mol% Na	5.88	93.5
Ball-mill and reduced SnSe-PbSe(5 mol%) doped with 1 mol% Na	5.92	94.1

We first investigated the SPS-processed pristine pellet employing spherical aberration-corrected scanning transmission electron microscope (Cs-STEM) equipped with an energy dispersive spectroscopy (EDS) detector. Its low-magnification bright-field (BF) STEM image shows brighter nanoscale precipitates with a size in ~20 nm (Fig. 4.3). This indicates the presence of chemical species that has smaller molecular mass than the surrounding matrix. Elemental mappings scanned on the corresponding area by STEM-EDS reveals that those precipitates are devoid of Se atoms and richer in O atoms while Sn atoms are homogeneously distributed through them and the matrix. Surprisingly, nanoscale particles of tin oxides are present in pristine samples that are strictly prepared in an Ar atmosphere.

Afterward, we ball milled pristine powders to better examine oxide contaminants and to maximally remove them by reduction. A size of the powders generally ranges from ~20 to 50 nm. Typical low-magnification STEM image for the BM sample shows randomly oriented nanoscale grains with amorphous regions in part (Fig. 4.4a). Fast Fourier transform (FFT) images taken on the rectangles in Fig. 4.4a also give diffuse features. Representative dark-field (DF) STEM image of the BM sample in Fig. 4.5 shows aggregates of smaller and darker nanoscale particles and larger and brighter crystallites. This indicates that the former would have smaller molecular mass given the DF-STEM image. Indeed, the former is tin oxides with a negligible amount of Se atoms and the latter comprises significantly higher degree of Se than O atoms according to elemental scanning on the corresponding area and

quantitative analysis by STEM-EDS (Fig. 4.5). Interestingly, oxygen concentration is much higher at the edge than at the central part of the BM powders (Fig. 4.6). Accordingly, oxide aggregates would be broken out of powders by a ball mill process. They possibly exist as isolate nanoscale particles or form thin films on surfaces of powders. The observed features are commonly seen in the BM samples.

In contrast, the BR sample shows a relatively well-ordered nanoscale grains with recovered high crystallinity according to representative low-magnification STEM image and the corresponding FFT images at the different areas (Fig. 4.4b and insets). It consists of an appropriate ratio of Sn, Pb, and Se atoms with a trace of O atom as given by elemental scanning on the corresponding area and quantitative analysis by STEM-EDS (Fig. 4.7). However, some powders are still found to show a significant level of oxygen even after a reduction process. It should be noted that although the current STEM-EDS technique cannot provide high accuracy in chemical compositions inherently and oxygen is always detected in quantitative analysis, the results are enough to give a relative abundance for constituent elements in the materials.

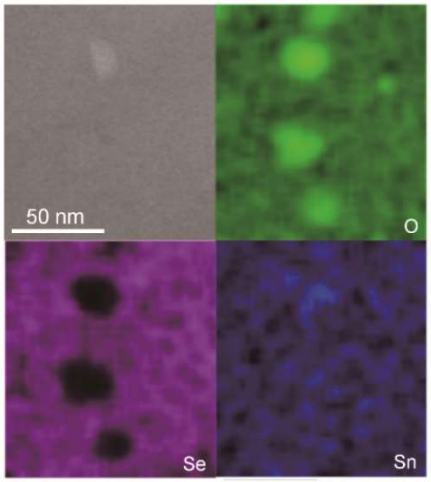

Figure 4.3. Typical Cs-STEM images and elemental mappings by STEM-EDS. Low-magnification annular bright-field STEM image and the corresponding elemental mappings scanned on the entire area in the upper left panel by STEM-EDS for the SPS-processed pristine sample. The other panels display direct EDS signals from O, Se, and Sn atoms in that area. Formation of tin oxide nanoscale precipitates are clearly observed.

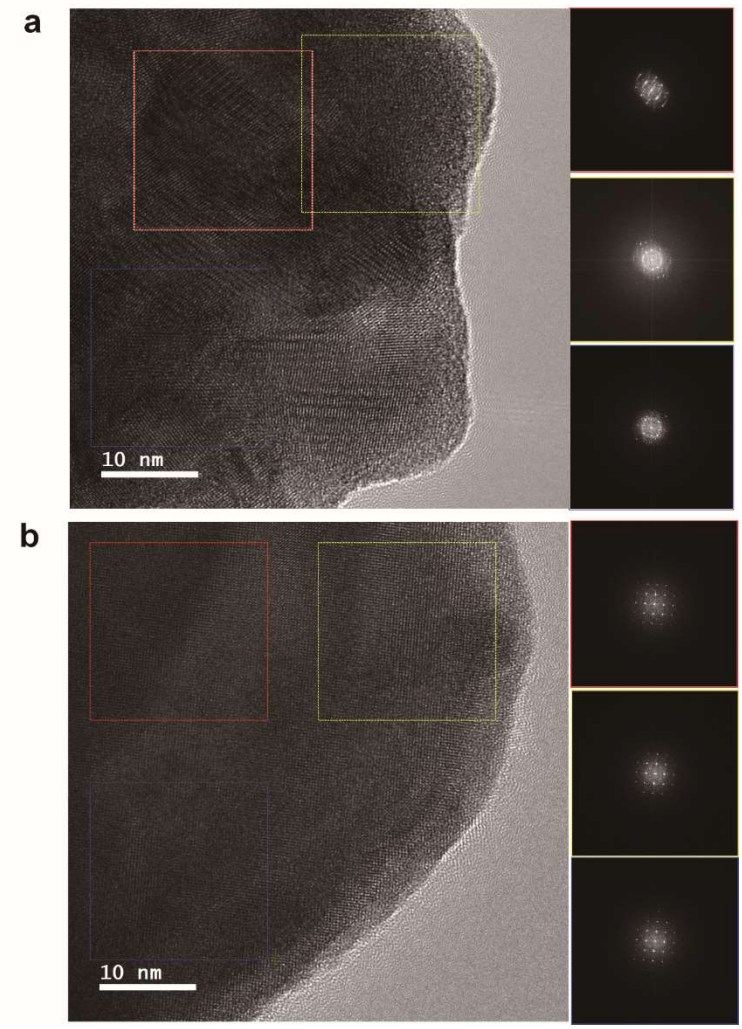

Figure 4.4. Cs-STEM images of (a) BM and (b) BR powders and their corresponding FFT images taken at different areas (insets). The scale bar is 10 nm.

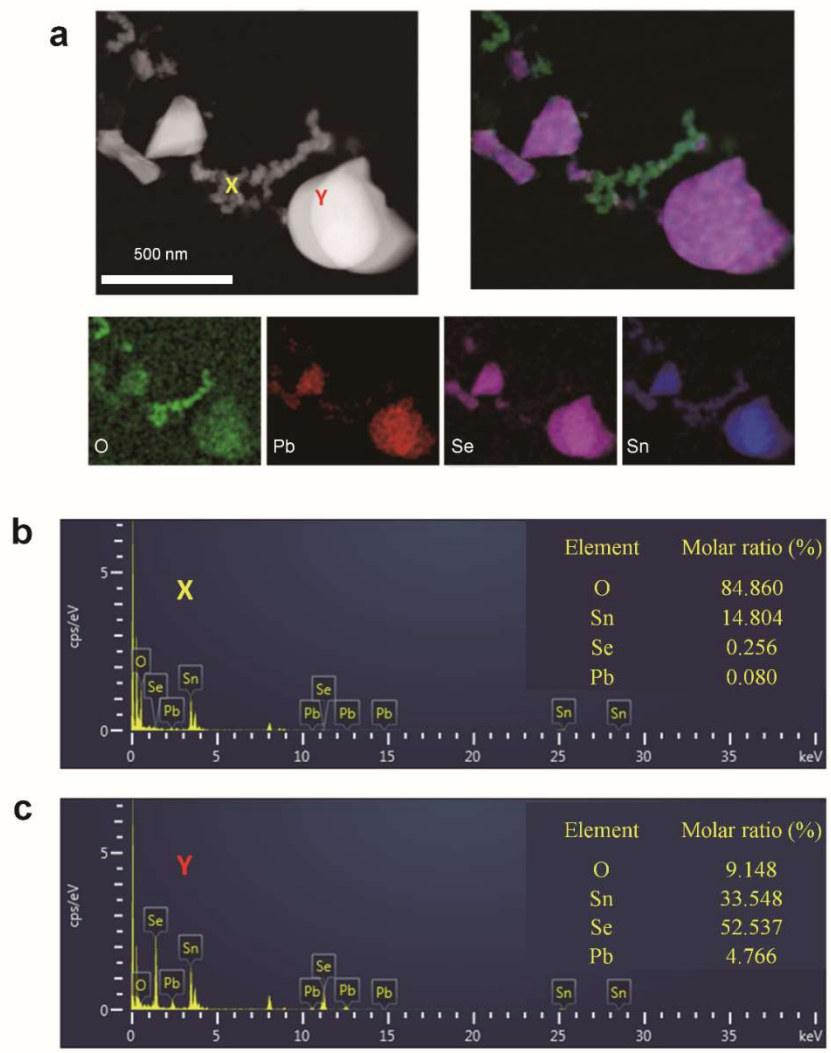

Figure 4.5. Quantitative elemental analysis taken at the points (b) X and (c) Y. It should be noted that although STEM-EDS cannot provide high accuracy in chemical compositions, the results are enough to give a relative abundance for constituent atoms in the materials.

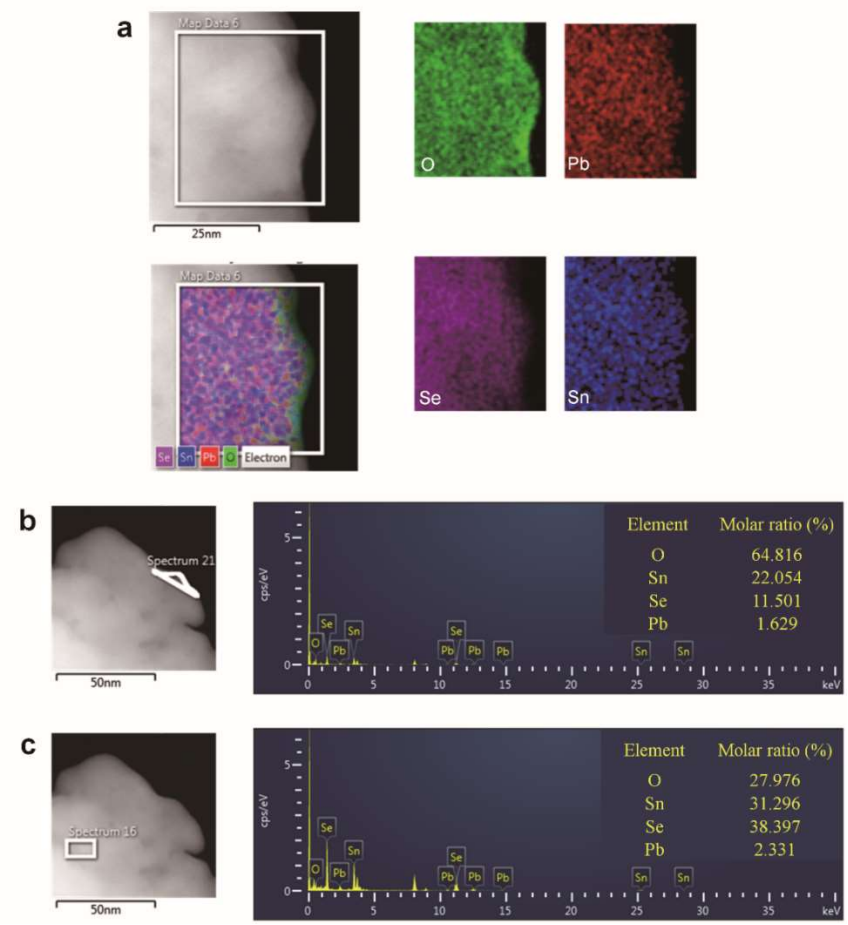

Figure 4.6. DF-STEM image and quantitative elemental analysis by STEM-EDS at the selected areas by STEM-EDS in the BM powders. Quantitative STEM-EDS analysis taken (b) at the edge area and (c) in the central shows oxygen atoms are more abundant at the edges than in the central area of the BM powders, indicating that tin oxide contaminants form thin films on the surfaces of the BM powders.

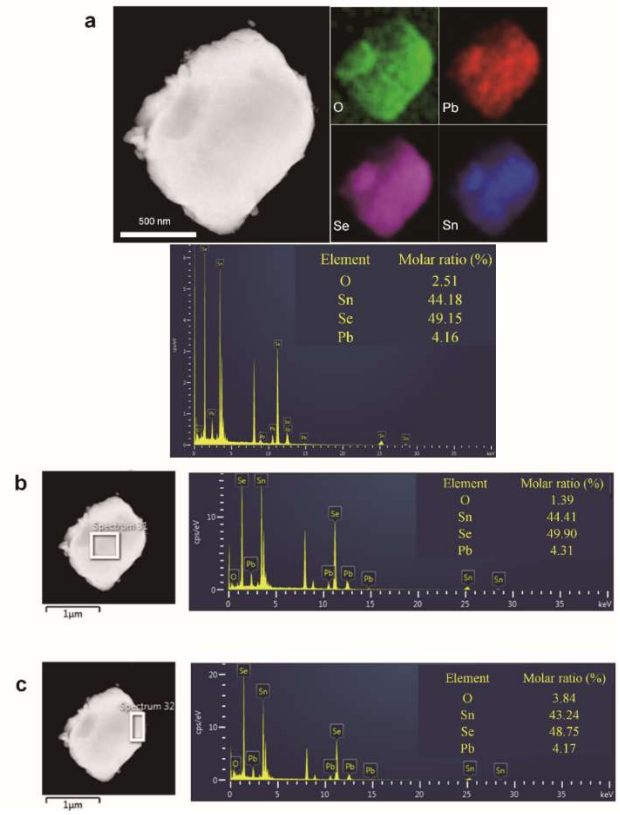

Figure 4.7. Typical DF-STEM image and quantitative elemental analysis by STEM-EDS for the BR powders. A negligible amount of oxygen atom in BR powders. a, DF-STEM image and elemental mappings of the constituent elements and quantitative analysis by STEM-EDS on the entire powders. Quantitative STEM-EDS analysis taken (b) in the central and (c) at the edge area shows that oxygen atoms are more abundant at the latter, indicating tin oxide contaminants form thin films on the surfaces of the powders.

We further investigated the surface state of BM and BR powders by X-ray photoemission spectroscopy (XPS) (Fig. 4.8). To directly observe surface overlayers of oxide contaminants, we did not perform any surface treatment such as ion sputtering and mechanical cleaning. For both samples, the Sn $3d_{3/2}$ and $3d_{5/2}$ peaks are split into two profiles, indicating the two different oxidation states in Sn. The deconvoluted peaks of 494.7 and 486.3 eV are clearly assigned to the Sn $3d_{3/2}$ and $3d_{5/2}$ peaks from SnO_2. Note that the binding energy of Sn $3d_{3/2}$ and $3d_{5/2}$ for SnO and SnSe is too close to be deconvoluted each other. On that account, those of 493.2 and 484.8 eV mainly correspond to the Sn $3d_{3/2}$ and $3d_{5/2}$ peaks from SnSe while the presence of SnO cannot be excluded [32]. The XPS data demonstrate that a ratio of SnSe to SnO_2 is 1.15 for the BM sample and is raised to 1.36 for the BR sample. The latter also shows the greatly reduced oxygen concentration. These observations reveal that a substantial degree of tin oxides (SnO_2 and SnO) exists in SnSe-based materials, even considering that facile adsorption of oxygen on surfaces of samples can lead to its exaggerated concentration. More vigorous reduction conditions may results in lower oxygen concentration in samples. It is important to note that the presence of Sn^{4+} species and the resulting structural change were not observed by X-ray absorption near edge spectroscopy (XANES) and extended X-ray absorption fine structure (EXAFS) employing synchrotron X-ray for both samples. This suggests that only a remnant of tin oxides forms thin films on the surface of the powders.

Diffuse reflectance measurement on pristine sample shows an absorption

edge at 0.88 eV (Fig. 4.9). A ball mill process does not change this feature. Interestingly, the BR sample exhibits a much steeper and blue-shifted absorption edge at 0.97 eV. This observation indicates that a reduction process removes tin oxide residues and defect states, thereby unveiling intrinsic absorption spectrum of this material. Indeed, SnO bulk powders displays a well-known direct band gap at ~2.7 eV with extended band tailing down to ~0.7 eV due to an indirect band gap [33]. Similarly, the BM and BR processed samples of undoped SnSe powders give an energy gap at 0.91 and 0.98 eV with a steeper absorption edge in the latter.

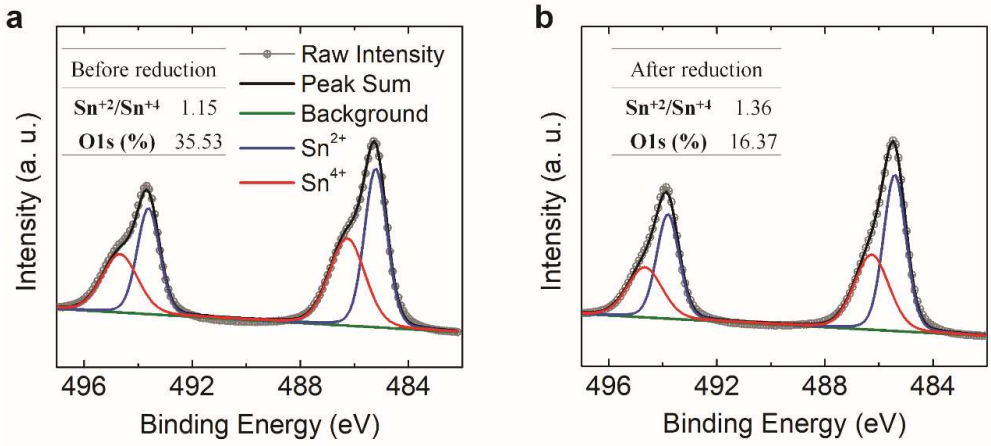

Figure 4.8. X-ray photoemission spectra of Sn $3d_{3/2}$ and $3d_{5/2}$ core states of (a) BM and (b) BR powders.

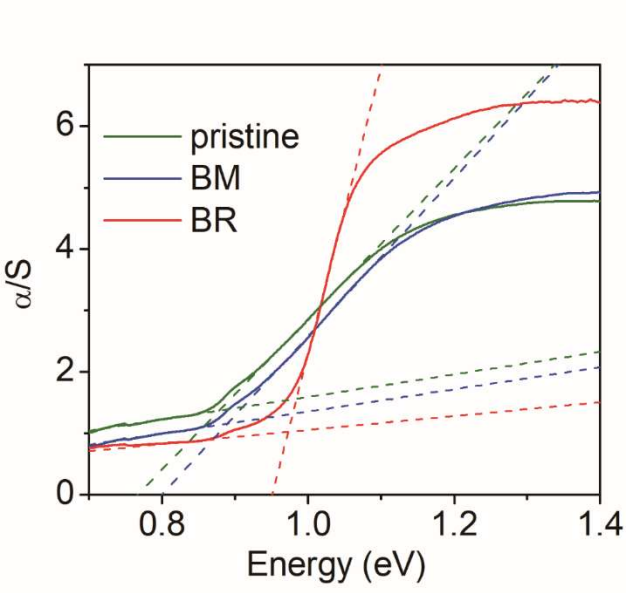

Figure 4.9. Optical absorption spectra for the Bulk, BM and BR sample at room temperature. A blue-shifted energy gap with a much steeper absorption edge is clearly observed.

To investigate the effect of a ball mill and a reduction process, we characterized electrical and thermal transport properties of pristine, BM, RD, and BR samples both parallel and perpendicular to the press direction of SPS (Fig. 4.10). Note that we will mainly focus on them along the former direction that shows higher ZT, if noted otherwise. The temperature-dependent Hall effect measurement shows that the μ_H at 300 K for pristine, BM, and BR samples is low at 1.85, 0.47, and 3.90 $cm^2\ V^{-1}\ s^{-1}$ (Fig. 4.11). However, μ_H of the BR sample greatly deviates from the others with rising temperature. It increases rapidly from 300 to ~450 K, subsequently decreases up to ~573 K, and sharply rises afterward. Its μ_H at 773 K is 46.7 $cm^2\ V^{-1}\ s^{-1}$, which is nearly 10 times larger than that of pristine. Its carrier concentration (n_H) is nearly constant at ~$1 - 2 \times 10^{19}$ cm^3 from 300 to 773 K, slightly lower than ~$3 - 4 \times 10^{19}$ cm^3 of pristine in the same temperature range.

Fig. 4.12a shows electrical conductivity (σ) of the samples. The enhanced μ_H by a reduction process is directly reflected on σ of the reduced samples because of their almost constant n_H with respect to temperature. The 'S'-like trend of σ curves of the BR and RD samples resembles of those of μ_H. The former shows higher σ than the latter above ~573 K and reaches a maximum (σ_{max}) of 93.2 S cm^{-2}, which is about two time larger than pristine and the BM samples. The BR sample shows the different trend of Seebeck coefficient (*S*) with respect to temperature from the others (Fig. 4.12b). It monotonously increases to reach ~+375 $\mu V\ K^{-1}$ at 673 K and subsequently

decreases to +271 μV K^{-1} at 773 K, showing higher values than the others over the entire temperature range. Interestingly, their *S* values measured parallel and perpendicular directions of the press are nearly the same (Fig. 4.10). The improved σ and *S* in the mid temperature range from ~450 to 600 K result in relatively high power factor (σS^2) for SnSe-based materials of ~5 – 5.5 μW cm^{-1} K^{-1} forming a plateau. The BR sample reaches the remarkably enhanced power factor of 6.85 μW cm^{-1} K^{-1} at 773 K in comparison with 3.12 and 3.23 μW cm^{-1} K^{-1} for pristine and the BM samples. The reduced sample without a ball mill process also gives the increased power factor of 4.85 μW cm^{-1} K^{-2} (Fig. 4.12).

κ_{tot} of the BR sample decreases continuously up to 773 K with increasing temperature. It is lower than that of pristine over the entire range of temperature. Note that κ_{tot} of pristine decreases sluggishly and deviates largely from that of the BR sample above ~673 K. The BM sample displays lower κ_{tot} than the BR sample up to ~723 K. This observation can be attributed to the nanoscale powders involving partially amorphous regions generated by a ball mill process as observed in the PXRD and STEM results (Fig. 4.2 and 4.5). Phonon scattering at grain boundaries and amorphous areas can suppress thermal conductivity. However, κ_{tot} of the BM and RD samples upturns above ~723 K, which is earlier than ~773 K of the BR sample and undoped and Na-doped SnSe single crystals.

The BR sample reaches a minimum κ_{tot} of ~0.20 W m^{-1} K^{-1} at 773 K. This

value is about a half of ~0.38 W m^{-1} K^{-1} of the others and is also lower than the κ_{tot} of undoped and Na-doped SnSe single crystals along the *a* axis, which is the out-of-plane direction giving the lowest κ_{tot} of SnSe materials (Fig. 4.13a). Up to ~750 K, its κ_{tot} is similar to and slightly higher than that for single crystals of SnSe along the *b* (in-plane) axis and Na-doped SnSe along the *a* axis, respectively. This observation can be ascribed to tin oxides that remain in the BR sample as observed in the STEM and XPS results. More harsh reduction processes or rigorous purification of reactant elements can further decrease κ_{tot} of polycrystalline SnSe materials. A ratio of lattice thermal conductivity (κ_{lat}) to κ_{tot} demonstrates that lattice vibrations dominate κ_{tot} (Fig. 4.14). The BR sample shows a minimum κ_{lat} of ~0.11 W m^{-1} K^{-1} at 773 K (Fig. 4.15). This value is about one third of pristine (~0.31 W m^{-1} K^{-1}) and a half of SnSe single crystals (~0.20 W m^{-1} K^{-1}). These results clearly confirm that ultralow thermal conductivity is intrinsic for SnSe materials, and their polycrystals indeed exhibit lower κ_{lat} than corresponding single crystals.

It is important to note that κ_{tot} of pristine and the BR sample at 773 K is ~0.38 and 0.20 W m^{-1} K^{-1}, and only 0.18 W m^{-1} K^{-1} difference between them corresponds to the raised κ_{tot} in pristine by almost a factor of two, leading to hugely damaged ZT. If κ_{tot} of materials were larger than unity, the same level of oxide impurity will not be as influential as in SnSe-based materials with ultralow κ_{tot}. Many research groups have obtained higher κ_{lat} in polycrystalline SnSe materials than that

of single crystals. The main reason can be explained in light of the characteristic difference in preparing single crystal and polycrystalline specimens. We found that tin oxides form thin films on microscale powders in this work. A consolidation process such as SPS spreads oxide films on grain boundaries throughout dense pellets. Consequentially, grain boundaries could even boost phonon transport rather than impede it because SnO_2 has ~140 fold larger thermal conductivity than SnSe. In contrast, high quality SnSe single crystals are typically synthesized by a Bridgman crystal growth method. This technique moves the SnSe melt in a conical reaction tube vertically with prolonged time. Immediately the melt passes a hot zone, crystals begin to grow at the bottom of a tube. During this process, impurities that are either less dense or more volatile tend to be expelled out and can be readily removed. Note that atomic mass of oxygen and selenium is 16.00 and 78.96 g mol^{-1}. Then, obtained single crystals are much purer than polycrystals, and can be nearly oxide-free. This process may induce vacancy because of the temperature gradient and elongated growth time.

Facile ball mill and reduction processes in this work uncover intrinsically high TE performance in polycrystalline SnSe materials with excellent reproducibility. We prepared twelve independent BR specimens, and their ultralow κ_{tot} was cross-confirmed from Seoul National University (SNU), Northwestern University (NU), and Netzsch instruments (Fig. 4.16). The uncertainty of κ_{tot} for those specimens (8 from SNU, 3 from NU, and 1 from Netzsch) ranges from 7 to 20 % in the temperature

range from 300 to 773 K. Note that this uncertainty originates both from individual specimens and instruments. Their average κ_{tot} at 773 K is ~0.209 W m^{-1} K^{-1}, confirming high reproducibility of intrinsically ultralow thermal conductivity of polycrystalline SnSe-based materials. Reproducibility tests for σ and *S* are also given in Fig. 4.17. Pristine, BM, RD, and BR samples show a negligible weight loss up to 800 K under an Ar flow according to thermogravimetric analysis, indicating their high thermal stability (Fig. 4.18).

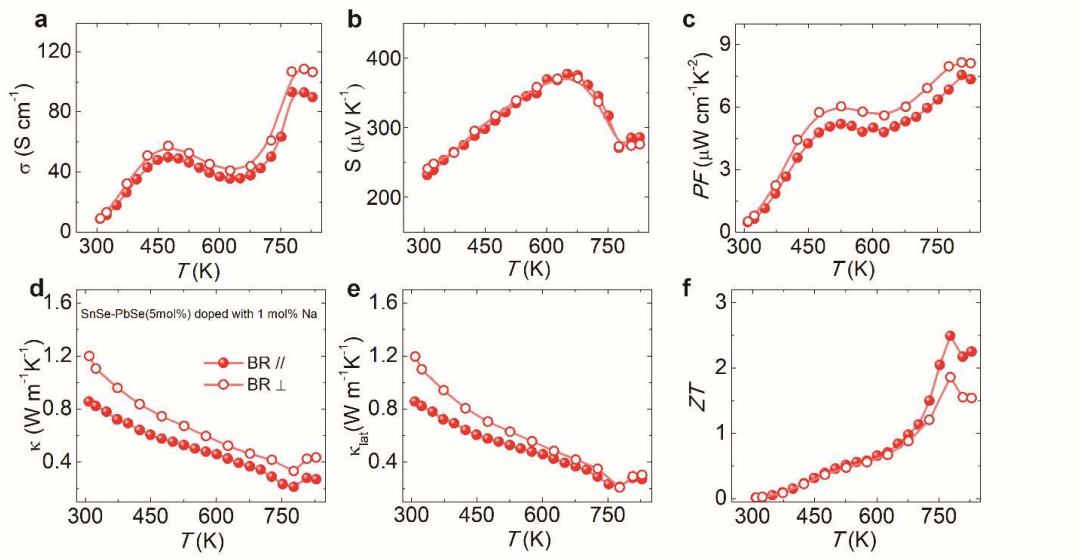

Figure 4.10. Thermoelectric properties as a function of temperature for the BR sample (a) Electrical conductivity, (b) Seebeck coefficient, (c) power factor (*PF*), (d), total thermal conductivity, (e) lattice thermal conductivity, and (f) *ZT* values taken parallel and perpendicular to the press direction of SPS. The typical uncertainty for *ZT* estimates is approximately 15-20%.

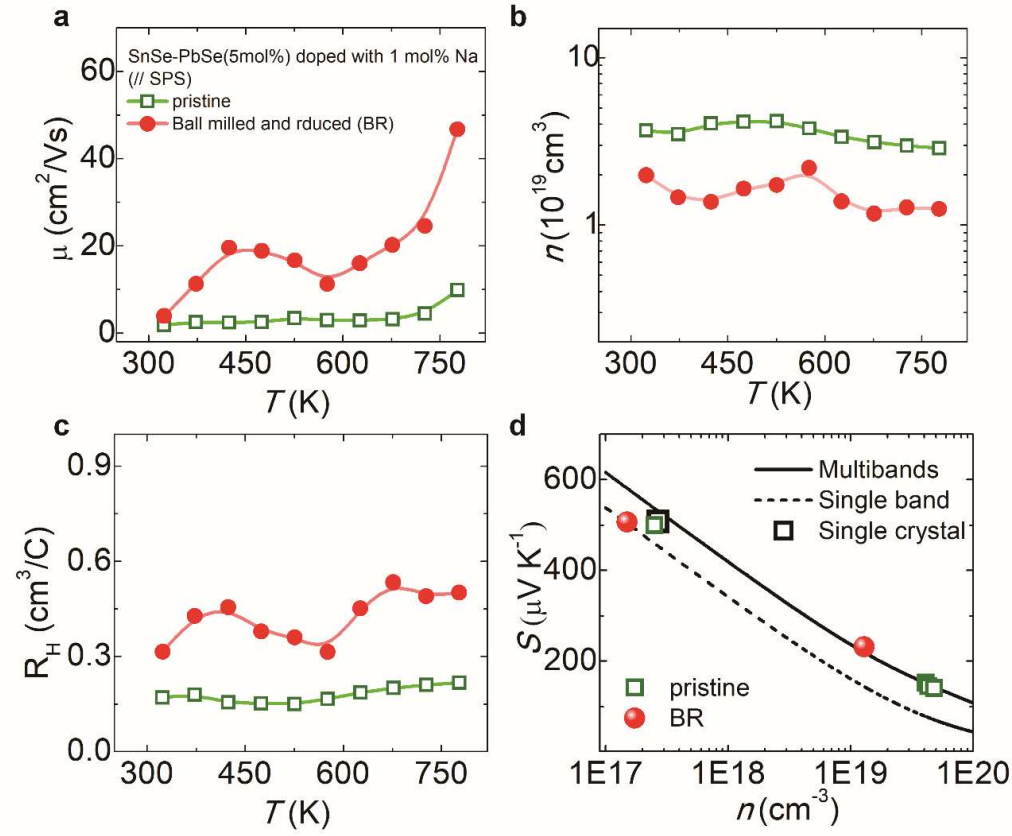

Figure 4.11. Hall transport properties of the pristine, and BR samples with respect to temperature and Pisarenko lines. a, Carrier mobility. b, Carrier concentration. c, Hall coefficient. d, Pisarenko relations of S with respect to n_H based on a single parabolic band model with the effective mass of $m = 0.47m_0$ and a multivalley band model for SnSe and their comparison with the experimental S values at 300 K.

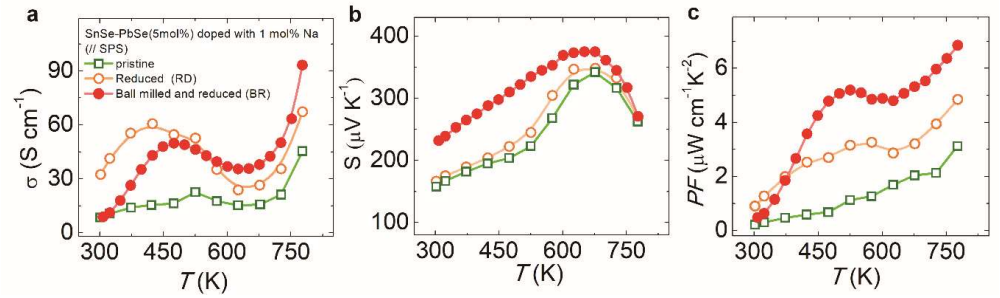

Figure 4.12. Charge transport properties of polycrystalline SnSe-PbSe(5 mol%) doped with 1 mol% Na samples. a, Electrical conductivity, **b**, Seebeck coefficient, and **c**, power factor (*PF*) with respect to temperature for pristine, RD, and BR samples taken parallel to the press direction of SPS.

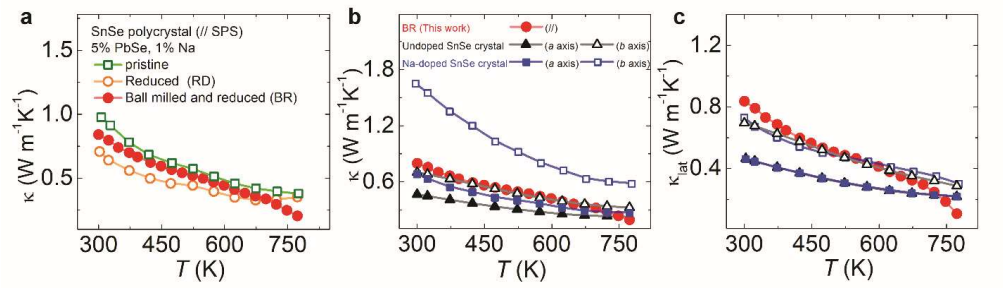

Figure 4.13. Thermal transport properties of polycrystalline SnSe-PbSe(5 mol%) doped with 1 mol% Na samples. a, Total thermal conductivity (κ_{tot}) for pristine, RD, and BR samples taken parallel to the press direction of SPS. **b**, κ_{tot} and **c**, lattice thermal conductivity (κ_{lat}) of the BR sample (//) are compared with those of undoped[20] and Na-doped SnSe single crystals[32] along the in plane (*a* axis) and out of plane (*b* axis) directions.

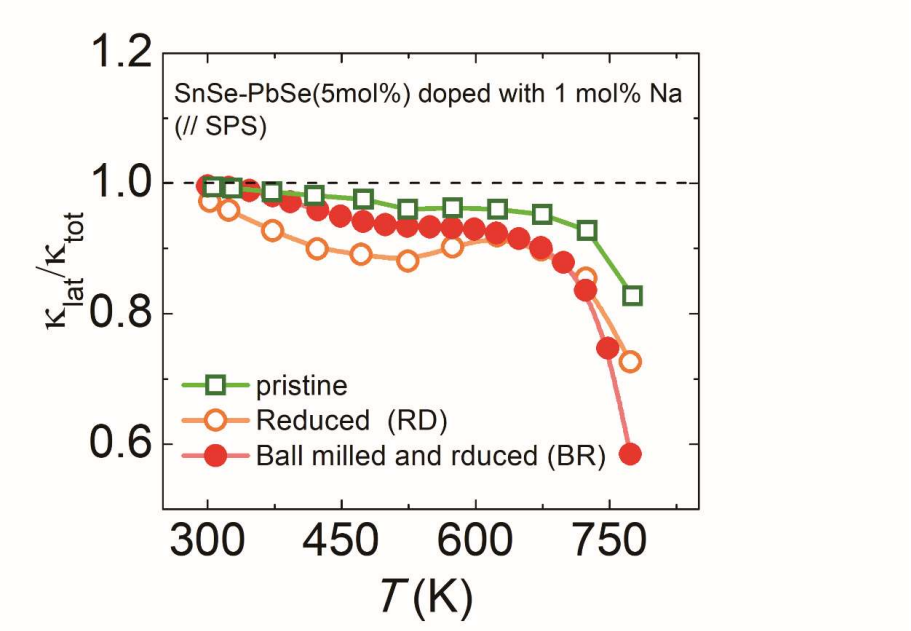

Figure 4.14. A ratio of lattice thermal conductivity to total thermal conductivity for the pristine, RD, and BR samples

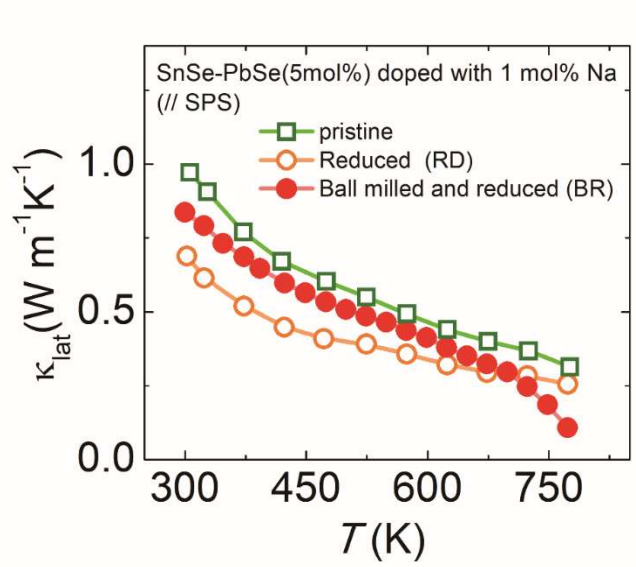

Figure 4.15. Lattice thermal conductivity for the pristine, RD, and BR samples

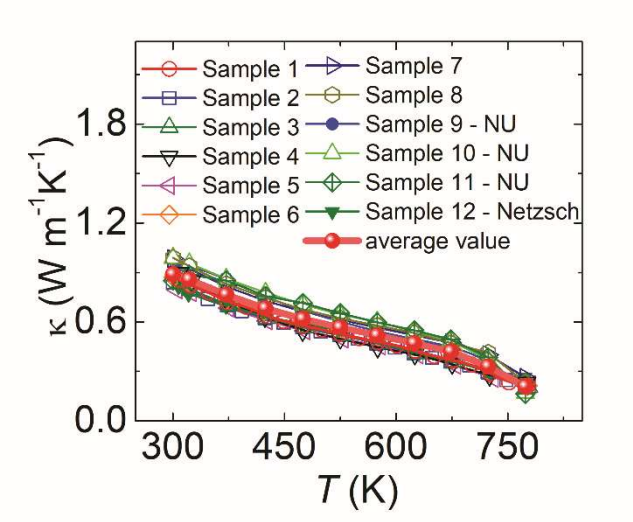

Figure 4.16. The reproducibility of total thermal conductivities (κ_{tot}) as a function of temperature for the BR samples of polycrystalline SnSe-PbSe(5 mol%) doped with 1 mol% Na. Twelve samples were independently prepared and characterized at Seoul National University (SNU, Samples 1-8), Northwestern University (NU, Samples 9-11), and Netzsch instruments (Netzsch, Sample 13). Ultralow κ_{tot} of the samples is highly reproducible. The uncertainty ranges from about 7 to 20 %. This value includes uncertainties from individual samples and three instruments from SNU, NU, and Netzsch. Note that the uncertainty for samples 1-8 measured in SNU is 11.1 % at 773 K. The relative density of all BR samples for the reproducibility test ranges from 93.9 to 95.6 % (average of the density: 94.6 %)

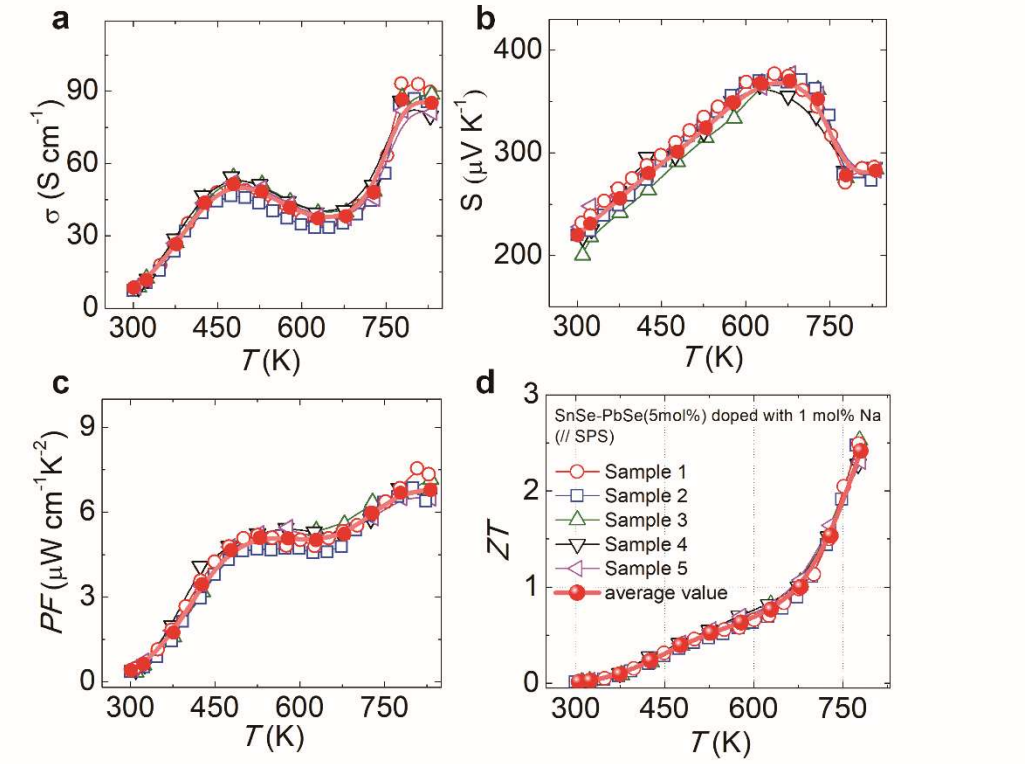

Figure 4.17. The reproducibility of thermoelectric properties as a function of temperature for the BR samples of SnSe-PbSe(5 mol%) doped with 1 mol% Na. (a) Electrical conductivity, (b), Seebeck coefficient, (c), power factor (*PF*), (d), ZT values were measured parallel to the press direction of SPS. The samples were independently prepared and measured. The average *ZT* of five individual samples reaches ~2.5 at 773 K. The typical uncertainty for *ZT* estimates is approximately 15-20%.

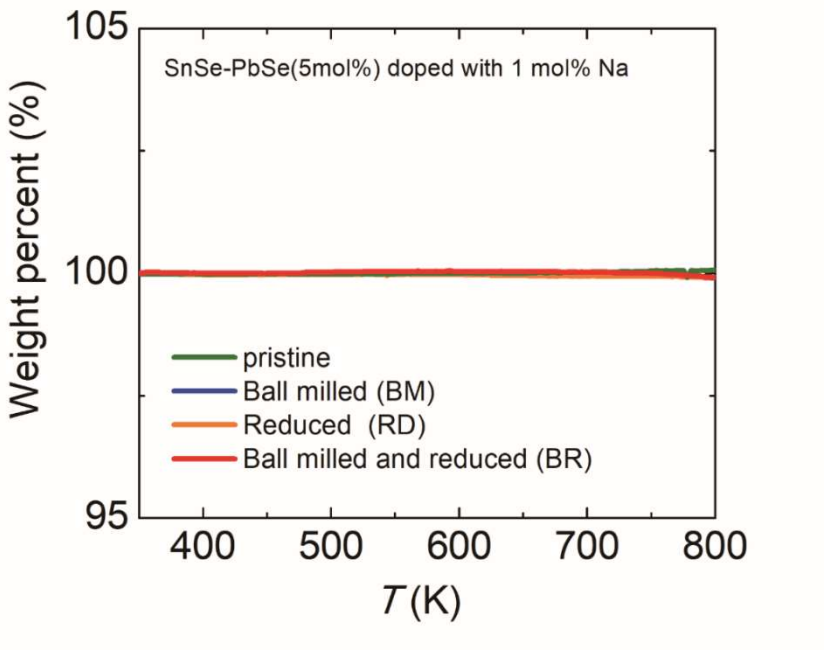

Figure 4.18. The thermogravimetric analysis (TGA) measurements for the pristine, BM, RD, and BR samples of SnSe-PbSe(5 mol%) doped with 1 mol% Na under an Ar flow at a rate of 10 K min^{-1}. SPS processed ingots were ground into fine powders and measured. The weight loss is nearly negligible up to 800 K.

Undoped and Na-doped p-type SnSe single crystals exhibit highly anisotropic TE properties. Along the *b* and *a* axes, the former shows ZT_{max} of ~2.6 and 0.8 at 923 K and the latter ~2.0 and 1.0 at 773 K, respectively. In contrast, the BR sample shows much less anisotropy in TE properties. Its ZT_{max} parallel and perpendicular to the press direction of SPS is ~2.5 and 1.8 at 773 K, respectively. σ is higher along the latter direction over the full temperature range, giving a σ_{max} of 106.7 S cm^{-1} compared with 93.2 S cm^{-1} along the former direction. These values are exceedingly higher than those reported for other polycrystalline SnSe-based materials. In comparison, undoped and Na-doped SnSe single crystals show σ of ~85 and 148 S cm^{-1} along the *b* axis (in plane) and ~14 and ~40 S cm^{-1} along the *a* axis (out of plane), respectively. *S* along the both directions are nearly the same. As a result, power factor is slightly higher along the latter direction to give 7.96 μW cm^{-1} K^{-1} at 773 K and a maximum of 8.14 μW cm^{-1} K^{-1} at 800 K. κ_{tot} at 300 K perpendicular to the press direction is 1.20 W m^{-1} K^{-1} and rapidly decreases with increasing temperature to reach a minimum of 0.33 W m^{-1} K^{-1} 773 K, slightly higher than 0.20 W m^{-1} K^{-1} parallel to the press direction. However, such a small deviation results in a large difference in ZT along those directions. κ_{lat} along both directions gets closer with increasing temperature and nearly the same above 773 K in contrast to κ_{tot}. Relatively low anisotropy in TE properties can be explained by the results of the XRD patterns of the SPS pellets taken perpendicular plane to the pressing direction (Fig 4.19). The BR sample has a much less degree of preferred orientation

for the (*h*00) with respect to the (*hkl*) reflections than pristine. The Lotgering factor decreases from 0.302 of the former to 0.185 for the latter (Fig. 4.19 and Table 4.2).

4.4 Conclusion

We demonstrate that a facile reduction process can unveil the underestimated thermoelectric performance of polycrystalline SnSe materials. Simultaneous enhancement in electrical conductivity and Seebeck coefficient, coupled with the lowest lattice thermal conductivity reported to date, leads to extraordinarily high ZT ~2.5. Their performance in the low to mid temperature range can be further enhanced considering a record-high device ZT of Na-doped SnSe single crystals. They are exceptional from other high performance thermoelectric systems, given high thermal stability, easy preparation processes, earth crust-abundant constituent elements without scarce Te, and highly reproducible thermoelectric performance. These advantages improve the prospects of establishing high efficiency thermoelectric modules operating in the mid to high temperature range.

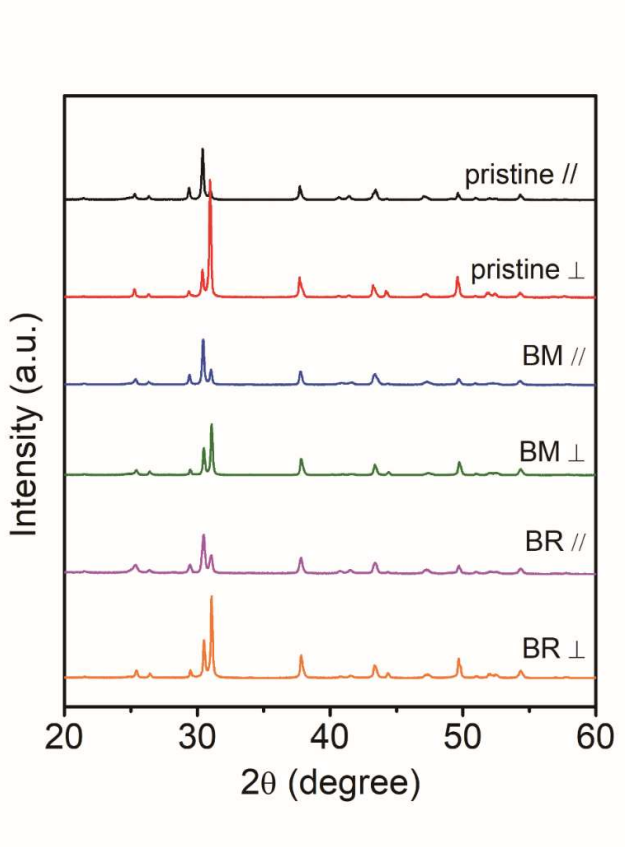

Figure 4.19. Powder X-ray diffraction patterns of SPS processed pellets taken parallel and perpendicular planes to the pressing direction of SPS. The Lotgering factor is given in Supplementary Table 4.2.

Table 4.2. Comparison of Lotgering factor for the pristine, BM, and BR samples.

To understand the structurally anisotropic nature of SnSe-PbSe(5 mol%) doped with 1 mol% Na, we estimated a degree of preferred orientation of the pellet parallel and perpendicular to the pressing direction of SPS based on the XRD patterns of pristine, BM and BR samples (Figure S17). The Lotgering factor (*LF*) is commonly employed to quantify the degree of preferred orientation of a given material. The *LF* is defined by the following equation:

$$LF = \frac{(p - p_0)}{(1 - p_0)}, \quad p = \frac{\sum I_{h00}}{\sum I_{hkl}}$$

Where *p* is the degree of orientation regarding a preferred orientation, p_0 is the degree of orientation regarding a random orientation, and $\sum I_{00l}$ and $\sum I_{hk}$ are the sums of peak intensities of the (*h*00) and (*hkl*) reflections in the 2θ range from 10° to 60°. Accordingly, *LF* is 1 for a perfect (*h*00)-plane preferential orientation according to the equation 1. We chose the peak of (400) as the dominant peak of (*h*00). The LF_{004} values for pristine, BM, and BR samples parallel to the press direction are 0.302, 0.157, and 0.185, respectively. The BR sample shows smaller preferred orientation to the (*h*00) reflections than the pristine.

Sample	Lotgering factor (400)
pristine SnSe-PbSe(5 mol%) doped with 1 mol% Na ⊥	0.302
Ball-mill SnSe-PbSe(5 mol%) doped with 1 mol% Na ⊥	0.157
Ball-mill and reduced SnSe-PbSe(5 mol%) doped with 1 mol% Na ⊥	0.185

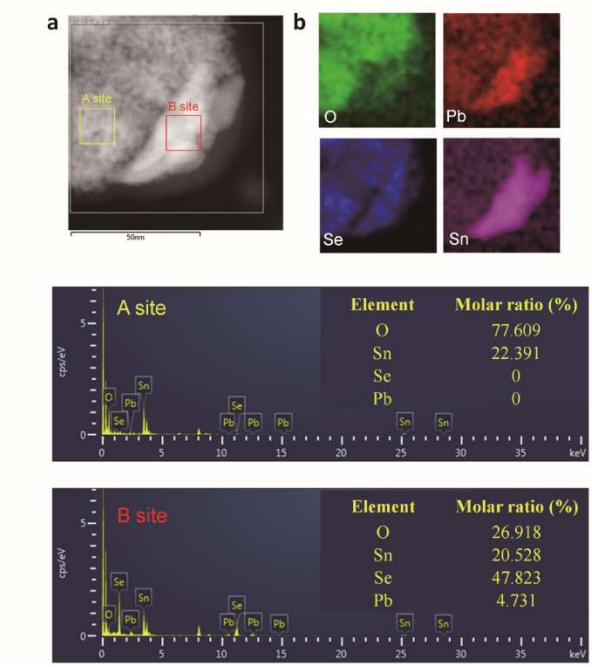

Figure 4.20. Typical dark field (DF) Cs-STEM image and elemental mappings of BM powders by STEM-EDS. a, STEM image of BM powders. Brighter and larger crystallites are seen in the lower right part. Darker aggregates of smaller nanoscale particles are found in other areas. Given DF STEM image, it is highly probable that the latter consists of lighter molecular mass. Indeed, it comprises Sn and O atoms devoid of Pb and O atoms, according to the qualitative STEM-EDS analysis taken at the A site. On the other hand, the former contains a much higher concentration of Se than O atom. b, The corresponding elemental mapping scanned on the entire area of a. The respective STEM-EDS signals were directly obtained from O, Pb, Sn, and Se atoms. According to the quantitative STEM-EDS results, the site A only consists of Sn and O atoms devoid of Se and Pb atoms.

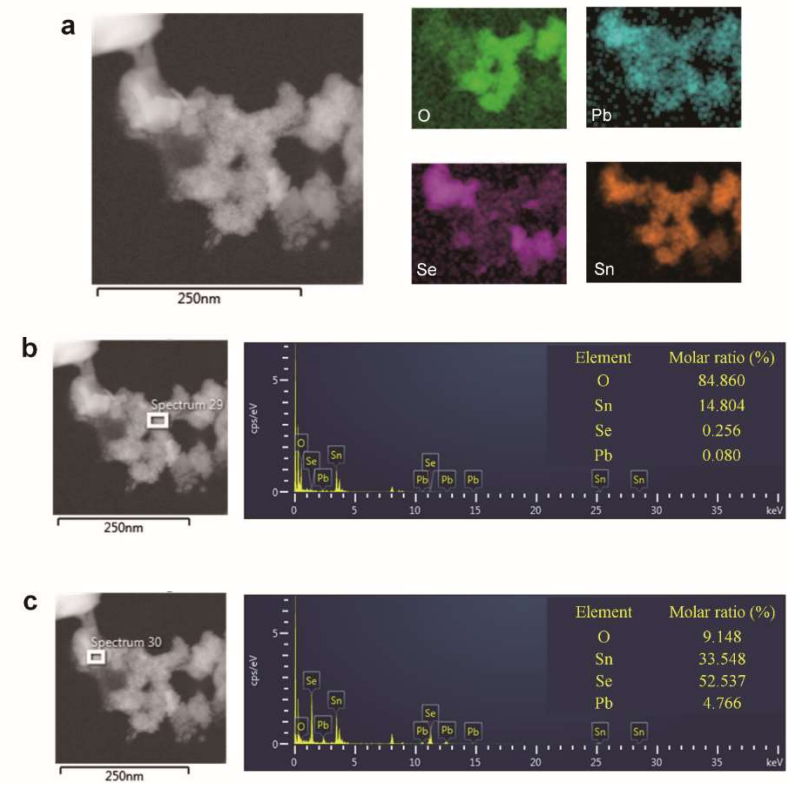

Figure 4.21. Typical dark field Cs-STEM image and elemental mappings of BM powders by STEM-EDS. a, STEM image. Cloudy aggregates of nanoscale particles are found at the central and right area. Brighter and larger crystallites are observed in the left area. b, The corresponding elemental mappings scanned on the red rectangle area of a. The respective STEM-EDS signals were directly obtained from O, Pb, Sn, and Se atoms. c, According to the quantitative STEM-EDS results, the site A consists of Sn and O atoms with a negligible amount of Se atom. The site B comprises a much higher content of Se than O atoms.

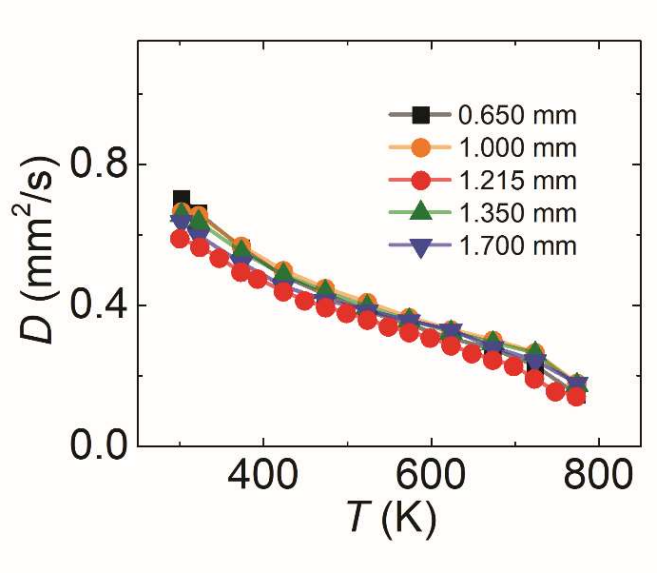

Figure 4.22. Thermal diffusivities of BR samples with a different thickness parallel to the press direction of SPS. Each specimen with a different thickness was prepared from the different synthesis batches to ensure the reliability of confirming the relationship between the thermal diffusivity and the specimen thickness. The deviation in thermal diffusivity among those specimens is negligible. The standard deviation among their thermal diffusivities is only 7.3% at 773 K, in which this material exhibits a peak ZT of ~2.5. This result also verifies the high reproducibility of ultralow intrinsic thermal conductivity of our SnSe-based material.

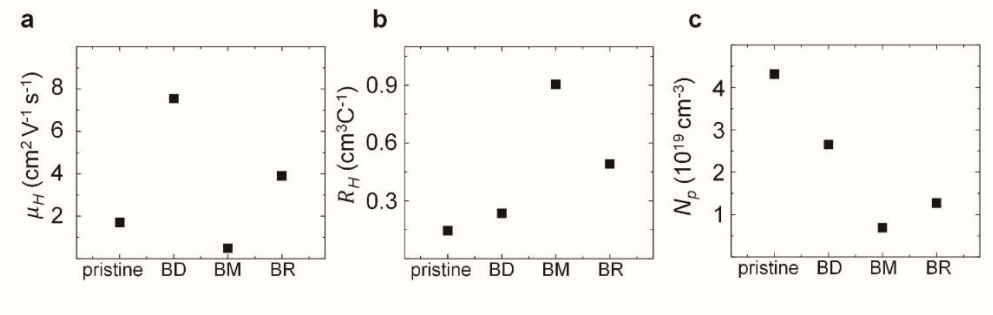

Figure 4.23. Hall transport properties for the pristine, BM, RD, and BR samples at 300 K. a, Carrier mobility. b, Hall coefficient. c, Carrier concentration.

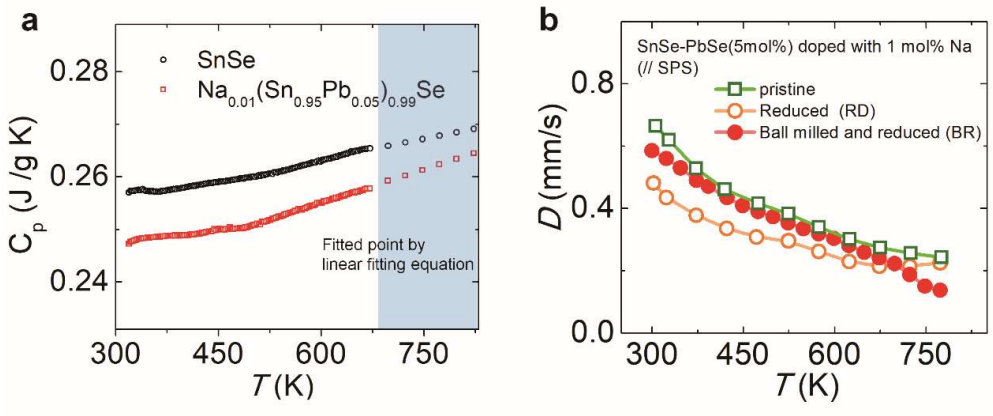

Figure 4.24. a, The heat capacity (C_p) of SnSe and SnSe-PbSe(5 mol%) doped with 1 mol% Na in the temperature range from 300 to 673 K and the predicted heat capacity by a linear fitting. b, Thermal diffusivity as a function of temperature of the pristine, RD, and BR samples taken parallel to the press direction of SPS.

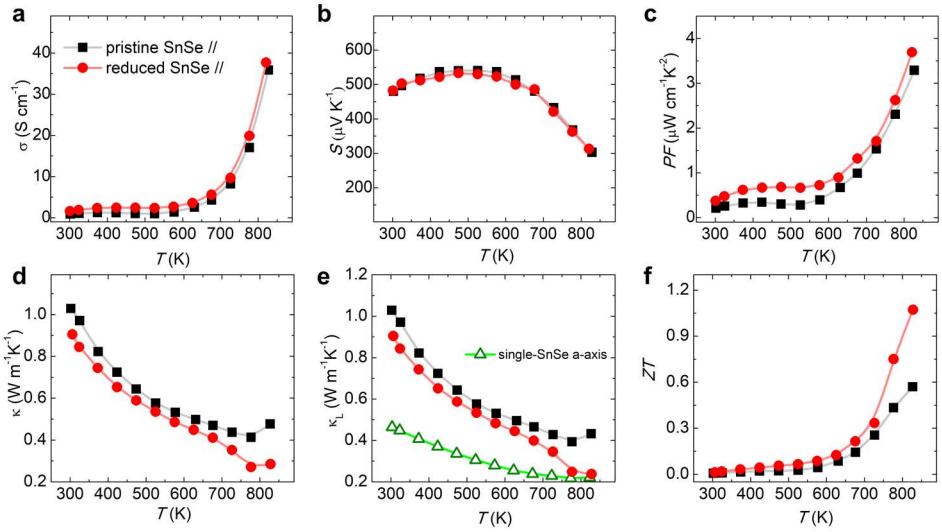

Figure 4.25. Thermoelectric properties as a function of temperature for undoped polycrystalline SnSe. Those of pristine and the ball-milled and subsequently reduced samples were characterized parallel to the press direction of SPS. **a.** Electrical conductivity (σ). **b.** Seebeck coefficient (*S*). **c.** Power factor (*PF*). **d.** Total thermal conductivity (κ). **e.** Lattice thermal conductivity (κ_L). The κ_L along the *a* axis for single crystal SnSe is given for comparison[20]. Its κ_L is the lowest along the *a* axis **f.** *ZT* values. It should be noted that the sample preparation processes such as the condition of H_2-reduction was not optimized for these samples in contrast to the case of the BR sample. Accordingly, their thermoelectric properties can be much improved by further optimization processes. However, a reduction in κ and ZT by the H_2 reduction is clearly observed.

Thermal Diffusivity - NETZSCH LFA Analysis

General information

Database :	nkslab-18010.mdb	**Operator :**	---
Instrument :	LFA 467	**Remark(mment) :**	---
Identity :	NKSLAB-18010	**Cp table :**	Na0.01(Sn0.95Pb0.05)0.99Se_1 - A1
Date :	6/8/2018	**Expansion table :**	dL_const
Material :	Na0.01(Sn0.95Pb0.05)0.99Se_1 - A1	**Furnace :**	LFA 467 Steel
Ref. density (20.0 °C) /(g/cm^3) :	5.900	**Sample holder :**	4 samples round/12.7mm
Sample :	Na0.01(Sn0.95Pb0.05)0.99Se_1	**Lamp :**	LFA 467 Flash Lamp
Type :	Single layer	**Furnace TC :**	E
Sample position :	A1	**Sample TC :**	E
Detection Area (Diameter)/mm :	8.8	**Sample Xp / Tn :**	4.00 / 4.00
Filter/% :	0	**Furnace Xp / Tn :**	4.00 / 4.00
Thickness (RT) /mm :	1.5800	**Calculation code :**	Standard + p.c./I/1-0-0
Diameter /mm :	12.500	**Purge 2 MFC**	ARGON
Sensor :	InSb	**Protective MFC**	ARGON

Results

Shot number	Temperature °C	Model	Diffusivity mm^2/s	Uncertainty %	Laser voltage V	Pulse width ms
1	25.2	Standard + p.c.(I)	0.560	0.1	260.0	0.60
2	25.1	Standard + p.c.(I)	0.562	0.3	260.0	0.60
3	25.0	Standard + p.c.(I)	0.561	0.3	260.0	0.60
Mean:	**25.1**		**0.561**			
Std. Dev.:	**0.1**		**0.001**			
4	50.1	Standard + p.c.(I)	0.527	0.2	260.0	0.60
5	50.0	Standard + p.c.(I)	0.527	0.2	260.0	0.60
6	50.0	Standard + p.c.(I)	0.529	0.2	260.0	0.60
Mean:	**50.1**		**0.528**			
Std. Dev.:	**0.0**		**0.001**			
7	100.1	Standard + p.c.(I)	0.474	0.1	260.0	0.60
8	100.0	Standard + p.c.(I)	0.477	0.2	260.0	0.60
9	100.0	Standard + p.c.(I)	0.478	0.2	260.0	0.60
Mean:	**100.0**		**0.476**			
Std. Dev.:	**0.0**		**0.002**			
10	150.0	Standard + p.c.(I)	0.433	0.1	260.0	0.60
11	150.0	Standard + p.c.(I)	0.434	0.1	260.0	0.60
12	150.0	Standard + p.c.(I)	0.435	0.1	260.0	0.60
Mean:	**150.0**		**0.434**			
Std. Dev.:	**0.0**		**0.001**			
13	200.0	Standard + p.c.(I)	0.400	0.1	260.0	0.60
14	200.0	Standard + p.c.(I)	0.401	0.2	260.0	0.60
15	200.0	Standard + p.c.(I)	0.402	0.2	260.0	0.60
Mean:	**200.0**		**0.401**			
Std. Dev.:	**0.0**		**0.001**			
16	250.0	Standard + p.c.(I)	0.370	0.1	260.0	0.60
17	250.0	Standard + p.c.(I)	0.373	0.2	260.0	0.60
18	250.0	Standard + p.c.(I)	0.373	0.2	260.0	0.60
Mean:	**250.0**		**0.372**			
Std. Dev.:	**0.0**		**0.002**			
19	300.0	Standard + p.c.(I)	0.346	0.2	260.0	0.60
20	300.0	Standard + p.c.(I)	0.348	0.2	260.0	0.60
21	300.0	Standard + p.c.(I)	0.348	0.2	260.0	0.60
Mean:	**300.0**		**0.347**			
Std. Dev.:	**0.0**		**0.001**			
22	350.0	Standard + p.c.(I)	0.323	0.2	260.0	0.60
23	350.0	Standard + p.c.(I)	0.325	0.2	260.0	0.60
24	350.0	Standard + p.c.(I)	0.324	0.2	260.0	0.60
Mean:	**350.0**		**0.324**			
Std. Dev.:	**0.0**		**0.001**			
25	400.0	Standard + p.c.(I)	0.298	0.2	260.0	0.60
26	400.0	Standard + p.c.(I)	0.298	0.2	260.0	0.60
27	400.0	Standard + p.c.(I)	0.297	0.2	260.0	0.60
Mean:	**400.0**		**0.298**			
Std. Dev.:	**0.0**		**0.001**			
28	450.0	Standard + p.c.(I)	0.186	0.7	260.0	0.60
29	450.0	Standard + p.c.(I)	0.187	0.8	260.0	0.60
30	450.0	Standard + p.c.(I)	0.186	0.8	260.0	0.60
Mean:	**450.0**		**0.186**			
Std. Dev.:	**0.0**		**0.001**			
31	500.0	Standard + p.c.(I)	0.174	0.8	260.0	0.60
32	500.0	Standard + p.c.(I)	0.171	0.8	260.0	0.60
33	500.0	Standard + p.c.(I)	0.170	0.8	260.0	0.60
Mean:	**500.0**		**0.172**			

Created with NETZSCH Proteus software

Seonghwan Min, President
NETZSCH KOREA CO., LTD.
#83, Nocheom-Gil, Ilsandong-Gu
Goyang, Korea

Figure 4.26. The official test report for thermal diffusivity from NETZSCH Scientific Instruments Trading (Korea) Ltd.

4.5 References

1. Gingerich, D. B.; Mauter, M. S., Quantity, Quality, and Availability of Waste Heat from United States Thermal Power Generation. *Environmental Science & Technology* **2015,** *49* (14), 8297-8306.

2. Kanatzidis, M. G., Discovery-Synthesis, Design, and Prediction of Chalcogenide Phases. *Inorganic Chemistry* **2017,** *56* (6), 3158-3173.

3. Xianli, S.; Ping, W.; Han, L.; Wei, L.; Yonggao, Y.; Peng, L.; Chuqi, S.; Changjun, X.; Wenyu, Z.; Pengcheng, Z.; Qingjie, Z.; Xinfeng, T.; Ctirad, U., Thermoelectric Materials: Multi-Scale Microstructural Thermoelectric Materials: Transport Behavior, Non-Equilibrium Preparation, and Applications. *Adv. Mater.* **2017,** *29* (20).

4. J., V. C.; Ali, S.; Arun, M.; G., K. M., Nanostructured Thermoelectrics: Big Efficiency Gains from Small Features. *Adv. Mater.* **2010,** *22* (36), 3970-3980.

5. Lei, Y.; Zhi-Gang, C.; S., D. M.; Jin, Z., High Performance Thermoelectric Materials: Progress and Their Applications. *Adv. Energy Mater.* **2018,** *8* (6), 1701797.

6. Tan, G.; Zhao, L.-D.; Kanatzidis, M. G., Rationally Designing High-Performance Bulk Thermoelectric Materials. *Chemical Reviews* **2016,** *116* (19), 12123-12149.

7. Kanatzidis, M. G., Nanostructured Thermoelectrics: The New Paradigm? *Chemistry of Materials* **2010,** *22* (3), 648-659.

8. Lee, Y.; Lo, S.-H.; Chen, C.; Sun, H.; Chung, D.-Y.; Chasapis, T. C.; Uher, C.; Dravid, V. P.; Kanatzidis, M. G., Contrasting role of antimony and bismuth dopants on the thermoelectric performance of lead selenide. *Nat. Commun.* **2014,** *5*, 3640.

9. Park, K.; Ahn, K.; Cha, J.; Lee, S.; Chae, S. I.; Cho, S.-P.; Ryee, S.; Im, J.; Lee, J.; Park, S.-D.; Han, M. J.; Chung, I.; Hyeon, T., Extraordinary Off-Stoichiometric Bismuth Telluride for Enhanced n-Type Thermoelectric Power Factor. *J. Am. Chem. Soc.* **2016,** *138* (43), 14458-14468.

10. Lee, Y. K.; Ahn, K.; Cha, J.; Zhou, C.; Kim, H. S.; Choi, G.; Chae, S. I.; Park, J.-H.; Cho, S.-P.; Park, S. H.; Sung, Y.-E.; Lee, W. B.; Hyeon, T.; Chung, I., Enhancing p-Type Thermoelectric Performances of Polycrystalline SnSe via Tuning Phase Transition Temperature. *Journal of the American Chemical Society* **2017,** *139* (31), 10887-10896.

11. Zhao, L.-D.; Dravid, V. P.; Kanatzidis, M. G., The panoscopic approach to high performance thermoelectrics. *Energy Environ. Sci.* **2014,** *7* (1), 251-268.

12. Biswas, K.; He, J.; Blum, I. D.; Wu, C.-I.; Hogan, T. P.; Seidman, D. N.; Dravid, V. P.; Kanatzidis, M. G., High-performance bulk thermoelectrics with all-scale hierarchical architectures. *Nature* **2012,** *489*, 414.

13. Tan, G.; Shi, F.; Hao, S.; Zhao, L.-D.; Chi, H.; Zhang, X.; Uher, C.; Wolverton, C.; Dravid, V. P.; Kanatzidis, M. G., Non-equilibrium processing leads to record high thermoelectric figure of merit in PbTe–SrTe. *Nature*

Communications **2016,** *7*, 12167.

14. Yanling, P.; Gangjian, T.; Dan, F.; Lei, Z.; Qing, T.; Xiaobing, X.; Shengkai, G.; Yue, C.; Jing-Feng, L.; Jiaqing, H.; G., K. M.; Li-Dong, Z., Integrating Band Structure Engineering with All-Scale Hierarchical Structuring for High Thermoelectric Performance in PbTe System. *Adv. Energy Mater.* **2017,** *7* (3), 1601450.

15. Xiaojian, T.; Ling, W.; Hezhu, S.; Song, Y.; Jingtao, X.; Guoqiang, L.; Haochuan, J.; Jun, J., Improving Thermoelectric Performance of α-MgAgSb by Theoretical Band Engineering Design. *Adv. Energy Mater.* **2017,** *7* (18), 1700076.

16. Shi, X.; Yang, J.; Salvador, J. R.; Chi, M.; Cho, J. Y.; Wang, H.; Bai, S.; Yang, J.; Zhang, W.; Chen, L., Multiple-Filled Skutterudites: High Thermoelectric Figure of Merit through Separately Optimizing Electrical and Thermal Transports. *Journal of the American Chemical Society* **2011,** *133* (20), 7837-7846.

17. Tang, Y.; Gibbs, Z. M.; Agapito, L. A.; Li, G.; Kim, H.-S.; Nardelli, Marco B.; Curtarolo, S.; Snyder, G. J., Convergence of multi-valley bands as the electronic origin of high thermoelectric performance in $CoSb_3$ skutterudites. *Nature Materials* **2015,** *14*, 1223.

18. Fu, C.; Bai, S.; Liu, Y.; Tang, Y.; Chen, L.; Zhao, X.; Zhu, T., Realizing high figure of merit in heavy-band p-type half-Heusler thermoelectric materials. *Nat. Commun.* **2015,** *6*, 8144.

19. Zhang, J.; Song, L.; Pedersen, S. H.; Yin, H.; Hung, L. T.; Iversen, B. B., Discovery of high-performance low-cost n-type Mg_3Sb_2-based thermoelectric materials with multi-valley conduction bands. *Nat. Commun.* **2017,** *8*, 13901.

20. Basu, R.; Bhattacharya, S.; Bhatt, R.; Roy, M.; Ahmad, S.; Singh, A.; Navaneethan, M.; Hayakawa, Y.; Aswal, D. K.; Gupta, S. K., Improved thermoelectric performance of hot pressed nanostructured n-type SiGe bulk alloys. *J. Mater. Chem. A* **2014,** *2* (19), 6922-6930.

21. Girard, S. N.; He, J.; Zhou, X.; Shoemaker, D.; Jaworski, C. M.; Uher, C.; Dravid, V. P.; Heremans, J. P.; Kanatzidis, M. G., High Performance Na-doped PbTe–PbS Thermoelectric Materials: Electronic Density of States Modification and Shape-Controlled Nanostructures. *J. Am. Chem. Soc.* **2011,** *133* (41), 16588-16597.

22. Korkosz, R. J.; Chasapis, T. C.; Lo, S.-h.; Doak, J. W.; Kim, Y. J.; Wu, C.-I.; Hatzikraniotis, E.; Hogan, T. P.; Seidman, D. N.; Wolverton, C.; Dravid, V. P.; Kanatzidis, M. G., High ZT in p-Type $(PbTe)_{1-2x}(PbSe)_x(PbS)_x$ Thermoelectric Materials. *J. Am. Chem. Soc.* **2014,** *136* (8), 3225-3237.

23. Min, H.; Zhi-Gang, C.; Lei, Y.; Yi-Chao, Z.; S., D. M.; Hao, W.; Jin, Z., Realizing zT of 2.3 in $Ge_{1-x-y}Sb_xIn_yTe$ via Reducing the Phase-Transition Temperature and Introducing Resonant Energy Doping. *Adv. Mater.* **2018,** *30* (11), 1705942.

24. Zhao, L.-D.; Tan, G.; Hao, S.; He, J.; Pei, Y.; Chi, H.; Wang, H.;

Gong, S.; Xu, H.; Dravid, V. P.; Uher, C.; Snyder, G. J.; Wolverton, C.; Kanatzidis, M. G., Ultrahigh power factor and thermoelectric performance in hole-doped single-crystal SnSe. *Science* **2016,** *351* (6269), 141-144.

25. Zhao, L.-D.; Lo, S.-H.; Zhang, Y.; Sun, H.; Tan, G.; Uher, C.; Wolverton, C.; Dravid, V. P.; Kanatzidis, M. G., Ultralow thermal conductivity and high thermoelectric figure of merit in SnSe crystals. *Nature* **2014,** *508* (7496), 373-377.

26. Duong, A. T.; Nguyen, V. Q.; Duvjir, G.; Duong, V. T.; Kwon, S.; Song, J. Y.; Lee, J. K.; Lee, J. E.; Park, S.; Min, T.; Lee, J.; Kim, J.; Cho, S., Achieving ZT=2.2 with Bi-doped n-type SnSe single crystals. *Nat. Commun.* **2016,** *7*, 13713.

27. Olvera, A. A.; Moroz, N. A.; Sahoo, P.; Ren, P.; Bailey, T. P.; Page, A. A.; Uher, C.; Poudeu, P. F. P., Partial indium solubility induces chemical stability and colossal thermoelectric figure of merit in Cu_2Se. *Energy & Environmental Science* **2017,** *10* (7), 1668-1676.

28. Chang, C.; Wu, M.; He, D.; Pei, Y.; Wu, C.-F.; Wu, X.; Yu, H.; Zhu, F.; Wang, K.; Chen, Y.; Huang, L.; Li, J.-F.; He, J.; Zhao, L.-D., 3D charge and 2D phonon transports leading to high out-of-plane ZT in n-type SnSe crystals. *Science* **2018,** *360* (6390), 778-783.

29. Wu, D.; Wu, L.; He, D.; Zhao, L.-D.; Li, W.; Wu, M.; Jin, M.; Xu, J.; Jiang, J.; Huang, L.; Zhu, Y.; Kanatzidis, M. G.; He, J., Direct

observation of vast off-stoichiometric defects in single crystalline SnSe. *Nano Energy* **2017,** *35*, 321-330.

30. Zhao, L.-D.; Chang, C.; Tan, G.; Kanatzidis, M. G., SnSe: a remarkable new thermoelectric material. *Energy & Environmental Science* **2016,** *9* (10), 3044-3060.

31. PRL 2008, 055502Singh, Abhishek Kumar; Janotti, A.; Scheffler, M.; Van de Walle, C. G., Sources of Electrical Conductivity in SnO_2. *Phys. Rev. Lett.* **2008,** *101* (5), 055502.

32. Wang, J.-J.; Lv, A.-F.; Wang, Y.-Q.; Cui, B.; Yan, H.-J.; Hu, J.-S.; Hu, W.-P.; Guo, Y.-G.; Wan, L.-J., Integrated Prototype Nanodevices via SnO_2 Nanoparticles Decorated SnSe Nanosheets. *Scientific Reports* **2013,** *3*, 2613.

33. Ogo, Y.; Hiramatsu, H.; Nomura, K.; Yanagi, H.; Kamiya, T.; Hirano, M.; Hosono, H., p-channel thin-film transistor using p-type oxide semiconductor, SnO. *Appl. Phys. Lett.* **2008,** *93* (3), 032113.

Chapter 5. Revealing and removing the origin of surface SnO_x: Uncovering intrinsic charge and thermal transport properties of SnSe

5.1 Introduction

A thermoelectric (TE) power generator is an electronic heat convertor to generate electricity. It consists of p- and n-type TE semiconductors, connected electrically in series, without mechanically moving components. [1] A temperature gradient across them spontaneously induces an electric potential difference driven by charge carriers moving with heat. TE technology has been regarded as an environmentally friendly solution to recovering enormous amount of waste heat, which amount to more than 60% of the globally produced energy. Its extensive applications, however, have been restricted by low efficiency of TE materials.[2]

The efficiency of thermoelectric materials and devices is estimated by the figure of merit $ZT = S^2\sigma T/\kappa_{tot}$, where S is the Seebeck coefficient, σ is the electrical conductivity, T is the absolute temperature, and κ_{tot} is the total thermal conductivity from the electrical (κ_{ele}) and lattice vibration contribution (κ_{lat}).

The ZT values have been significantly increased by developing various performance enhancing strategies for increasing power factor (the product $S^2\sigma$) or suppressing lattice thermal conductivity in the past decade. They have been individually or multiply applied to representative thermoelectric systems such as lead chalcogenides, skutterudites, and half-heusler compounds. For example,

remarkably high ZT ~2.2-2.5 around 920 K was attained in PbTe-SrTe systems by introducing the multiple strategies of band engineering, endotaxial nanostructures, and hierarchical architecture, nonequilibrium processing.[3] Among the state-of-the-art thermoelectric systems, the most surprising achievement would be the discovery of the new thermoelectric material, tin selenide (SnSe), comprising nontoxic and Earth's-crust-abundant elements. Remarkably, this material contains highly effective phonon scattering mechanisms inherently in the crystal structure. Namely, strongly anisotropic and anharmonic crystal chemistry gives rise to intrinsic ultralow κ_{lat} of ~0.20 W/mK. As a result, its p-type pristine crystals exhibit the ZT of 2.6 at 913 K along the *b* axis, and the Br-doped n-type crystals show the ZT of 2.8 at 773 K along the *a* axis.[4,5]

However, these extraordinarily high thermoelectric properties have been only observable in properly prepared and handled single crystal samples. Contrary to the general understanding, many research groups observed much higher κ_{lat} values in polycrystalline SnSe samples than those reported for the single crystal samples despite the presence of additional phonon scattering mechanism at grain boundaries. Accordingly, ZT values of the polycrystalline SnSe materials have been much lower than those of the single crystals.[6] This has led to the serious controversy on if the ultralow κ_{lat} of SnSe is intrinsic property and such exceptional ZT values reported for single crystal SnSe can be achieved in polycrystalline SnSe samples. Indeed, polycrystalline samples are definitely suitable form for mass production and

commercial applications of thermoelectric power generation, given the high cost, lengthy and labor-intensive production, and mechanical brittleness of typical single crystal samples. Consequently, it has been the utmost task to realize comparable or even higher thermoelectric performance in polycrystalline SnSe samples.

Recently, we revealed that this apparently higher κ_{lat} is attributed to surface tin oxides on SnSe powders, which is detected by scanning transmission electron microscopy and X-ray photoemission spectroscopy. SnO_2, thermodynamically more stable than SnO at high temperature, shows approximately 140 times higher κ_{lat} than SnSe.[7] If SnSe powers covered with tin oxide thin films were compacted into dense pellets, high thermal conductivity tin oxides are present at grain boundaries. In this case, thermal conductivity can be rather boosted at grain boundaries in contrary to the general expectation, than scattering heat carrying phonons. Surface tin oxides can also serve as scattering centers for charge carriers, thereby affecting both thermal and charge transport performances adversely. Previously, we have developed a combined post-process of ball milling and chemical reduction for powders of SnSe-based materials, efficiently removing the tin oxide layers on them and revealing exceptionally low κ_{lat} of ~0.11 W/mK and near-single crystal ZT of 2.5 at 773 K. However, this post-H_2-reduced sample still shows higher κ_{lat} in the nearly entire temperature range from 300 to ~700 K than the single crystal SnSe. More critically, the origin of forming such tin oxides has been mysterious because all procedures have been strictly performed in 99.99% purity argon-filled glovebox, where the level

of oxygen kept less than 1 ppm.

Here, we report that Sn starting reagent, despite its 99.999% purity, is the origin of the surface tin oxides present in polycrystalline SnSe-based materials. Their presence obscures their intrinsic thermal and charge carrier transport properties. As a result, their true thermoelectric properties have not been truly observed in polycrystalline samples. To maximally avoid the formation of tin oxides, we develop a facile two-step oxygen/tin oxides removal strategy process.

5.2 Experimental section

Reagents. The following starting reagents were used as received unless noted otherwise: Se shot (99.999%, 5N Plus, Canada) and Na piece (99.9%, Sigma-Aldrich, USA). As-received Sn chunk (99.999%, American Elements, USA) was used to synthesize 'untreated' SnSe-based materials as control samples. It was purified by our melting-purification process as described below to eliminate surface tin oxides, and was used to synthesize 'purified' SnSe-based materials.

Purification of Sn. As-received Sn chunks were apparently silvery. They were placed on a graphite sheet pre-washed with ethanol, and were heated at 473 K, which is near the melting point of Sn at ~505 K, for 6h under a 4% H_2/96% Ar with a flow rate of 200 mL min^{-1}. A change in their surface color and luster was not visible. The

resulting Sn chunks were loaded into a carbon-coated and evacuated fused-silica tube (~10^{-4} Torr). The tube was heated at 1273 K for 6 h, followed by cooling to room temperature. Ash-like black residues formed at the top and surface of the Sn ingot. They were identified as tin oxides by Fourier transformed far-infrared absorption spectroscopy. They were scraped out of the Sn ingot. The same melting-purification process was repeated three times at 873–723 K until the black residues were not visibly observed any more.

Synthesis. Purified and untreated materials with the nominal compositions $Na_xSn_{0.995-x}Se$ (x = 0.01-0.03) and SnSe as a reference were synthesized by reacting stoichiometric mixtures of proper starting reagents. They were loaded in carbon-coated and evacuated fused-silica tubes (~10^{-4} Torr), and were heated at 1223 K for 12 h, followed by quenching to ice water. The obtained ingots were further annealed at 773 K for 48 h and were cooled naturally to room temperature. The weight of typical ingots was approximately 13g. They were pulverized by hand-grinding, sieved to 2.5 mm, and were subsequently purified at 613 K for 6 h under a 4% H_2/96% Ar with a flow rate of 200 mL min^{-1}.

Compacting powders. The resulting powders were loaded in a BN-coated graphite die and were cold-pressed manually in an Ar-filled glovebox. When the die was

transferred to a spark plasma sintering (SPS) system (SPS-211Lx, Fuji Electronic Industrial Co., Japan), an Ar flow (99.99% purity) was applied to it continuously to avoid possible oxidation. Powder samples in the die were densified at ~ 783 K for 5 min under an axial pressure of 50 MPa in a vacuum of ~ 1.4×10^{-2} Torr using SPS. All SPS-processed samples show relative densities of ~96 %.

Powder X-ray diffraction (XRD). XRD analysis was performed on a SmartLab Rigaku X-ray diffractometer with Cu Kα (λ = 1.5418 Å) graphite-monochromatized radiation operating at 40 kV and 30 mA at room temperature.

Time-of-flight secondary ion mass spectroscopy (TOF-SIMS). TOF-SIMS experiments were carried out on a Physical Electronics TRIFT III spectrometer. The SPS processed samples were polished with Buehler Ecomet III Tabletop Polisher/Grinder to prepare a smooth surface. Subsequently, they were sputtered with 5 keV Ar ion beam for 5 min in SIMS chamber to expose the grain boundary. During this process, omnipresent H_2O even in an ultrahigh vacuum chamber was ionized to give H^+, which then attached to surface tin oxides to form $SnOH^+$. Accordingly, to examine the distribution of surface tin oxides, the $SnOH^+$ ion mapping images were collected for 10 min. The primary ion source of SIMS is gallium beam with 25 keV energy. The measurements were conducted in NUANCE-Keck-II center of Northwestern University.

Hall measurements. The Hall coefficients (R_H) were obtained by the Van der Pauw method on a Lake Shore HMS8407 Hall effect measurement system in a magnetic field of 1.5 T and 3 mA excitation current. The hole carrier concentration (n_H) and hole mobility (μ_H) were accessed by the formulae, $n_H = 1/(e \cdot R_H)$ and $\mu_H = R_H \cdot \sigma$, respectively.

Electrical and thermal transport property measurements. The obtained SPS-processed pellets were cut and polished into a rectangular shape with a length of 13 mm and thickness of ~ 2 mm under a N_2 atmosphere (99.99% purity). The electrical conductivity and Seebeck coefficient were measured simultaneously under an Ar atmosphere from room temperature to 823 K using a Netzsch SBA 458 Nemesis system. A Netzsch LFA 457 MicroFlash instrument was used to record the thermal diffusivity of the samples coated with graphite. The typical samples are disk shape with a diameter of 8 mm and thickness ranging from 1 to 2 mm. The thermal conductivity was calculated from the formula $\kappa_{tot} = D \cdot C_p \cdot \rho$, where D is the thermal diffusivity, C_p is the heat capacity, and ρ is the mass density of the specimens. The temperature-dependent C_p value were derived from the previous study[5]. The ρ value used was obtained by their geometrical dimensions and masses, which is nearly the same as that by the Archimedes method. The density values used are given in Table S1. The total thermal conductivity κ_{tot} is the sum of the lattice (κ_{lat}) and electronic thermal (κ_{ele}) conductivities. κ_{ele} is proportional to the electrical conductivity (σ) according to the Wiedemann−Franz relation ($\kappa_{ele} = L \cdot \sigma \cdot T$), where L is the

temperature-dependent Lorenz number and T is the absolute temperature. An L value with respect to temperature were obtained from the previous study[5]. The κ_{lat} value was calculated by subtracting the κ_{ele} value from the κ_{tot} value by the relation $\kappa_{lat} = \kappa_{tot} - \kappa_{ele}$.

Calculations for formation energy of oxygen impurity and phase stability. The formation energies of oxygen impurities were calculated using an octuple super cell of SnSe. The lattice parameter of pristine SnSe were fully relxed to be a = 11.49 Å, b = 4.12 Å, and c = 4.53 Å, while the internal coordinate of three possible configurations of oxygen impurities such as including O replacing Sn (O_{Sn}), O replacing Se (O_{Se}), and O at interstitial sites in the SnSe crystal lattice (O_{Int}) were optimized within the fixed lattice constant of pristine SnSe by density functional theory (DFT) calculations. Plane wave basis set with 350 eV cut off energy and the projector augmented wave method[8] were utilized to describe wavefunctions and potentials. For the accurate description of exchange correlation functional and van der Waals interaction, we employed SCAN+rVV10 functional[9] which is implemented in Vienna Ab initio Simulation Package[10,11]. Formation energies of each configuration were calculated with the following formula:

$$\Delta H_{D,q}(E_F,\mu)=\left[E_{D,q} - E_H\right]+q(E_V+\Delta E_F)+\sum_\alpha n_\alpha\left(\mu_\alpha^0+\Delta\mu_\alpha\right)+\varepsilon_{corr}$$

The first term of right-hand side of the equation is the total energy difference between defected system with charge q and pristine host material. The second and third terms

stand for the free energy gain (or loss) from Fermi energy and chemical potential, respectively, where E_V is the highest energy level of occupied states of electron, ΔE_F is the Fermi level referenced to E_V, n_α is the number of atom when α is removed (+1, +2, ..) or added (–1, –2, …) to host system upon the defect formation, μ_α^0 is the total energy of reference phase of α, and $\Delta\mu_\alpha$ is the relative chemical potential α that varies with synthesis condition. The last term is a correction term including finite cell corrections[12]. Extended Data Fig. 3a presents the formation energy of three different configurations of oxygen impurities in SnSe as a function of Fermi level under the oxygen-rich condition. The set of corresponding chemical potentials is determined by free energies of competing phases consisting of Sn, Se, and O, which results in the phase stability map shown in Extended Data Fig. 3c. From the calculated formation energies of oxygen impurities, the concentration of oxygen which can be soluble into the lattice is evaluated as shown in Extended Data Fig. 3b.

Calculations for phonon band structure and Grüneisen parameters. Phonon band structure and Grüneisen parameters were calculated within quasi-harmonic approximation based on DFT calculations. They have been calculated for pristine SnSe previously[13]. In this work, we further calculated them for the optimally hole-doped system, namely, $Na_{0.03}Sn_{0.97}Se$. To obtain accurate force constant matrix, we employed a 2×2×2 supercell for $Na_{0.03}Sn_{0.97}Se$ with 64 atoms, and accordingly the supercell accommodates 512 atoms in total. For better comparison, we also

considered the same size of supercell for pristine SnSe. DFT force calculations were performed with plane wave set of 350 eV energy cutoff, gamma point *k*-space sampling, and PBEsol exchange functional[14], and they were forced to converge until the largest component of atomic force becomes smaller than 10^{-8} eV Å^{-1}. To evaluate the Grüneisen parameters defined by the relation $\gamma_i = -\frac{V}{\omega_i}\frac{\partial \omega_i}{\partial V}$, where V is the volume of unit cell and ω_i is frequency of *i*-th phonon mode, we considered three sets of phonon dispersion relation with different volumes, namely, 0.99, 1.00, and 1.01 times of the optimized volume of the unit cell.

Calculations for electronic band structure. To understand the enhanced Seebeck coefficient by Na doping, we obtained electronic band structures for hole-doped $Na_{0.03}Sn_{0.97}Se$ and pristine SnSe using DFT calculations with plane wave basis set with 350 eV energy cut off, 4×4×4 *k*-space sampling, and SCAN+rVV10 functional[9]. We used a $2\sqrt{2}\times2\sqrt{2}\times1$ supercell, and the lattice parameters and internal coordinates were fully optimized. Upon Na doping, the lattice dimension decreases by about 0.5% along the *b*- and *c*-axes and increases by about 0.3% along the *a*-axis.

It should be noted that the recent investigation by angle-resolved photo emission spectroscopy (ARPES) for SnSe clearly shows the emergence of pudding mold-type bands near valence band maximum (VBM)[15] which is highly important to achieve high power factor within the band convergence strategy. However, many previous DFT studies for SnSe employing semi-local exchange-correlation

functional such as PBE could not reproduce band structures observed by the ARPES appropriately. In this work, we found that such band dispersions in SnSe seen by the ARPES experiments can be well reproduced by SCAN+rVV10 functional. Accordingly, we applied the same method to hole-doped $Na_{0.03}Sn_{0.97}Se$. We considered a 64 atoms-containing supercell for both SnSe and $Na_{0.03}Sn_{0.97}Se$. Band structures are evaluated along a high-symmetric line in *k*-space. For density of states (DOS), we employed denser *k*-grid mesh, which is a 10×10×10 regular mesh. Calculation results are given in Extended Data Fig. 12.

Calculations for Lorenz number. The Lorenz number, *L*, was evaluated with two different schemes: 1) Kane band model and 2) Boltzmann transport equation (BTE) with DFT band structures as follows.

1) Calculation by a multivalley Kane band model

To consider multivalley effects, we calculated the Lorenz number as follows:

$$L=\frac{L_1\sigma_1+L_2\sigma_2}{\sigma_1+\sigma_2}$$

where $L_{1,2}$ and $\sigma_{1,2}$ are the Lorenz number and conductivity of the first and the second band maxima (VBM_1 and VBM_2), respectively. They are expressed by the following equations, respectively:

$$L_i = \left(\frac{k_B}{e}\right)\left\{\frac{{}^{2}F_{-2}^{1}(\eta_i,\alpha_i)}{{}^{0}F_{-2}^{1}(\eta_i,\alpha_i)} - \left(\frac{{}^{1}F_{-2}^{1}(\eta_i,\alpha_i)}{{}^{0}F_{-2}^{1}(\eta_i,\alpha_i)}\right)^2\right\}$$

$$\sigma_i = q\,\mu_i\;\; n_i$$

where q is the charge of the carrier, μ_i is the mobility, and n_i is the carrier concentration as given by the following equations:

$$n_i = \frac{1}{3\pi^2}\left(\frac{2m_{d,i}^{*}k_BT}{h^2}\right)^{\frac{3}{2}}\;{}^{0}F_{0}^{\frac{3}{2}}(\eta_i,\alpha_i)$$

$$\mu_i = \frac{2\pi h^4 eC_l}{m_{l,i}^{*}\left(2m_{d,i}^{*}k_BT\right)^{\frac{3}{2}}E_{def}^{2}}\,\frac{3\;{}^{0}F_{-2}^{1}(\eta_i,\alpha_i)}{{}^{0}F_{0}^{\frac{3}{2}}(\eta_i,\alpha_i)}$$

In the equations above, the effective mass of each band was calculated by the following equations:

$$m_{d,i}^{*}=\sqrt[3]{m_{x,i}^{*}m_{y,i}^{*}m_{z,i}^{*}}(N)^{\frac{2}{3}}$$

$$m_{l,i}^{*}=\frac{1}{3}\left(\frac{1}{m_{x,i}^{*}}+\frac{1}{m_{y,i}^{*}}+\frac{1}{m_{z,i}^{*}}\right)^{-1}$$

where N is a degeneracy of bands, which is 2 here. ${}^{n}F_{m}^{k}$ is the generalized Fermi function which is defined by the following equation:

$${}^{n}F_{m}^{k}(\eta,\alpha)=\int_{0}^{\infty}d\varepsilon\left(-\frac{df(\varepsilon-\eta)}{d\varepsilon}\right)\varepsilon^{n}\left(\varepsilon+\alpha\varepsilon^{2}\right)^{k}\left[(1+2\alpha\varepsilon)^{2}+2\right]^{\frac{m}{2}}$$

where η is the reduced Fermi level: $\eta_1=\frac{E_f}{k_BT}$ and $\eta_2=\eta_1-\frac{\Delta E}{k_BT}$ for the VBM_1 and VBM_2, respectively. The non-parabolicity parameter α is given by $\alpha_1=\frac{k_BT}{E_g}$ and $\alpha_2=\frac{k_BT}{E_g+\Delta E}$ for the VBM_1 and VBM_2, respectively, where T is the absolute temperature, k_B is the Boltzmann constant, C_l is a parameter determined by the longitudinal speed of sound υ_l and the atomic density d, and E_{def} is a combination of deformation potentials for multivalley systems, which describes the carrier scattering strength by acoustic phonons. Detailed parameters for each band are

obtained from the previous work[5] as listed in the following Table:

	1st band	2nd band
$m^*_{x,i}$	0.76	2.49
$m^*_{y,i}$	0.33	0.18
$m^*_{z,i}$	0.14	0.19

In this work, we first evaluated η for given carrier concentrations and temperatures. Then, we further calculated σ_i and L_i. Carrier concentration was varied from 4.0 $\times$ 10^{18} to 4.0 $\times$ 10^{19} cm^{-3}. We set E_g at 0.65 eV and ΔE is 0.06 eV for undoped SnSe system according to the previous report.[1] For Na-doped system, only ΔE is changed to 0.00 eV given the VBM convergence by Na doping. Calculation results are presented in Extended Data Fig. 12c.

2) Calculation by BTE with DFT electronic band structures

Utilizing BoltzTra2 code[16] and our DFT electronic band structures, we calculated Lorenz number. In this scheme, electrical conductivity (σ) and electric thermal conductivity (κ_{el}) are expressed as follows:

$$\sigma = L^{(1)}$$

$$\kappa_{el} = \frac{1}{q^2 T}\left[\frac{\left(L^{(1)}\right)^2}{L^{(0)}} - L^{(2)}\right]$$

$$L^{(\alpha)}(\mu,T)=q^2\int\sigma(\varepsilon,T)(\varepsilon\text{-}\mu)^{\alpha}\left(-\frac{df^0(\varepsilon;\mu,T)}{d\varepsilon}\right)$$

where $\sigma(\varepsilon, T)$ is the transport distribution function. Then, the Lorenz number is calculated by the following equation:

$$L=\frac{\kappa_{el}}{\sigma T}$$

In this calculation, we first calculated μ for given carrier concentrations and temperatures. Then, we evaluated the remaining quantities to obtain *L*. In these results, we note that the deviation in *L* along the *a* axis for undoped and Na-doped systems becomes greater at higher temperatures. Because we only employed *Pnma* structure, which is the low temperature phase of SnSe, for the band structure calculations, such behavior possibly deviates from the correct value. Compared to the results by a Kane model, those by BTE with the full DFT electronic structure show a larger difference in the *L* because it reflects further changes in the electronic structure by Na-doping. However, the corresponding difference less than 10% is trivial.

5.3 Results and discussion

First, as-received elemental tin (Sn) reagent must be purified before the use for synthesis of SnSe-based materials. Note that we use 99.999% purity Sn chunk, showing a characteristic silvery luster. It is chemically reduced by a 4% H_2/Ar flow at 473 K for 6 h, near the melting point of Sn, showing no visible change in the surface color and luster. It is subsequently heated at 1223 K for 6 h in a carbon-coated and evacuated fused silica tube (~10^{-4} Torr). Surprisingly, ash-like black residues form at the upper surface of the resulting Sn ingot, which is identified as tin oxides by Fourier-transformed far-infrared spectroscopy (Figures 5.1 and 5.2). After scraping tin oxide residues out, the same melting purification process is repeated two more times at 873 and 723 K, respectively, until their presence is not visibly observed any more. We find that the purification of elemental selenium (Se) reagent has a negligible influence on thermoelectric properties of SnSe-based materials. The purified Sn reagent is used to synthesize polycrystalline SnSe-based materials. Second, the synthesized powder samples are pulverized and further purified under a 4% H_2/96% Ar flow at 613 K for 6h. Samples prepared by this two-step purification process is designated as 'purified' in this letter. Those without this process is denoted as 'untreated'. All polycrystalline samples were densified into pellets by spark plasma sintering (SPS) for thermoelectric property measurements. It is an argon atmosphere (99.99%) in which all experimental procedures were strictly performed unless noted otherwise.

To investigate the effect of our purification process and probe the presence of oxygen in the SnSe samples, we performed time of flight ion mass spectroscopy (TOF-SIMS). It should be noted that oxygen is ubiquitous even in an ultrahigh vacuum. Due to the high ionization yield of oxygen atom, it contributes to the majority of the *m*/*z* 16 counts. As a result, oxygen ion mapping cannot reflect the oxygen distribution in SnSe samples accurately. Instead, we sputtered the specimen surface to generate $SnOH^+$, which corresponds to SnO attached with H^+. The $SnOH^+$ mapping can reliably scan the oxygen distribution bound on Sn. The $SnOH^+$ images from the untreated (Figure 5.3a) and purified SnSe samples (Figure 5.3c) show that the former contains the 7.4 times higher concentration of tin oxides than the latter. Importantly, tin oxides are more abundant in the grain boundary (indicated by white dotted lines) than the interior regions in both the samples (Figure 5.3b and 5.3d). This observation verifies that a significant amount of tin oxides exists at grain boundaries in polycrystalline SnSe-based materials and that our purification process can effectively remove them. Grain boundary tin oxides are plausibly brought by SPS process of SnSe powders of which surface is covered with tin oxide thin film.

The computational study based on density functional theory (DFT) strongly supports the observation upon the formation of surface tin oxides. If oxygen is introduced to SnSe, three possible defects can be considered in the SnSe lattice: O replacing Sn (O_{Sn}), O replacing Se (O_{Se}), and O at interstitial sites (O_{Int}). The

formation energy of these defects is calculated to be larger than 1.0 eV (Figure 5.4a) under the oxygen-rich condition (indicated by a red dot in the chemical potential map in Fig. 5.4c). This result indicates that the maximum concentration of oxygen impurity present in the SnSe lattice cannot exceed 10^{14} cm^3 in the temperature range of 300 – 800 K (Figure 5.4b). As a result, even a trace of oxygen present in starting reagents and sample preparation processes can be precipitated as tin oxides on the surface of SnSe powders, rather than incorporating into the SnSe lattice. Figure 5.4c presents the phase stability map of SnSe phase and competitors as a function of chemical potentials. When the oxygen chemical potential ($\Delta\mu_O$) is small enough (<-3.33 eV), SnSe can exist solely. However, $\Delta\mu_O$ becomes larger than -3.33 eV, tin oxides are precipitated first, and then other competitors follows. These calculation results agree with the observation of a high degree of tin oxides at grain boundaries in untreated polycrystalline SnSe samples.

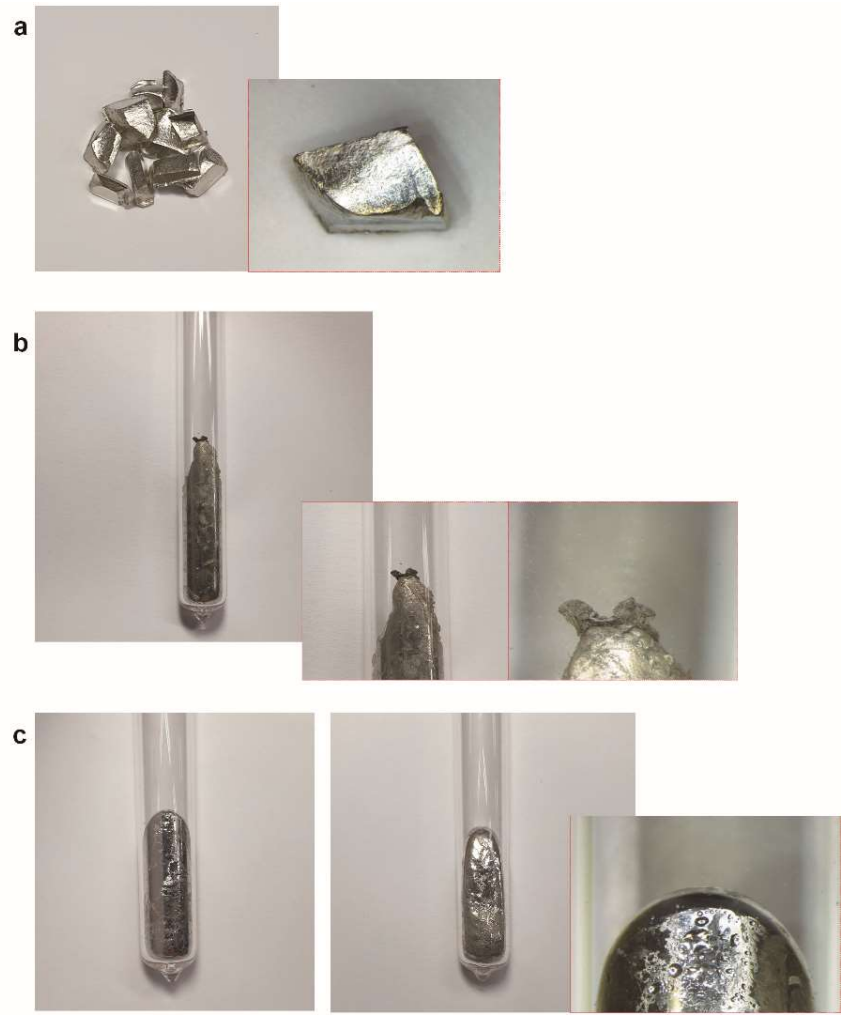

Figure 5.1. a, As-received Sn chunks. **b,** Typical images of Sn ingot after H_2-chemical reduction and subsequent melting-purification at 1273 K for 6 h. It is clearly observed that ash-like black residues formed on the top and whole surface of Sn ingot. **c**, After the repetition of the melting-purification process three times, the black residues were invisible any more.

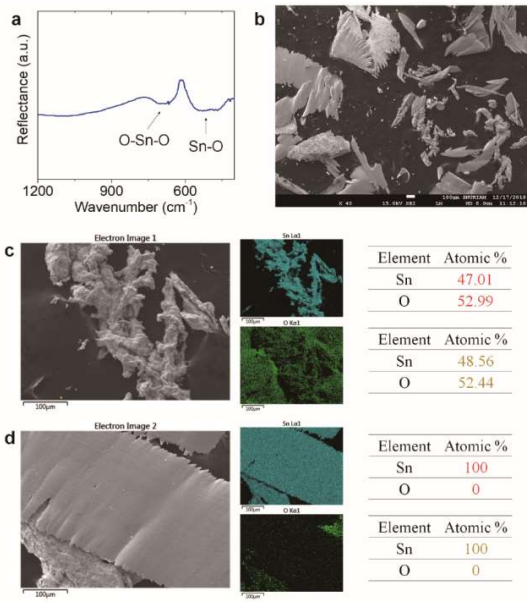

Figure 5.2. Spectroscopic and elemental analysis on the ask-like black residues. The black residues were carefully scraped from the top and surface of the Sn ingot after the first melting-purification process. **a**, Fourier-transformed far-infrared spectrum of the ash-like black residues. The peaks in the spectrum arise from the presence of Sn-O bonds. The bands around 480 cm^{-1} and 540 cm^{-1} are attributed to asymmetric and symmetric stretching vibration of O-Sn-O, respectively. The band at 680 cm^{-1} can be assigned to the asymmetric Sn-O-Sn stretching mode. **b**, Scanning electron microscopy (SEM) image of the ash-like black residues with the slices of Sn, which were scraped from Sn ingot. **c**, SEM image, EDS elemental mapping, and composition analysis of the ash-like black residues, confirming they are SnO_x. **d**, SEM image, EDS elemental mapping, and composition analysis of Sn slices, confirming the negligible concentration of SnO_x in the purified Sn ingot.

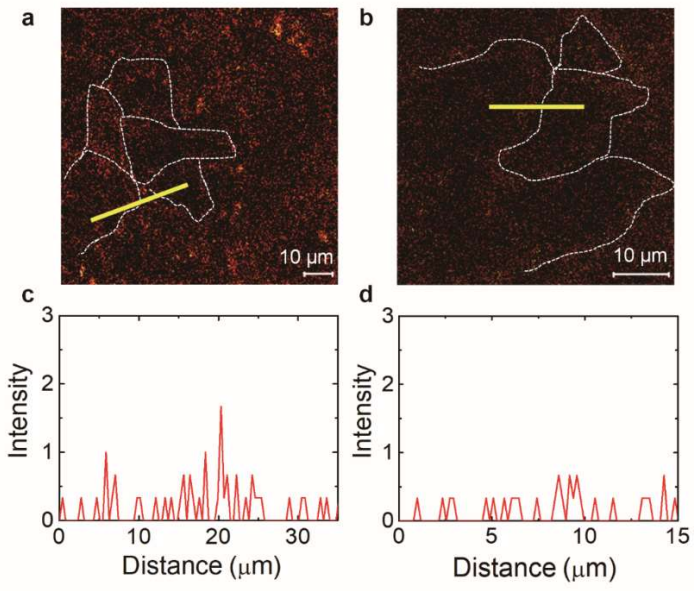

Figure 5.3. Distribution of tin oxides (SnO_x) in 'untreated' and 'purified' polycrystalline SnSe samples by the time-of-flight secondary ion mass spectroscopy (TOF-SIMS).

The surface of both SPS processed specimens was sputtered to generate $SnOH^+$ complex which is relevant quantity to tin-bound oxygen. Accordingly, $SnOH^+$ map clearly represents the distribution of surface SnO_x on SnSe samples. **a,** The $SnOH^+$ image for the untreated SnSe sample. **b,** The $SnOH^+$ image for the 'purified' SnSe sample. The red spots correspond to SnO_x. The white dotted lines indicate grain boundaries, which were defined with optical images taken on the corresponding regions. The scale bar is given. **c,** The concentration of SnO_x across the grain boundary by a line profile (yellow solid line in **a)** for the untreated SnSe sample. **d,** The concentration of SnO_x across the grain boundary by a line profile (yellow solid

line in **b)** for the purified SnSe sample. The width of a line profile is 3 μm, in which the concentrations of SnO_x were averaged. The substantial decrease in surface SnO_x is clearly observed by our purification process.

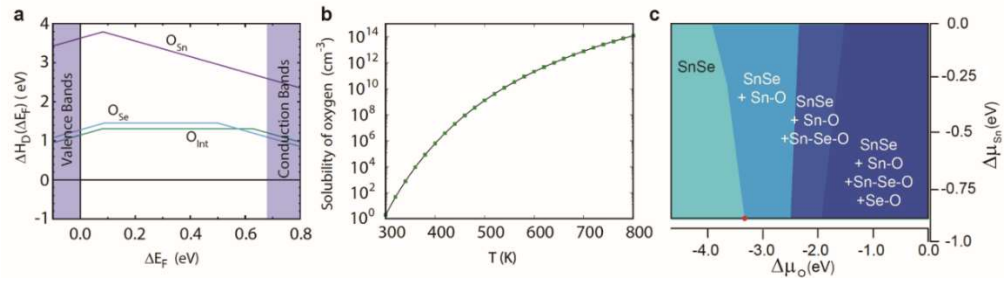

Figure 5.4. The density functional theory calculations for the formation of surface tin oxides. a, The diagram of calculated defect formation energy (ΔH_D) as a function of Fermi energy (ΔE_F) for three possible defects: oxygen replacing tin (O_{Sn}), oxygen replacing selenium (O_{Se}), and oxygen at interstitial sites in the SnSe lattice (O_{Int}). The energy level of the valence band maximum (VBM) is set to zero. The regions below VBM and above conduction band minimum are depicted in violet color. **b**, The calculated solubility of oxygen in the SnSe lattice in the temperature range of 300-800 K, showing that the maximum concentration of oxygen impurity present in the SnSe lattice cannot exceed 10^{14} cm^3. **c**, Phase stability map of SnSe and competitors with oxygen as a function of chemical potential for oxygen ($\Delta\mu_O$).

The effect of our two-step purification process is dramatically evident in thermal conductivity (κ) of polycrystalline SnSe-based materials. Because of the characteristic lamellar structure of SnSe (Figure 5.5), their thermoelectric properties are highly anisotropic. Namely, the polycrystalline and single crystal samples exhibit the lowest κ along the parallel to the consolidation direction (//) and along the crystallographic *a* axis, respectively. Accordingly, we compare κ for purified and untreated polycrystalline SnSe samples with the previously published value for the undoped single crystal sample along these directions.

The purification process markedly reduces the lattice thermal conductivity (κ_{lat}) for the polycrystalline SnSe sample, making it comparable to that reported for the single crystal SnSe sample along the *a* axis over the entire temperature range (Figure 5.6a). In contrast, when treated only by the post H_2-reduction without the elemental Sn purification process, the decrease in κ_{lat} is modest. The κ_{lat} for the untreated, H_2-reduced, and purified polycrystalline SnSe samples is ~1.03, 0.99, and 0.58 W/mK at 300 K and ~0.41, 0.38, and 0.24 W/mK at 773 K, respectively. This observation confirms the Sn purification is essential to unveil the intrinsically ultralow κ_{lat} in SnSe-based materials. Why the presence of a trace of tin oxides is so detrimental to SnSe thermoelectrics can be understood by comparing its κ_{lat} with that of representative thermoelectric systems SnTe and PbTe comprising a larger congener. The difference in the κ_{lat} before and after the purification process may be the contribution from tin oxides to κ_{lat} of SnSe. It is, respectively, ~0.45 and

0.17 W/mK at 300 and 773 K, and corresponds to approximately 77 and 71% of the κ_{lat} at 300 and 773 K for the purified SnSe sample. In contrast, the κ_{lat} of the untreated SnTe falls in the range 3.20 – 1.43 W/mK in 300 – 723 K temperature range. Consequently, the contribution from tin oxides, if present, to the κ_{lat} of SnTe should be modest. The κ_{lat} of the untreated PbTe decreases from 2.39 to 1.07 W/mK in 310 – 750 K temperature range. Consequently, the observation of ultralow κ_{lat} can be seriously obscured by even a tiny concentration of high κ_{lat} impurity as in the case of SnSe.

The $Na_xSn_{0.995-x}Se$ (x = 0.01, 0.02, and 0.03) samples exhibit even more suppressed κ_{lat} than the undoped SnSe, decreasing with the higher Na concentration (Figure 5.6b). The x = 0.03 sample shows lower κ_{lat} than the single crystal SnSe sample above 323 K. The lowest κ_{lat} is ~0.18 (x = 0.01), 0.14 (x = 0.02), and ~0.08 W/mK (x = 0.03) at 783 K, in comparison with ~0.20 W/mK for the single crystal SnSe along the *a* axis. The observed values are one of the lowest κ_{lat} to date among bulk crystalline solids. In comparison, bulk polycrystalline $CsAg_5Te_3$ exhibits ~0.18 W/mK at 727 K because the concerted rattling of ionized Ag groups considerably increases the Grüneisen parameters [17]. 62 nm-thick thin films of disordered lamellar WSe_2, prepared by the vacuum deposition method, gives ~0.05 W/mK at 300 K [18].

The electrical thermal conductivity (κ_{ele}) for $Na_xSn_{0.995-x}Se$ samples increases with the higher Na concentration over the entire temperature range, much higher than that for the polycrystalline and single crystal SnSe samples (Figure 5.7a).

For example, the κ_{ele} for the $Na_xSn_{0.995-x}Se$ samples at 773 K is ~0.075, 0.107, and 0.113 W/mK in comparison with 0.007 W/mK of the SnSe single crystal sample. Their κ_{ele} increases with the higher temperature above 673 K. As a result, total thermal conductivity (κ_{tot}) for the x = 0.03 becomes comparable to that for SnSe single crystal sample at the elevated temperatures, where the former shows much lower κ_{lat} than the former. Their κ_{tot} at 773 K is nearly the same at ~0.23 W/mK, slightly lower than ~0.26 W/mK for the purified SnSe (Figure 5.7b).

Our two-step purification process for polycrystalline SnSe-based materials ultimately reveals their intrinsically ultralow thermal conductivity with the excellent reproducibility. The purified specimens were prepared from the thirteen independent synthesis batches, and their ultralow κ_{tot} was cross-checked from two institutions of Seoul National University (SNU) and Northwestern University (NU) and the company of Netzsch instruments (Figure 5.8). Those specimens (7 from SNU, 3 from NU, and 3 from Netzsch) give the uncertainty in κ_{tot} less than ~9.7% in the temperature range from 323 to 773 K. It is only 6.2% 773 K. Note that the obtained uncertainty arises from both individual specimens and instruments from three independent inspection places. The uncertainty at 783 K is 6.3% from ten samples measured from SNU and NU, in which temperature range the instrument at Netzsch cannot operate. The average κ_{tot} at 773 and 783 K is ~0.25 and 0.24 W/mK, corroborating the reproducibility of intrinsically ultralow thermal conductivity in polycrystalline SnSe-based materials.

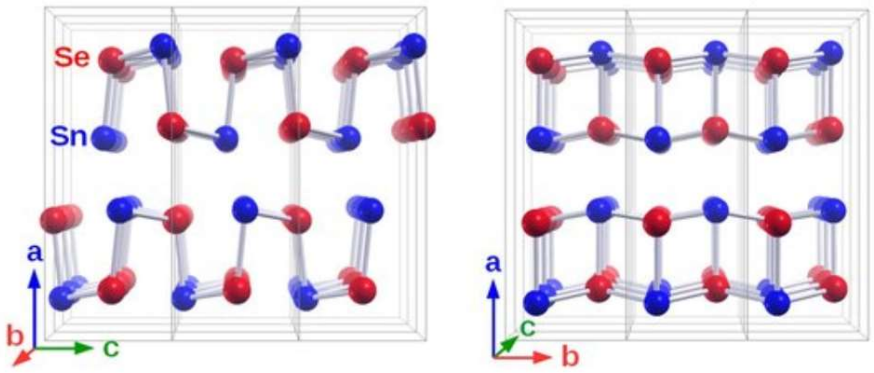

Figure 5.5. lamellar structure of SnSe along the *b*- and *c*-axes

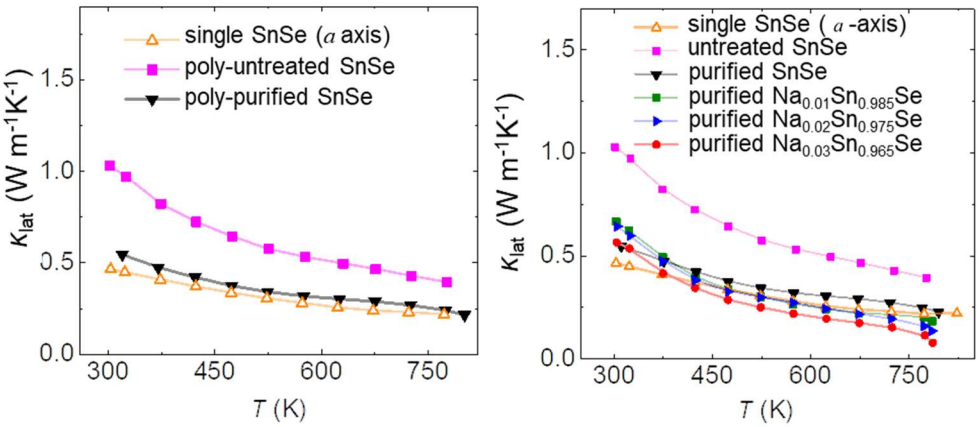

Figure 5.6. κ_{lat}, and total thermal conductivities, κ_{tot}, as a function of temperature for the undoped and Na-doped polycrystalline SnSe samples before and after the purification process. a, κ_{lat} for the untreated, H_2-reduced without Sn purification, and purified SnSe samples. **b,** κ_{lat} for the $Na_xSn_{0.995-x}Se$ (x = 0.01, 0.02, and 0.03) samples in comparison with that for the untreated and purified SnSe samples.

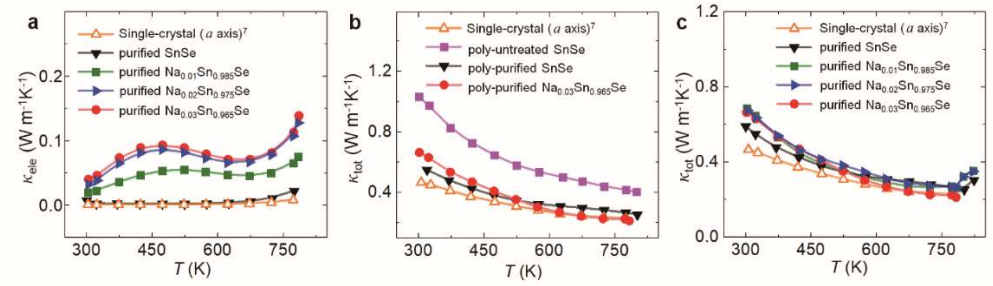

Figure 5.7. Thermal conductivities of the purified $Na_xSn_{0.995-x}Se$ and SnSe as a function of temperature. a, Electronic thermal conductivity, κ_{ele}. **b,** Comparison of total thermal conductivity, κ_{tot}, for the purified $Na_{0.03}Sn_{0.965}Se$ and untreated and purified SnSe. **c**, Comparison of κ_{tot} for purified $Na_xSn_{0.995-x}Se$ and SnSe. κ_{lat} and κ_{tot} for SnSe single-crystal along the *a* axis are given from the previous report for comparison. Data for polycrystalline samples were measured along the SPS direction. The untreated sample was synthesized using as-received starting Sn reagent. The purified samples were synthesized using starting Sn reagent treated by our purification process.

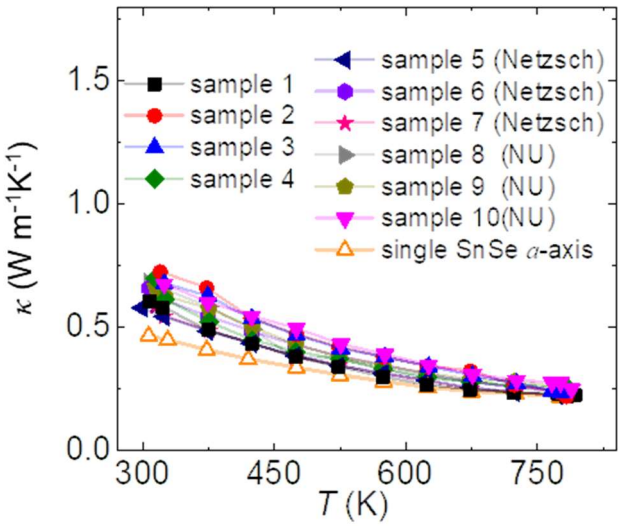

Figure 5.8. The reproducibility of κ_{tot} for ten independently synthesized samples, cross-checked at Seoul National University (samples 1-4), Netzsch instruments (Netzsch, samples 5-7), and Northwestern University (NU, samples 8-10). κ_{lat} and κ_{tot} for SnSe single-crystal along the *a* axis are given for comparison. Polycrystalline samples were measured parallel to the SPS direction.

The effect of the purification process is marginal on electrical conductivity (σ) for undoped polycrystalline SnSe samples, in contrast to the case of thermal conductivity (Figure 5.9a). This is ascribed to their too low Hall carrier concentration (n_H): ~2.52 $\times 10^{17}$ and 1.98 $\times 10^{17}$ cm^{-3} at 300 K for the untreated and purified polycrystalline SnSe, respectively. When applied to the properly doped $Na_xSn_{0.995-x}Se$ (x = 0.01, 0.02, and 0.03) system with the n_H at the level of 10^{19} cm^{-3}, the purification process substantially enhances σ over the full range of temperature (Figure 5.10a). Importantly, the σ is markedly improved in the temperature range 300 - 523 K by removing surface tin oxides, increasing with the higher Na content. This leads to the enhanced thermoelectric performance of the materials in the low to mid-range temperature regime. In fact, polycrystalline SnSe thermoelectrics has suffered from high electrical resistivity in that range, giving poor average ZT values. The x = 0.03 sample shows the σ of 140.15 and 117.96 S/cm at 423 and 783 K along the parallel to the SPS direction. It shows the even higher σ of 180.7 and 132.24 S/cm at 423 and 783 K along the perpendicular to the SPS direction.

The Seebeck coefficient (S) for the purified $Na_xSn_{0.995-x}Se$ samples increases monotonously up to 673 K and diminishes afterward (Figure 5.10b). It is nearly the same along the parallel and perpendicular to the SPS direction (Figure 5.11). In general, it slightly increases with the higher Na concentration for the $Na_xSn_{0.995-x}Se$ samples in contrast to the general trend of the inverse proportionality between σ and S. Their S is significantly enhanced by the purification process

involving chemical reduction process. For example, the maximum S for x = 0.03 sample +322 and 342 at 673 K before and after the purification process, respectively. The Na-doped samples show considerably smaller S values than the undoped SnSe sample because of the much higher n_H. The high reproducibility of σ and S values were confirmed using independently synthesized samples (Figure 5.12). Note that the S values slightly increases with the higher Na doping concentration, in contrast to the trend of the inverse proportionality between σ and S.

The simultaneously increased σ and S of the purified $Na_xSn_{0.995-x}Se$ samples results in the remarkably improved power factor (Figure 5.10c). Their power factors increase with the larger amount of Na doping. The improved σ in the low to mid-range temperature is directly reflected in the trend of power factors for the $Na_xSn_{0.995-x}Se$ samples. The x = 0.03 sample exhibits power factors near 9 μW/cmK^2 in the wide range of temperature from 473 to 783 K with a maximum of 9.62 μW/cmK^2 at 498 K along the parallel to the SPS direction. The maximum power factor is even higher at 12.06 μW/cmK^2 at 473 K along the perpendicular to the SPS direction, which is the highest value reported for polycrystalline SnSe-based materials.

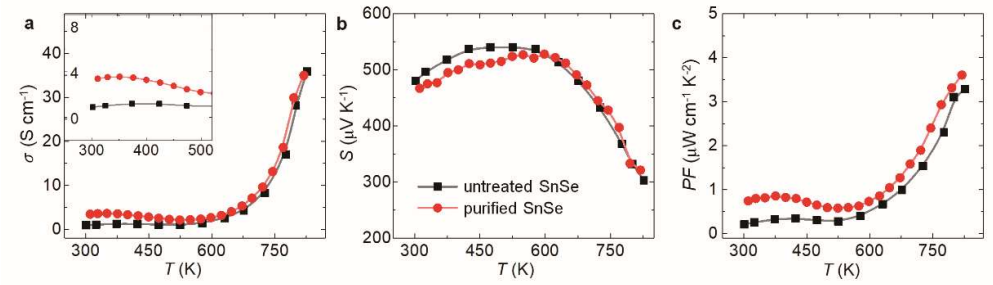

Figure 5.9. Charge transport properties as a function of temperature for polycrystalline SnSe before and after the purification process. a, Electrical conductivity, σ. Inset, σ in the low temperature range is magnified. **b**, Seebeck coefficient, *S*. **c**, Power factor, *PF*. Data were measured along the SPS direction. The untreated sample was synthesized using as-received starting Sn reagent. The purified sample was synthesized using starting Sn reagent treated by our purification process.

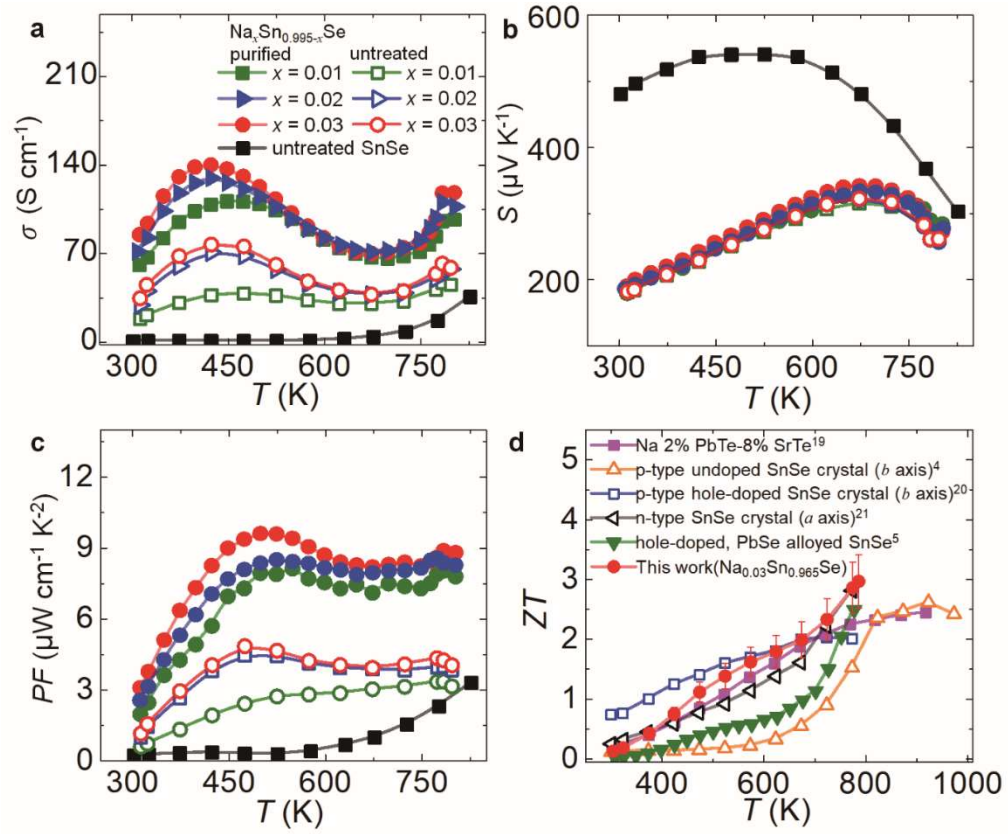

Figure 5.10. Thermoelectric properties of $Na_xSn_{0.995-x}Se$ before and after the purification process. a, Electrical conductivity. **b**, Seebeck coefficient. **c**, Power factor. **d**, ZT values of polycrystalline $Na_xSn_{0.995-x}Se$ developed in this work and current-state-of-art polycrystalline thermoelectrics, 2%Na doped PbTe-8%SrTe[19] and ball-milled and H_2-reduced SnSe-5%PbSe doped with 1% Na[5] and single-crystal SnSe, undoped (p-type)[4], single-crystal Na-doped (p-type)[20], and single-crystal Br-doped SnSe[21]. Polycrystalline samples were measured parallel to the SPS direction. The typical uncertainty of 10% for ZT estimates is given.

The purification process concurrently enhances σ and *S* and decreases κ_{tot} for the $Na_xSn_{0.995-x}Se$ samples, leading to the extraordinarily high thermoelectric figure of merit ZT values. They increase with the higher concentration of Na doping. The $x = 0.03$ sample exhibits the maximum ZT (ZT_{max}) 3.00 at 783 K, which is the highest ever reported for any thermoelectric systems in any forms. In comparison, p- and n-type SnSe single crystals exhibits ZT_{max} ~2.6 at 923 K [13] and ~2.8 at 773 K [19], respectively (Figure 5.10d). The highest performance polycrystalline thermoelectric systems have been non-equilibrium processed PbTe-8%SrTe with ZT_{max} ~2.5 at 923 K [3] and ball milled and H_2-reduced SnSe doped with 1% Na and alloyed with PbSe with ZT_{max} ~2.5 at 773 K [20]. Note that its ZT exceeds unity at 473 K, at which few thermoelectric materials show similar performance. Its average ZT (ZT_{avg}) from 300 to 783 K is ~1.45, outperforming all reported values in the same temperature range. This record high ZT_{avg} is achievable because of the enhanced electrical conductivity in the low to mid-range temperature region. The ZT_{avg} directly determines the maximum thermoelectric conversion efficiency (η) between a hot (T_h) and cold side temperatures (T_c) as shown in eq 1:

$$\eta_{max} = \frac{\Delta T}{T_h} \frac{\sqrt{1 + Z \cdot T_{avg}} - 1}{\sqrt{1 + Z \cdot T_{avg}} + \frac{T_c}{T_h}}$$

The calculated η_{max} for the $x = 0.03$ sample is unprecedentedly high at 15.1% between 300 and 783 K, exceedingly higher than that of the other state-of-the-art thermoelectric systems (Figure 5.13). The estimated η_{max} for the hole-doped SnSe

single crystal is 13.7% between 400 and 773 K. 13.3% for 2.5% K-doped $PbTe_{0.7}Se_{0.3}$ is one of the highest η_{max} reported to date [21].

To understand the origin of the further reduction in κ_{lat} by Na doping, we investigated phonon dispersions and Grüneisen parameters for undoped and 3% Na-doped SnSe using first-principles DFT phonon calculations within the quasi-harmonic approximation [22]. Figure 5.14 shows that Na-doping slightly softens phonon frequency. Especially, the lowest energy transverse acoustic mode (TA_1) is prominently softened along the Γ-Z Brillouin zone direction with the decrease in phonon velocity of TA_1 mode from 1548 to 1305 m/s. Near the zone centers, phonon frequencies of other acoustic modes are not clearly modulated by Na-doping. A distinct frequency lowering arises as crystal momentum increases. However, it should be distinguished from a band crossing by phonon-phonon interaction which occurs near the zone boundaries. In the case of longitudinal acoustic mode (LA), phonon frequency along the Γ-X Brillouin zone direction (out-of-plane direction) increases by Na-doping. It can be attributed to an increased interlayer interaction by Na-doping. Optical modes are also prominently softened.

Grüneisen parameters measure the strength of the bonding anharmonicity. The Grüneisen parameters of acoustic modes are mostly increased by Na-doping (Figure 5.14). It is evident that phonon softening leads to an increase of the Grüneisen parameters except for the unexpected band crossing. The band crossing near the zone boundaries induces an abrupt change of the Grüneisen parameters,

which does not represent a change of anharmonicity of bonding. Interestingly, the Grüneisen parameters of LA mode decreases along the out-of-plane direction, implying Na-doping reduces the anharmonicity and increases the interlayer interaction of SnSe. The average Grüneisen parameters for all the acoustic phonon modes reduce from 2.51, 2.07, and 2.06 to 2.70, 2.48, and 2.44 for TA_1, TA_2, and LA modes, respectively. This result strongly supports the experimental observations given that κ_{lat} is proportional to 1/(Grüneisen parameter)^2. Consequently, the benefit from enriched anharmonicity by Na doping is larger than the accompanying increase in the κ_{ele}, leading to the lowered κ_{tot} in Na-doped SnSe.

To understand the enhancement of Seebeck coefficient for Na-doped SnSe, we examined electronic band structures for undoped and 3% Na-doped SnSe low temperature *Pnma* phase based on DFT calculations (Figure 5.15). Na-doping multiply modulates the valence band of SnSe. First, the doubly degenerated flat band along the X-Γ direction splits, and the upper energy band shifts up near the valence band maximum (VBM). Second, the pudding-mold-type bands at the valence top level along the Γ-Z direction become more consolidated by Na-doping. Na doping raises the energy of the second band along the Γ-Z direction so that the band maximum of the first and the second bands becomes almost same. Third, the doubly degenerated band along the X-direction splits, and the upper energy band moves toward higher energy level. As a result, carrier-contributing hole-pockets (remarked by 1st, 2nd, and 3rd at Figure 5.15) converge at the valence top level. The converged

hole-pockets result in the peak of density of states (DOS) near the VBM (Fig. 5.15), thereby significantly improving the Seebeck coefficient of Na-doped SnSe. The simultaneous emergence of the band convergence and hole-doping by Na-dopant enhances electrical conductivity and Seebeck coefficient for Na-doped SnSe at the same time, despite the general trend of inverse proportionality between them.

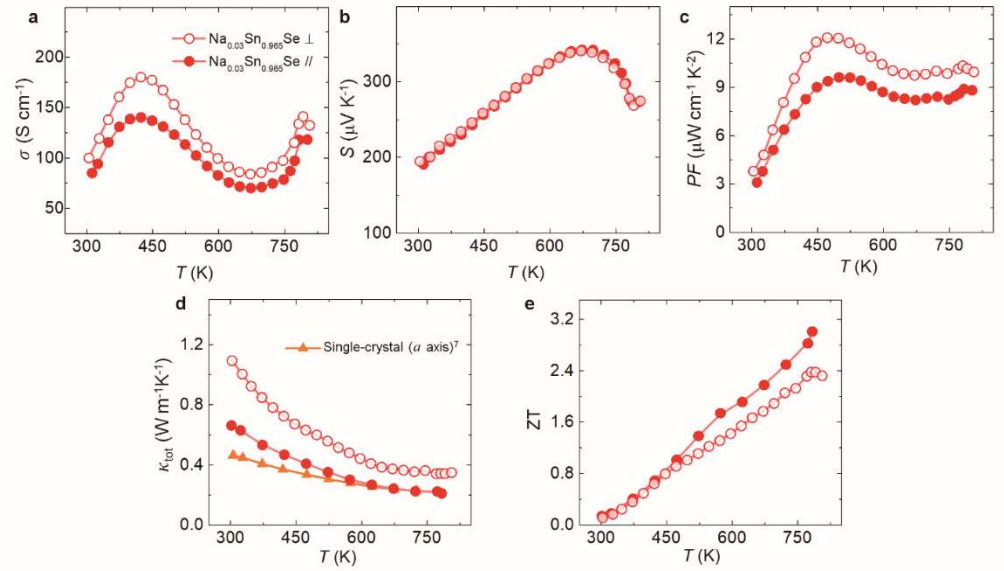

Figure 5.11. Comparison of thermoelectric properties as a function of temperature for the purified $Na_{0.03}Sn_{0.965}Se$ sample parallel, //, and perpendicular, ⊥, to the SPS direction. a, Electrical conductivity, σ. **b,** Seebeck coefficient, *S*. **c,** Power factor, *PF*. **d,** Total thermal conductivity, κ_{tot}. **e,** ZT values. κ_{tot} for single-crystal SnSe along the *a* axis from the previous report[13] is given for comparison.

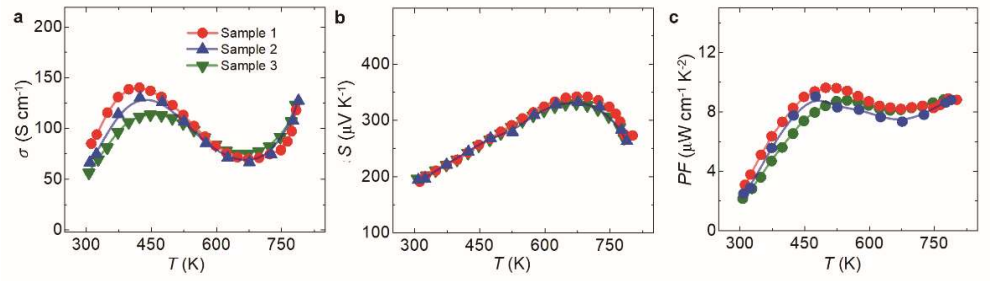

Figure 5.12. The reproducibility of thermoelectric properties as a function of temperature for the purified $Na_{0.03}Sn_{0.965}Se$. a, Electrical conductivity, σ. **b,** Seebeck coefficient, *S*. **c,** Power factor, *PF*. Data were measured along the SPS direction. The samples were independently prepared and measured.

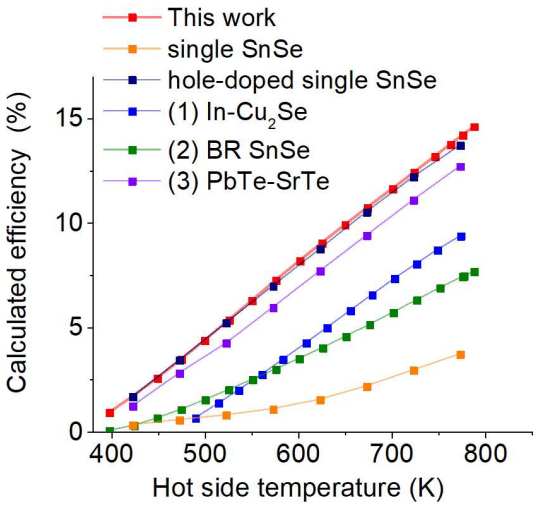

Figure 5.13. The calculated efficiency of purified polycrystalline $Na_{0.03}Sn_{0.965}Se$ sample between ~400 and 780 K. The corresponding value for state-of the-art thermoelectric systems Unless noted as single crystal, all samples are polycrystalline. Because T_c is closer to 400 K rather than 300 K in practical thermoelectric devices for power generation, efficiency was calculated and compared in the temperature range between ~400 and ~780 K. We conservatively calculated efficiency from various independent samples. Note that because there is a slight deviation in start and end temperatures for each system nearby values are used for the calculation.

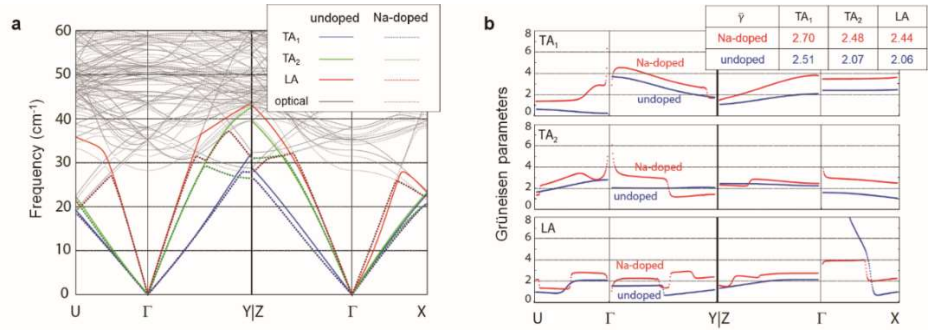

Figure 5.14. Theoretical calculations for phonon dispersions and Grüneisen parameters. phonon scattering branches; LA, longitudinal acoustic phonon sc attering branch. **b,** Grüneisen parameters: inset, the average Grüneisen param eters along the TA_1, TA_2, and LA. We investigated phonon dispersions and Grüneisen parameters for undoped and 3% Na-doped SnSe using first-princip les DFT phonon calculations within the quasi-harmonic approximation[25]. Na-d oping slightly softens phonon frequency in **a**. Especially, the lowest energy t ransverse acoustic mode (TA_1) is prominently softened along the Γ-Z Brillou in zone direction with the decrease in phonon velocity of TA_1 mode from 1 548 to 1305 ms^{-1}. Grüneisen parameters measure the strength of the bonding anharmonicity. The average Grüneisen parameters (γ) for all the acoustic pho non modes increase by Na doping from 2.51, 2.07, and 2.06 to 2.70, 2.48, and 2.44 for TA_1, TA_2, and LA modes, respectively in **b**. Given κ_{lat} proporti onal to γ^{-2}, the benefit from enriched anharmonicity by Na doping is greater than the accompanying increase in κ_{ele}, thereby lowering κ_{tot} for Na-doped SnS e.

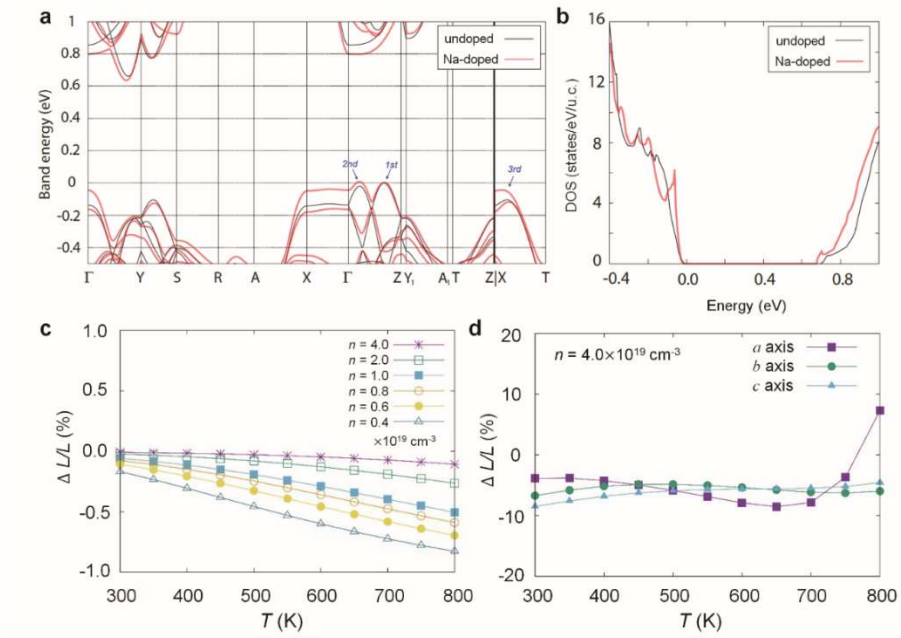

Figure 5.15. Theoretical calculations for electronic band structures and Lorenz numbers of undoped and 3% Na-doped SnSe (*Pnma*). a, Electronic band structures. Carrier-contributing hole-pockets are indicated by 1st, 2nd, and 3rd. **b,** Density of states (DOS) low temperature *Pnma* phase based on DFT calculations. The electronic structures based on DFT calculations for undoped and 3% Na-doped SnSe of the low temperature *Pnma* phase show that Na-doping multiply modulates valence bands of SnSe as shown in **a**. First, the energy of a second valence band maximum (VBM_2) along the Γ-Z direction increases, making an energy gap between a first VBM (VBM_1) and VBM_2 negligible. Second, two doubly degenerated flat bands along the X-Γ and the X-direction split, and their upper energy band shifts to VBM_1. Consequently, carrier-contributing hole-pockets converge at the valence top

level, resulting in the peak of density of states near the VBM as shown in **b**. This significantly improves S of Na-doped SnSe. **c,** The difference ($\Delta L/L$) between the calculated Lorenz number (L) for undoped and 3% Na-doped SnSe by a multiband Kane band model given VBM_1 and VBM_2. **d,** The $\Delta L/L$ between the calculated L for undoped and 3% Na-doped SnSe by a full band model by the BTE calculation with the full DFT electronic structure. See Methods for the details in the calculations.

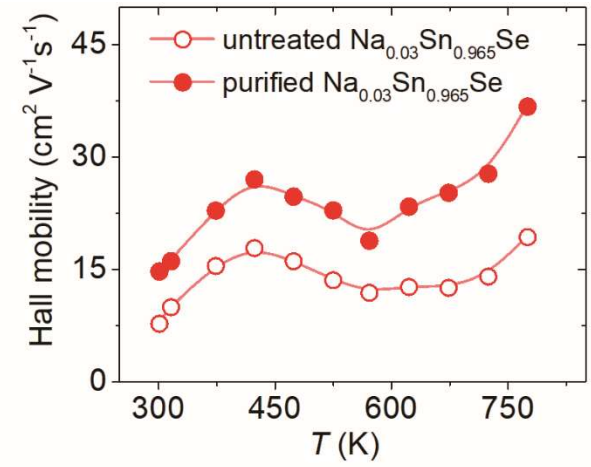

Figure 5.16. Hall mobility for the untreated and purified $Na_{0.03}Sn_{0.965}Se$ samples as a function of temperature.

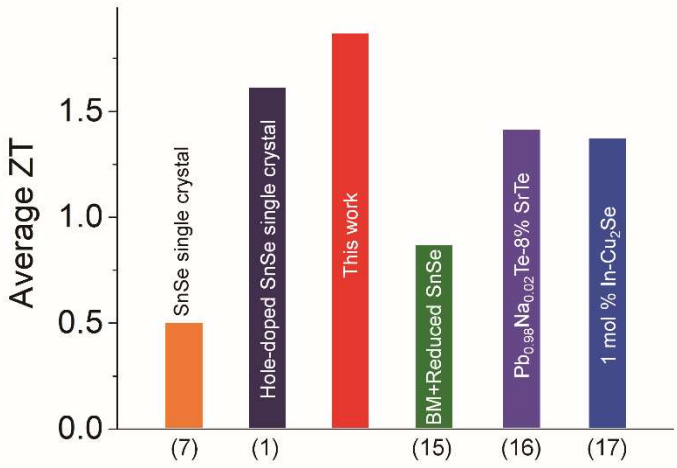

Figure 5.17. The average ZT of purified polycrystalline $Na_{0.03}Sn_{0.965}Se$ sample between ~400 and 780 K. The corresponding value for state-of the-art thermoelectric systems Unless noted as single crystal, all samples are polycrystalline. Because T_c is closer to 400 K rather than 300 K in practical thermoelectric devices for power generation, average ZT was calculated and compared in the temperature range between ~400 and ~780 K. We conservatively calculated average ZT from various independent samples. Note that because there is a slight deviation in start and end temperatures for each system. nearby values are used for the calculation. The average ZT of the purified polycrystalline $Na_{0.03}Sn_{0.965}Se$ sample is calculated between 400 and 783 K.

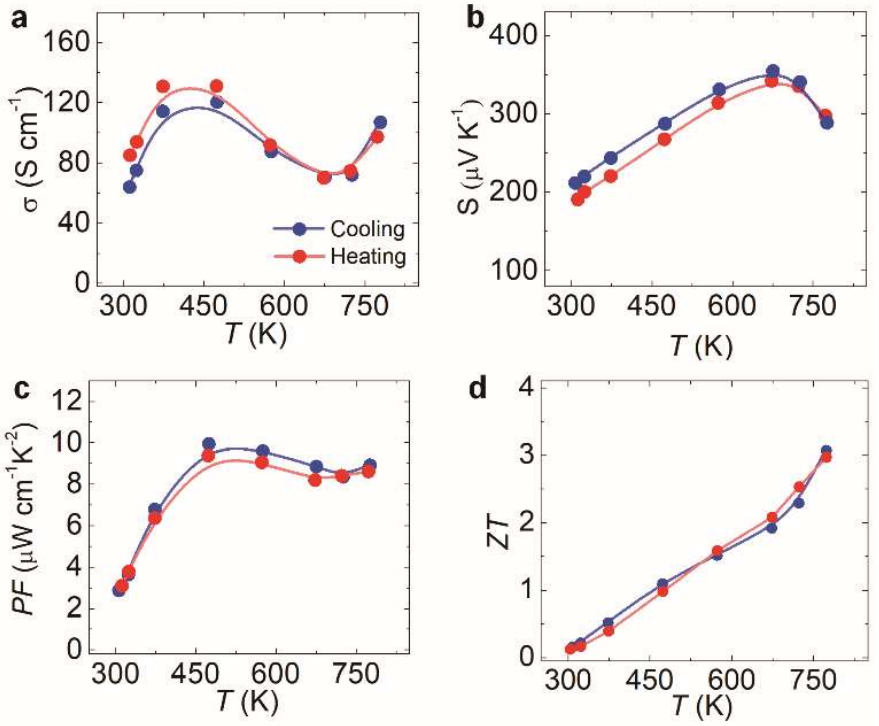

Figure 5.18. Temperature-dependent thermoelectric properties of purified $Na_{0.03}Sn_{0.965}Se$ during heating and cooling. a, Electrical conductivity, σ. **b,** Seebeck coefficient, *S*. **c,** Power factor, *PF*. **d,** ZT value.

Figure 5.19. Typical dense pellets obtained by SPS with a diameter of 13 mm and a height of ~16 mm (center) and the specimens cut for measuring electrical (left, a bar with a length of ~15 mm) and thermal transport properties (right, a disk with a diameter of 8 mm) along the pressing direction of SPS.

Figure 5.20. Test results for thermal diffusivity from Northwestern University. 3 specimens have been prepared independently and measured simultaneously.

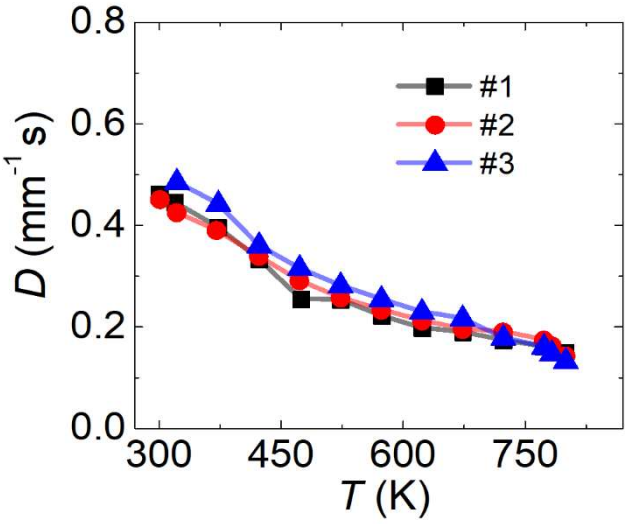

T (K)	#1 (mm^2 s^{-1})	#2 (mm^2 s^{-1})	#3 (mm^2 s^{-1})
300	0.462	0.451	-
323	0.445	0.425	0.485
373	0.396	0.390	0.442
423	0.333	0.339	0.360
473	0.254	0.291	0.315
523	0.253	0.257	0.281
573	0.221	0.233	0.254
623	0.197	0.212	0.229
673	0.189	0.195	0.216
723	0.173	0.190	0.178
773	0.160	0.174	0.160
783	0.156	0.163	0.146
800	0.148	0.143	0.131

Table 5.1. The sample densities for purified SnSe and $Na_xSn_{0.995-x}Se$ samples (x = 0.01, 0.02, 0.03). Their relative densities are around 96%. The theoretical density of single-crystal SnSe is 6.18 g cm^{-3}.

Sample	Density (g cm^{-3})	Relative density (%)
SnSe	5.921	95.8
$Na_{0.01}Sn_{0.985}Se$	5.942	96.1
$Na_{0.02}Sn_{0.975}Se$	5.921	95.8
$Na_{0.03}Sn_{0.965}Se$	5.914	95.6

5.4 Conclusion

The intrinsic thermoelectric properties of SnSe is ultimately uncovered by the purification of as-received elemental Sn reagent and the chemical reduction for synthesized SnSe materials. Hole-doped polycrystalline SnSe outperforms any thermoelectric systems in any forms ever reported in terms of peak ZT, average ZT, and calculated power conversion efficiency. It is remarkable that this extraordinary thermoelectric performance is achievable by removing tin oxide impurity via our facile purification process without complex performance-enhancing strategies and fabrication processes. This observation verifies the thermoelectric properties reported for well-prepared and properly handled SnSe single crystals. The ultrahigh ZT originates from intrinsic crystal chemistry of simple binary compound SnSe, validating the importance of discovery for new materials.

5.5 Reference

1. Gingerich, D. B.; Mauter, M. S., Quantity, Quality, and Availability of Waste Heat from United States Thermal Power Generation. *Environmental Science & Technology* **2015,** *49* (14), 8297-8306.

2. Tan, G.; Zhao, L.-D.; Kanatzidis, M. G., Rationally Designing High-Performance Bulk Thermoelectric Materials. *Chemical Reviews* **2016,** *116* (19), 12123-12149.

3. Tan, G.; Shi, F.; Hao, S.; Zhao, L.-D.; Chi, H.; Zhang, X.; Uher, C.; Wolverton, C.; Dravid, V. P.; Kanatzidis, M. G., Non-equilibrium processing leads to record high thermoelectric figure of merit in PbTe–SrTe. *Nature Communications* **2016,** *7*, 12167.

4. Wei, P.-C.; Bhattacharya, S.; He, J.; Neeleshwar, S.; Podila, R.; Chen, Y. Y.; Rao, A. M., The intrinsic thermal conductivity of SnSe. *Nature* **2016,** *539* (7627), E1-E2.

5. Zhao, L.-D.; Tan, G.; Hao, S.; He, J.; Pei, Y.; Chi, H.; Wang, H.; Gong, S.; Xu, H.; Dravid, V. P.; Uher, C.; Snyder, G. J.; Wolverton, C.; Kanatzidis, M. G., Ultrahigh power factor and thermoelectric performance in hole-doped single-crystal SnSe. *Science* **2016,** *351* (6269), 141-144.

6. Zhao, L.-D.; Chang, C.; Tan, G.; Kanatzidis, M. G., SnSe: a remarkable new thermoelectric material. *Energy & Environmental Science* **2016,** *9* (10), 3044-3060.

7. Turkes, P.; Pluntke, C.; Helbig, R., Thermal conductivity of SnO_2 single crystals. *Journal of Physics C: Solid State Physics* **1980,** *13* (26), 4941-4951.

8. Blöchl, P. E., Projector augmented-wave method. *Physical Review B* **1994,** *50* (24), 17953-17979.

9. Peng, H.; Yang, Z.-H.; Perdew, J. P.; Sun, J., Versatile van der Waals Density Functional Based on a Meta-Generalized Gradient Approximation. *Physical Review X* **2016,** *6* (4), 041005.

10. Kresse, G.; Hafner, J., Norm-conserving and ultrasoft pseudopotentials for first-row and transition elements. *Journal of Physics: Condensed Matter* **1994,** *6* (40), 8245-8257.

11. Kresse, G.; Furthmüller, J., Efficient iterative schemes for ab initio total-energy calculations using a plane-wave basis set. *Physical Review B* **1996,** *54* (16), 11169-11186.

12. Lany, S.; Zunger, A., Assessment of correction methods for the band-gap problem and for finite-size effects in supercell defect calculations: Case studies for ZnO and GaAs. *Physical Review B* **2008,** *78* (23), 235104.

13. Zhao, L.-D.; Lo, S.-H.; Zhang, Y.; Sun, H.; Tan, G.; Uher, C.; Wolverton, C.; Dravid, V. P.; Kanatzidis, M. G., Ultralow thermal conductivity and high thermoelectric figure of merit in SnSe crystals. *Nature* **2014,** *508*, 373.

14. Perdew, J. P.; Ruzsinszky, A.; Csonka, G. I.; Vydrov, O. A.; Scuseria, G. E.; Constantin, L. A.; Zhou, X.; Burke, K., Restoring the Density-

Gradient Expansion for Exchange in Solids and Surfaces. *Physical Review Letters* **2008,** *100* (13), 136406.

15. Pletikosić, I.; von Rohr, F.; Pervan, P.; Das, P. K.; Vobornik, I.; Cava, R. J.; Valla, T., Band Structure of the IV-VI Black Phosphorus Analog and Thermoelectric SnSe. *Physical Review Letters* **2018,** *120* (15), 156403.

16. Madsen, G. K. H.; Carrete, J.; Verstraete, M. J., BoltzTraP2, a program for interpolating band structures and calculating semi-classical transport coefficients. *Computer Physics Communications* **2018,** *231*, 140-145.

17. Lin, H.; Tan, G.; Shen, J.-N.; Hao, S.; Wu, L.-M.; Calta, N.; Malliakas, C.; Wang, S.; Uher, C.; Wolverton, C.; Kanatzidis, M. G., Concerted Rattling in $CsAg_5Te_3$ Leading to Ultralow Thermal Conductivity and High Thermoelectric Performance. *Angewandte Chemie International Edition* **2016,** *55* (38), 11431-11436.

18. Chiritescu, C.; Cahill, D. G.; Nguyen, N.; Johnson, D.; Bodapati, A.; Keblinski, P.; Zschack, P., Ultralow Thermal Conductivity in Disordered, Layered WSe_2 Crystals. *Science* **2007,** *315* (5810), 351-353.

19. Chang, C.; Wu, M.; He, D.; Pei, Y.; Wu, C.-F.; Wu, X.; Yu, H.; Zhu, F.; Wang, K.; Chen, Y.; Huang, L.; Li, J.-F.; He, J.; Zhao, L.-D., 3D charge and 2D phonon transports leading to high out-of-plane ZT in n-type SnSe crystals. *Science* **2018,** *360* (6390), 778-783.

20. Lee, Y. K.; Luo, Z.; Cho, S. P.; Kanatzidis, M. G.; Chung, I., Surface

Oxide Removal for Polycrystalline SnSe Reveals Near-Single-Crystal Thermoelectric Performance. *Joule* **2019,** *3* (3), 719-731.

21. Wu, H. J.; Zhao, L. D.; Zheng, F. S.; Wu, D.; Pei, Y. L.; Tong, X.; Kanatzidis, M. G.; He, J. Q., Broad temperature plateau for thermoelectric figure of merit ZT>2 in phase-separated $PbTe_{0.7}S_{0.3}$. *Nature Communications* **2014,** *5* (1), 4515.

22. Togo, A.; Tanaka, I., First principles phonon calculations in materials science. *Scripta Materialia* **2015,** *108*, 1-5.

Bibliography

International publications

1. “Enhancing p-type thermoelectric performances of polycrystalline SnSe via tuning phase transition temperature”,
   Y. K. Lee, K. Ahn, J. Cha, C. Zhou, H. S. Kim, G. Choi, S. I. Chae, J. Park, S. Cho, S. H. Park, Y. Sung, W. B. Lee, T. Hyeon and I. Chung,
   J. Am. Chem. Soc., **2017**, *139*, 10887.

2. “Surface oxide removal for polycrystalline SnSe reveals near-single-crystal thermoelectric performance”,
   Y. K. Lee, Z. Luo, S. P. Cho, M. G. Kanatzidis, I. Chung, *Joule,* **2019**, *3*. 719.

3. “High Performance n-type PbSe-Cu_2Se Thermoelectrics through Conduction Band Engineering and Phonon Softening”,
   C. Zhou, Y. Yu, **Y. K. Lee**, O. Cojocaru-Miredin, B. Yoo, S. P. Cho, J. Im, M. Wuttig, T. hyeon, I. Chung, *J. Am. Chem. Soc.,* **2018**, *140*, 15535.

4. “Defect Engineering for High-Performance n-Type PbSe Thermoelectrics”,
   C. Zhou, **Y. K. Lee**, J. Cha, B. Yoo, S. P. Cho, T. Hyeon, I. Chung, *J. Am. Chem. Soc*., **2018**, *140*, 9282.

5. “High Thermoelectric Performance in n-Type Polycrystalline SnSe via Dual Incorporation of Cl and PbSe and Dense Nanostructures”,
   J. I. Cha, C. Zhou, **Y. K. Lee**, S. P. Cho, I. Chung, *ACS Appl. Mater. Interfaces,* **2019**, *11*, 21645.

6. “Unusual n-type thermoelectric properties of Bi_2Te_3 doped with divalent alkali earth metals”,
   S. Byun, J. Cha, C. Zhou, **Y. K. Lee**, H. Lee, S. H. Park, W. B. Lee, I. Chung, *J. Solid State Chem.*, **2019**, *269*, 396.

7. “Cu Intercalation and Br Doping to Thermoelectric $SnSe_2$ Lead to Ultrahigh Electron Mobility and Temperature-Independent Power Factor”, C. Zhou, Y. Yu, X. Zhang, J. Xu, **Y. K. Lee**, B. Yoo, G. Liu, S. P. Cho, M. Wuttig, T. Hyeon, I. Chung,
   Adv. Funct. Mater., **2020**, *30*, 1908405.

8. “Indene-C60 Bisadduct Electron-Transporting Material with the High LUMO Level Enhances Open-Circuit Voltage and Efficiency of Tin-Based Perovskite Solar Cells”, M. Lee, D. Kim, **Y. K. Lee**, H. Koo, K. T. Lee, I. Chung, *ACS Appl. Energy Mater.,* **2020,** *https://doi.org/10.1021/acsaem.0c00535*

국 문 초 록

인구의 급격한 증가와 화석연료가 점점 고갈됨에 따라 전 세계적으로 새로운 에너지원에 대한 수요가 급증하고 있다. 이렇게 생산되는 에너지 중 60% 이상이 폐열의 형태로 낭비되고 있다. 열전 기술은 열에너지를 전기에너지로 변환시킬 수 있는 기술로, 버려지는 폐열을 전기에너지로 사용할 수 있기 때문에 차세대 친환경 에너지원으로 많은 각광을 받고 있다. 해당 기술의 상용화, 실용화를 위해서 현재 가장 문제가 되는 것은 열전 소재의 낮은 성능이다. 기존에 가장 많이 연구된 비스무스 텔루라이드, 리드 텔루라이드와 같은 열전 소재는 다양한 전략을 통해 높은 열전성능을 보이고 있으나 독성이 있는 리드 또는 매우 값비싼 텔루륨과 같은 원소를 지니고 있어 한계를 지니고 있다. 본 학위논문은 다양한 열전 소재 중, 친환경인 소재인 틴 셀레나이드의 열전 성능 향상 연구에 대해 논의 하고자 한다.

첫번째로 다결정 틴 셀레나이드에 리드셀레나이드 및 소듐을 도입하였다. 리드셀레나이드의 합금화를 통해 780 K 부근에서 일어나는 *Pnma*의 결정구조에서 *Cmcm*의 결정구조로의 상전이 온도가 감소하는 것을 확인하였다. 또한 소듐을 도입하여 최적의 캐리어 농도를 10의 19승 수준으로 향상시킬 수 있었다. 최적화된 캐리어 농도와 낮아진 상 전이 온도에

의해 향상된 전기전도도 및 파워팩터를 확인하였다. 또한 리드 셀레나이드의 도입은 고용체를 형성한다고 여겨지던 기존의 상태도의 정보와 다르게 나노구조를 틴 셀레나이드 소재 내에 형성함을 수차보정 투과전자현미경을 통해 관찰하였다. 이를 통해 리드 셀레나이드의 도입은 점산란 및 나노구조에 의한 산란을 유발하며 이에 의해 열전도도가 낮아짐을 규명하였다. 파워팩터의 향상 및 감소된 열전도도에 의해 $Na_{0.01}(Sn_{0.95}Pb_{0.05})_{0.99}Se$의 조성에서 약 1.2의 열전성능지수 ZT를 보이는 p형 틴셀레나이드계 소재를 성공적으로 개발하였다.

두번째로, 결함을 이용하여 틴 셀레나이드의 열전성능을 향상시키는 연구를 진행하였다. 틴 셀레나이드에 공극 및 인듐을 도입하였으며, 함량의 조절을 통해 각 인자가 도입됨에 따라 전기전도도 및 열전도도가 동시에 감소함을 확인하였다. 하지만 인듐의 도입을 통해 전자 밴드구조가 변화되어 제백계수가 향상되었고 이를 통해 파워팩터의 감소를 최소화 하였다. 낮아진 열 전도도 및 향상된 파워팩터를 통해 $Na_{0.01}(Sn_{0.97}In_{0.01})_{0.99}Se$의 조성에서 약 2.0의 열전 성능지수를 확인하였다. 동일한 조성임에도 불구하고 어닐링 공정을 진행한 경우 열전도도가 보다 낮아지는 현상을 발견하여 수차보정 투과전자현미경을 통해 어닐링 시간에 따른 미세구조의 변화를 확인하였다. 어닐링을 진행하지 않은 소재에서 공극들이 클러스터를 이루며 분포되어 있으며, 어닐링이 진

행됨에 따라 공극 클러스터들이 모여 일정한 방향으로 헤테로스트럭쳐를 형성함을 확인하였다. 시간별 투과전자현미경 이미지 및 상 분석을 통해 인듐 셀레나이드의 이종상이 벌크 틴 셀레나이드 내에 형성되었음을 확인하였으며 이를 통해 낮아진 열전도도의 원인을 규명하였다. 더불어 틴 셀레나이드 내에 공극의 형성 및 헤테로스트럭쳐의 규명 매커니즘을 제시하여 다른 원소의 도입을 통한 틴 셀레나이드 벌크 소재 내의 나노구조체의 형성 가능성을 제시하였다.

마지막으로, 지금까지 규명되지 않았던 단결정 틴 셀레나이드와 다결정 틴 셀레나이드의 열전 성능 차이에 대한 원인을 밝히고자 하였다. 틴 셀레나이드보다 약 140배의 열전도도를 가지는 틴 산화물의 형성을 다결정의 틴 셀레나이드의 높은 열전도도의 원인임을 수차보정 투과전자현미경을 통해 확인하였다. 이를 해결하고자 볼밀 및 환원공정을 진행하였으며 공정 후의 소재에서 산화물의 함량이 줄어듦과 동시에 단결정 수준의 낮은 열전도도를 확인하였다. 이를 통해 열전성능지수 ZT 2.5를 가지는 소재를 개발하였다.

또한 합성 시 사용되는 틴 내부의 틴 산화물을 제거하기 위해 정제 및 환원공정을 진행하여 낮은 산화물의 함량을 가지는 틴 셀레나이드를 개발하였으며 단결정 틴 셀레나이드보다 낮은 격자 열전도도를 확인하였

다. 또한 소듐의 도핑을 통해 전기전도도 및 파워팩터를 향상시켜 파워팩터를 단결정 수준으로 향상시켰다. 결과적으로, 단결정에 비해 높은 틴셀레나이드의 열전도도의 원인을 실험적, 이론계산적으로 밝혀내었으며, 지금까지 보고된 열전 소재 중 가장 높은 열전성능인 ZT 3.0 가지는 소재를 개발하였다.

다결정 틴 셀레나이드의 다양한 원소 및 공극의 도입을 통해 열전 성능의 변화 및 소재의 미세구조 변화 등을 확인하여 소재 전반에 대한 이해도를 높였으며, 원소의 정제, 볼밀 및 환원 공정을 통해 단결정과 다결정 틴셀레나이드의 성능차이의 원인을 규명하였다. 이와 같은 전략은 모든 열전 소재에 적용될 수 있으므로 비단 틴 셀레나이드 뿐 아니라 전반적인 열전 소재 분야의 성능 향상에 기여할 수 있다.

주요어: 열전 소재, 다결정, 틴 셀레나이드, 리드 셀레나이드, 결함, 정제 공정, 환원 공정

학번: 2016-30236